

UC San Diego

UC San Diego Electronic Theses and Dissertations

Title

Thermodynamic Strategies of Electrocatalyst Design for CO2 Reduction

Permalink

<https://escholarship.org/uc/item/8d88f2t9>

Author

Ostericher, Andrew Logan

Publication Date

2019

Peer reviewed|Thesis/dissertation

UNIVERSITY OF CALIFORNIA SAN DIEGO

Thermodynamic Strategies of Electrocatalyst Design for CO₂ Reduction

A dissertation submitted in partial satisfaction of the
requirements for the degree
Doctor of Philosophy

in

Chemistry

by

Andrew L. Ostericher

Committee in charge:

Professor Clifford P. Kubiak, Chair
Professor Andrew C. Kummel
Professor Stephen P. Mayfield
Professor Alina M. Schimpf
Professor William C. Trogler

2019

Copyright
Andrew L. Ostericher, 2019
All rights reserved.

The dissertation of Andrew L. Ostericher is approved, and it is acceptable in quality and form for publication on microfilm and electronically:

Chair

University of California San Diego

2019

DEDICATION

For my mother.

EPIGRAPH

*Well the water, it runs deep,
where it don't run wide.*

TABLE OF CONTENTS

Signature Page	iii
Dedication	iv
Epigraph	v
Table of Contents	vi
List of Figures	viii
List of Tables	xii
Acknowledgements	xiii
Vita	xvii
Abstract of the Dissertation	xviii
Chapter 1	CO ₂ Capture & Utilization: The Necessity and Challenges of Implementing Carbon-Neutral Economies	1
	1.1 The Necessity for Non-Petrochemical Fuel Sources	1
	1.2 Potential Routes of CO ₂ Conversion to Liquid Fuels	5
	1.3 Fundamental Challenges in Catalyst Design	7
	1.4 References	10
Chapter 2	Hydricity of Transition Metal Hydrides: Thermodynamic Considerations for CO ₂ Reduction	13
	2.1 Introduction	13
	2.2 Results & Discussion	16
	2.2.1 Dataset of Metal Hydride Complexes	16
	2.2.2 Correlation of Hydricity and Reduction Potential	18
	2.2.3 Expansion to Other Hydride Classes	25
	2.2.4 Implications for CO ₂ Reduction	28
	2.2.5 Limitations of the Model.	36
	2.3 Conclusion	38
	2.4 References	41
	2.5 Appendix A	51
Chapter 3	Utilization of Thermodynamic Scaling Relationships in Hydricity to Develop Nickel Hydrogen Evolution Reaction Electrocatalysts with Weak Acids and Low Overpotentials	56
	3.1 Introduction	56

3.2	Results & Discussion	58
3.2.1	Synthesis and Characterization	58
3.2.2	Electrochemistry	61
3.2.3	Estimation of Hydricity	63
3.2.4	Electrocatalytic Hydrogen Evolution	66
3.3	Conclusion	70
3.4	Experimental	71
3.5	References	75
3.6	Appendix B	78
Chapter 4	Thermodynamic Targeting of Electrocatalytic CO ₂ Reduction: Advantages, Limitations, and Insights for Catalyst Design	99
4.1	Introduction	99
4.2	Results and Discussion	101
4.2.1	Overview of the System Studied	101
4.2.2	Electrocatalytic CO ₂ Reduction	102
4.2.3	Infrared Spectroelectrochemistry	105
4.2.4	Computational Studies	106
4.2.5	Proposed Mechanism	108
4.2.6	Insights for Future Catalyst Design	110
4.3	Conclusion	112
4.4	Experimental	112
4.5	References	115
4.6	Appendix C	118

LIST OF FIGURES

Figure 1.1:	Improvements in global life expectancy since 1770. Adapted from references 1-2.	2
Figure 1.2:	Atmospheric CO ₂ concentrations for the last 10,000 years. Reproduced with permission from reference 8.	3
Figure 1.3:	Estimated renewable share of total energy consumption from 2016. Adapted from reference 11.	4
Figure 1.4:	Energy density of selected storage methods. “Batteries” encompass average values for lithium-ion, alkaline, nickel-metal hydride, and lead-acid batteries. Data sourced from references 15-17.	5
Figure 1.5:	Standard reduction potentials of CO ₂ to various products at standard conditions in aqueous solution vs. NHE.	6
Figure 2.1:	Modes of metal hydride bond dissociation.	14
Figure 2.2:	Hydricity in terms of BDFE and $E_{1/2}(M^{n+}/(n-1)^+)$	15
Figure 2.3:	Structures and abbreviations for the parent complexes [M] ⁿ⁺ of the metal hydrides [M-H] ⁽ⁿ⁻¹⁾⁺	19
Figure 2.4:	Phosphine ligand structures and abbreviations.	20
Figure 2.5:	Correlation of ΔG_{H-}° with the first one-electron reduction potential of the parent metal complex. Fixed slope line given by black dashed trace.	24
Figure 2.6:	Correlation of pK _a with the second reduction potential of the parent metal complex. Fixed slope line given by black dashed trace.	25
Figure 2.7:	Acidity in terms of BDFE and $E_{1/2}(M^{(n-1)}/(n-2)^+)$	26
Figure 2.8:	Correlation of ΔG_{H-}° with the first one-electron reduction potential for organic compounds. Fixed slope line for metal hydrides given by lower black dashed trace.	27
Figure 2.9:	Hydricity requirements for hydride transfer to CO ₂	28
Figure 2.10:	Comparison of ΔG_{H-}° of metal hydrides (filled points), organic hydride donors (open points), and formate (solid black trace).	29
Figure 2.11:	Strength of the base required for H ₂ cleavage for a given hydricity. B = base, BH ⁺ = conjugate acid of B.	30
Figure 2.12:	Representative catalytic cycle for CO ₂ hydrogenation with a metal hydride. Hydricity requirement for favorable CO ₂ reduction given by top equation. pK _a requirement for favorable H ₂ activation given by bottom equation. B = base, BH ⁺ = conjugate acid of B.	31
Figure 2.13:	Modified Pourbaix diagram indicating the thermodynamic stability of a metal hydride and BH ⁺ relative to CO ₂ and H ₂	32
Figure 2.14:	Thermochemical cycle used to estimate $E^\circ(\text{CO}_2/\text{HCO}_2^-)$ in acetonitrile. B = base, BH ⁺ = conjugate acid of B. S = acetonitrile.	33
Figure 2.15:	Thermochemical cycle used to estimate $E^\circ(\text{CO}_2/\text{HCO}_2\text{H})$ in acetonitrile. B = base, BH ⁺ = conjugate acid of B. S = acetonitrile.	34

Figure 2.16:	Comparison of the standard reduction potential for the CO ₂ /formic acid (pink line) and CO ₂ /formate (blue line) couples as a function of pK _a (BH ⁺) (right axis), overlaid with the fixed slope correlation of ΔG _{H-} ^o (M-H) and E _{1/2} (M ^{n+/(n-1)+}).	36
Figure 2.17:	Correlation of ΔG _{H-} ^o with the first one-electron reduction potential of the parent metal complex. Only complexes that exhibit a one-electron E _{1/2} (M ^{n+/(n-1)+}) redox couple are included.	51
Figure 2.18:	Correlation of ΔG _{H-} ^o with the first two-electron reduction potential of the parent metal complex. Only complexes that exhibit a two-electron E _{1/2} (M ^{n+/(n-2)+}) redox couple are included.	51
Figure 2.19:	Correlation of ΔG _{H-} ^o with the first one-electron reduction potential of the parent metal complex, including [Rh(depx) ₂] ⁺ and [Pt(EtXanphos) ₂] ²⁺ . Fixed slope line given by black dashed trace.	53
Figure 2.20:	Agreement between BDFE calculated from pK _a and hydricity values. Only systems for which the parent metal complex exhibit a one-electron E _{1/2} (M ^{n+/(n-1)+}) redox couple are included.	53
Figure 2.21:	BDFE calculated from known hydricity values as function of experimental reduction potential.	54
Figure 3.1:	Hydrogen evolution in terms of metal-hydride hydricity.	57
Figure 3.2:	Synthesis of 1 , 2 , and 3	59
Figure 3.3:	Crystal structures of 1 and 2 . Thermal ellipsoids are drawn at the 50% probability level. Hydrogen atoms and PF ₆ counterions are omitted for clarity.	59
Figure 3.4:	Crystal structure of 3 . Thermal ellipsoids are drawn at the 50% probability level. Hydrogen atoms are omitted for clarity.	60
Figure 3.5:	Cyclic voltammograms of 1 (red) and 2 (blue) in acetonitrile (1 mM nickel in 0.1 M Bu ₄ NPF ₆). Scan rate 100 mV/s.	62
Figure 3.6:	Hydricities of transition metal hydrides as a function of E _{1/2} (M ^{n+/(n-1)+}) in acetonitrile. E _{1/2} (Ni ^{II/0}) and corresponding predicted ΔG _{H-} ^o for 1 and 2 indicated by the red and blue stars, respectively. Adapted from Ref. 10.	64
Figure 3.7:	Hydricity in terms of E _{1/2} (M ^{n+/(n-1)+}).	65
Figure 3.8:	Cyclic voltammetry of 2 in the absence and presence of 0.8 M methanol in acetonitrile (1 mM 2 in 0.1 M Bu ₄ PF ₆). Scan rate 100 mV/s.	66
Figure 3.9:	Cyclic voltammograms of 2 with increasing phenol concentration in acetonitrile (1 mM 2 in 0.1 M Bu ₄ NPF ₆). Scan rate 100 mV/s.	67
Figure 3.10:	Catalytic Tafel plots for 2 , Co(dmgH) ₂ (py) (DMF solution), ⁷ [Ni(P ₂ ^{Ph} N ₂ ^{Ph}) ₂] ²⁺ (CH ₃ CN solution), ⁵ Fe(TPP) (DMF solution), ⁶ [Ni(P ₂ ^{PhCF₃} N ₂ ^{Ph-C₁₄}) ₂] ²⁺ (hexanedinitrile/H ₂ O solution) ⁸ with 1.0 M Brønsted acid.	69
Figure 3.11:	¹ H NMR (500 MHz) spectrum of 1 in CD ₃ CN.	78
Figure 3.12:	³¹ P NMR (500 MHz) spectrum of 1 in CD ₃ CN.	78
Figure 3.13:	¹³ C NMR (500 MHz) spectrum of 1 in CD ₃ CN.	79
Figure 3.14:	¹ H NMR (500 MHz) spectrum of 2 in CD ₃ CN.	79

Figure 3.15:	^{31}P NMR (500 MHz) spectrum of 2 in CD_3CN	80
Figure 3.16:	^{13}C NMR (500 MHz) spectrum of 2 in CD_3CN	80
Figure 3.17:	^1H NMR (500 MHz) spectrum of 3 in C_6D_6	81
Figure 3.18:	^{31}P NMR (500 MHz) spectrum of 3 in C_6D_6	81
Figure 3.19:	^{13}C NMR (500 MHz) spectrum of 3 in C_6D_6	81
Figure 3.20:	Cyclic voltammograms of 1 (1 mM) in acetonitrile. 0.1 M TBAPF ₆ , glassy carbon working electrode, platinum counter, Ag/AgCl reference, internal ferrocene reference.	82
Figure 3.21:	Plot of peak current vs. scan rate for 1	82
Figure 3.22:	Cyclic voltammograms of 2 (1 mM) in acetonitrile. 0.1 M TBAPF ₆ , glassy carbon working electrode, platinum counter, Ag/AgCl reference, internal ferrocene reference.	83
Figure 3.23:	Plot of peak current vs. scan rate for 2	83
Figure 3.24:	Post-catalysis electrode rinse test. Red trace: 1 mM 2 , 1.0 M phenol, 0.1 M TBAPF ₆ in ACN with internal ferrocene reference. 100 mV s ⁻¹ scan rate. Black trace: unpolished glassy carbon electrode post-catalysis in fresh solution with same conditions in absence of catalyst. 100 mV s ⁻¹ scan rate.	84
Figure 3.25:	Cyclic voltammogram of phenol (3.0 M) in acetonitrile. 0.1 M TBAPF ₆ , glassy carbon working electrode, platinum counter, Ag/AgCl reference, internal ferrocene reference.	84
Figure 3.26:	Controlled potential electrolysis at -1.9 V vs. Fc ⁺⁰ in the presence and absence of 2 . Conditions: 0.1 M TBAPF ₆ in acetonitrile with 0.2 M phenol and 1 mM Fc internal standard, glassy carbon working electrode, graphite rod counter electrode, Ag/AgNO ₃ reference electrode.	85
Figure 3.27:	Plot of electrons passed vs H ₂ produced during controlled potential electrolysis of 2 with phenol. Average Faradaic Efficiency of 112 ± 5%.	85
Figure 3.28:	Cyclic voltammograms of 1 in presence and absence of phenol. 1 mM 1 in acetonitrile with 0.1 M TBAPF ₆ , glassy carbon working electrode, platinum counter, Ag/AgCl reference at 100 mV s ⁻¹ scan rate.	86
Figure 3.29:	Cyclic voltammograms of 1 with varying concentrations of HNEt ₃ BF ₄ . 1 mM 1 in acetonitrile with 0.1 M TBAPF ₆ , glassy carbon working electrode, platinum counter, Ag/AgCl reference at 100 mV s ⁻¹ scan rate.	86
Figure 3.30:	Graphical representation of i_{cat} , i_p , E_{cat} , $E_{cat/2}$, and $E_{\text{H}^+/\text{H}_2}^{/circ}$, for rate and overpotential determination following methods by Appel and Helm. ⁷	90
Figure 4.1:	Thermochemical cycle for hydride transfer to CO ₂	100
Figure 4.2:	Hydricity in terms of BDFE and $E_{1/2}(M^{n+/(n-1)+})$	100
Figure 4.3:	Complex 1 and bis-NHC ligand.	102
Figure 4.4:	Plot of known hydricities of d ^{8/9} metals versus $E_{1/2}(M^{n+/(n-1)+})$	103
Figure 4.5:	Cyclic voltammograms of 1 (1 mM) in the presence of phenol (up to 0.4 M) under atmospheres of CO ₂ and N ₂	104

Figure 4.6:	Cyclic voltammograms of 1 (1 mM) with no added proton source under nitrogen (black) and under CO ₂ (blue). Conditions: 0.1 M Bu ₄ NPF ₆ in acetonitrile at 100 mV s ⁻¹ ; glassy carbon working electrode; platinum counter electrode; Ag/AgCl reference electrode.	105
Figure 4.7:	IR-SEC of 1 (3 mM) in CO ₂ -saturated acetonitrile in the absence of an added proton source, sweeping from 0 to -1.8 V vs. Ag pseudoreference electrode.	107
Figure 4.8:	DFT-calculated HOMOs and LUMOs of complexes 1 , 1 ⁰ , and 1 ^H . Hydrogen atoms are omitted for clarity with the exception of the hydride of 1 ^H	109
Figure 4.9:	Proposed mechanistic pathways of CO ₂ reduction and hydrogen evolution by 1	110
Figure 4.10:	Controlled potential electrolysis at -1.75 V vs. Ag/AgCl in the presence of 1 under CO ₂ . Conditions: 0.1 M TBAPF ₆ in acetonitrile with 0.1 M phenol, glassy carbon working electrode, graphite rod counter electrode, Ag/AgCl reference electrode.	118
Figure 4.11:	Plot of charge passed vs. gas products produced during controlled potential electrolysis shown in Figure 4.11. Slopes of 0.27593 and 0.12374 for the 2-electron products of H ₂ and CO correspond to Faradaic Efficiencies of 55% and 25%, respectively.	118
Figure 4.12:	Cyclic voltammograms of 1 (1 mM) under nitrogen with no added proton source (black), with 0.8 M methanol under nitrogen (blue), and 0.8 M methanol under CO ₂ (red).	119
Figure 4.13:	Controlled potential electrolysis at -1.75 V vs. Ag/AgCl in the presence of 1 under CO ₂ . Conditions: 0.1 M TBAPF ₆ in acetonitrile with 0.4 M methanol, glassy carbon working electrode, graphite rod counter electrode, Ag/AgCl reference electrode.	119
Figure 4.14:	Plot of charge passed vs. gas products produced during controlled potential electrolysis shown in Figure 4.13. Slopes of 0.01849 and 0.10916 for the 2-electron products of H ₂ and CO correspond to Faradaic Efficiencies of 4% and 22%, respectively.	120
Figure 4.15:	¹ H NMR of bulk work-up of CPE from Figure 4.13 in D ₂ O, showing formate resonance at 8.21 ppm and maleic acid internal standard at 6.40 ppm. Identical workup of control CPE under the same conditions save for the absence of 1 was void of a formate resonance.	120
Figure 4.16:	Experimental (blue) and DFT-calculated (red) FTIR spectra of the carbonyl stretches of the proposed degradation species [Ni(bis-NHC)(CO) ₂] ⁰ . For details on optimized structure used for calculations and input files, see Computational Methods section below.	121
Figure 4.17:	IR-SEC of 1 (3 mM) in ¹³ CO ₂ -saturated acetonitrile in the absence of an added proton source, sweeping from -1.2 to -1.7 V vs. Ag pseudoreference electrode.	121
Figure 4.18:	IR-SEC of 1 (3 mM) in CO ₂ -saturated acetonitrile in the presence of phenol (0.1 M), sweeping from -1.1 to -1.8 V vs. Ag pseudoreference electrode.	122

LIST OF TABLES

Table 2.1:	Thermodynamic data for nickel complexes.	21
Table 2.2:	Thermodynamic data for palladium and platinum complexes.	22
Table 2.3:	Thermodynamic data for group eight and nine complexes.	23
Table 2.4:	Comparison of standard reduction potentials for CO ₂ to formate/formic acid or CO.	34
Table 2.5:	Organic hydride donor dataset.	52
Table 3.1:	Cyclic voltammetry data and predicted hydricities for 1 and 2	61
Table 3.2:	Crystal data and structure refinement for Complex 1 . (CCDC: 1852576)	92
Table 3.3:	Selected bond distances for complex 1	93
Table 3.4:	Selected bond angles for complex 1	93
Table 3.5:	Crystal data and structure refinement for Complex 2 . (CCDC: 1851821)	94
Table 3.6:	Selected bond distances for complex 2	95
Table 3.7:	Selected bond angles for complex 2	95
Table 3.8:	Crystal data and structure refinement for Complex 3 . (CCDC: 1851844)	96
Table 3.9:	Selected bond distances for complex 3	97
Table 3.10:	Selected bond angles for complex 3	97
Table 4.1:	Selected calculated and experimental bond lengths.	108
Table 4.2:	Optimized geometry coordinates for complex 1	124
Table 4.3:	Optimized geometry coordinates for complex 1 ⁰	127
Table 4.4:	Optimized geometry coordinates for complex 1 ^H	130

ACKNOWLEDGEMENTS

Thanks first and foremost to my friends. Through some incredible cosmic fortune I have ended up surrounded by a group of people that are not only genuine, caring, and supportive, but also stimulating, curious, and adventurous. They are scattered from San Diego and Seattle to Germany, Spain, and Sweden. They are scientists and engineers and mathematicians and artists and musicians and whiskey makers and many other things. Those here in San Diego are Miles, MJ, Lisa, Chase, Adrian and Alison just to name a few. And then there's my longest friend and platonic life partner, Jimmy Mills, whose questionable advice and dubious guidance has led me astray in the best possible ways for two and a half decades.

Also thanks to my parents. To my mother, for being the most loving person I have ever known as well as instilling in me a curiosity for the world. My pursuit of science, language, and music is a direct result of that curiosity. And I have you to thank. I love you. And to my father. I don't know if I would be here today had it not been for the countless hours over the course of *The Dark Year* when we stood side by side, throwing flies on pristine trout streams.

Thanks also to my brother, Ian. From thirty-hour South American bus rides to wading through rivers in the mountains of Slovenia, the *Brothers Ostericher* have had more adventures than most people have in a lifetime. Let's have some more. And if recent trends are at all indicative of what is to come, they are likely only to get crazier...

I am also thankful to so many people within the Department of Chemistry & Biochemistry. My lab mates have been incredible co-workers and friends. So thank you to past co-workers Dr. Tyler Porter, Dr. Kate Waldie, and Dr. Mark Reineke in particular, and present colleagues Felix Brunner, Chris Miller, Daphne Cheung, Joe Palasz, Nicole Torquato and Thomas Chan. Outside of our lab, thanks go to Joe Palomba and Michael Neville. Thanks also to Dr. Doug Agnew and Dr. Chuck Mokhtarzadeh, who were both early mentors and inspirations of mine in the department. I also thank Dr. Milan Gembicky, Dr. Curtis Moore, and Dr. Arnold Rheingold for their guidance and instruction in the crystallography laboratory.

Finally, I wish to thank my advisor, Cliff, for his support and mentorship. I have developed so much as a scientist under your guidance and as a result, there are doors open that were once a far off dream. Thank you.

CHAPTER-SPECIFIC ACKNOWLEDGEMENTS

Chapter 2, in full, is a reprint of the material as it appears in Waldie, K. M.;[‡] Ostericher, A. L.;[‡] Reineke, M.; Sasayama, A. F.; Kubiak, C. P. "Hydricity of Transition-Metal Hydrides: Thermodynamic Considerations for CO₂ Reduction" *ACS Catalysis*, **2018**, 8, 1313-1324. The dissertation author was the primary co-author of this paper. We would like to acknowledge the early contributions to this work and the helpful discussions of Candace Seu, and the experimental contributions of Alyssia Lilio and Michael Doud. We would like to acknowledge productive discussions with members of the molecular catalysis group at Pacific Northwest National Laboratory. We would also like to acknowledge our reviewers for useful advice about presenting this study. This work was supported by the Air Force Office of Scientific Research through the MURI program under AFOSR Award FA9550-10-1-0572.

Chapter 3, in full, is a reprint of the material as it appears in Ostericher, A. L.; Waldie, K. M.; Kubiak, C. P. "Utilization of Thermodynamic Saling Relationships in Hydricity to Develop Nickel Hydrogen Evolution Reaction Electrocatalysts with Weak Acids and Low Overpotentials" *ACS Catalysis*, **2018**, 8, 9596-9603. The dissertation author was the primary author of this paper. We acknowledge Dr. Mark H. Reineke for early contributions relating to this work, Tyler Porter for invaluable discussions, and the UCSD Molecular Mass Spectrometry Facility for sample analysis. This work was supported by the Air Force Office of Scientific Research through the MURI program under AFOSR Award FA9550-10-1-0572 and is based in part upon work performed by the Joint Center for Artificial Photosynthesis, a DOE Energy Innovation Hub, supported through the Office of Science of the U.S. Department of Energy under Award No. DE-SC0004993.

Chapter 4, in full, is being prepared for submission for publication of the material entitled, Ostericher, A. L.; Porter, T. M.; Kubiak, C. P., "Thermodynamic Targeting of Electrocatalytic CO₂ Reduction: Advantages, Limitations, and Insights for Catalyst Desing." The dissertation author was the primary author of this material. This work was supported by the Joint Center for

Artificial Photosynthesis, a DOE Energy Innovation Hub, supported through the Office of Science of the U.S. Department of Energy under Award No. DE-SC0004993.

VITA

2011	B. S. in Chemistry, University of Washington, Seattle, WA, USA
2013	M. S. in Chemistry, Freie Universität Berlin, Germany
2014-2015	Distiller, Westland Distillery, Seattle, WA, USA
2019	Ph. D. in Chemistry, University of California San Diego, CA, USA

PUBLICATIONS

Ostericher, A. L.; Waldie, K. M.; Kubiak, C. P. "Utilization of Thermodynamic Saling Relationships in Hydricity to Develop Nickel Hydrogen Evolution Reaction Electrocatalysts with Weak Acids and Low Overpotentials" *ACS Catalysis*, **2018**, *8*, 9596-9603.

Waldie, K. M.;[‡] Ostericher, A. L.;[‡] Reineke, M.; Sasayama, A. F.; Kubiak, C. P. "Hydricity of Transition-Metal Hydrides: Thermodynamic Considerations for CO₂ Reduction" *ACS Catalysis*, **2018**, *8*, 1313-1324. [‡]Co-first authors

Zhanaidarova, A.; Ostericher, A. L.; Miller, C. J.; Jones, S. C.; Kubiak, C. P. "Selective Reduction of CO₂ to CO by a Molecular Re(ethynyl-bpy)(CO)₃Cl Catalyst and Attachment to Carbon Electrode Surfaces" *Organometallics*, **2019**, *38* (6), 1204–1207.

Reineke, M. H.; Porter, T. M.; Ostericher, A. L.; Kubiak, C. P. "Synthesis and Characterization of Heteroleptic Ni(II) Bipyridine Complexes Bearing Bis(N-heterocyclic carbene) Ligands" *Organometallics*, **2018**, *37* (3), 448-453.

Porter, T. M.; Ostericher, A. L.; Kubiak, C. P. "Steric and Electronic Control of an Ultrafast Isomerization" *Chemical Science*, **2019**, Just Accepted.

ABSTRACT OF THE DISSERTATION

Thermodynamic Strategies of Electrocatalyst Design for CO₂ Reduction

by

Andrew L. Ostericher

Doctor of Philosophy in Chemistry

University of California San Diego, 2019

Professor Clifford P. Kubiak, Chair

The electrocatalytic reduction of CO₂ represents a possible means of disrupting current petrochemical reliance by leveraging renewably-generated electricity to manufacture commodity chemicals and liquid fuels. Such an approach may enable economic feasibility of anthropogenic climate change mitigation by catalytic conversion of atmospheric CO₂ to value-added products. However, many of the most active catalysts consist of rare metals whose cost renders them prohibitively expensive for scalability. Additionally, a wide distribution of reduction products is often possible and poor selectivity decreases overall efficiency and complicates downstream purification processes. Fundamental understanding of elementary steps involved in catalytic

pathways may therefore allow for improved catalyst design from inexpensive, earth-abundant materials.

One such elementary step consists of hydride transfer from a catalyst intermediate to CO₂, yielding the two-electron reduction product, formate. The investigation, targeting, and tuning of the thermodynamics of such hydride intermediates to enable improved catalyst design represents the overarching aim of the work presented herein, which is underpinned by three distinct objectives. Firstly, a powerful scaling relationship is elucidated which relates the thermodynamic propensity of hydride transfer, hydricity (ΔG_{H-}°), and the first reduction potential of the parent metal complex ($E_{1/2}(M^{n+/(n-1)+})$). This relationship not only establishes a mechanism for estimating hydricity based on $E_{1/2}(M^{n+/(n-1)+})$ but also provides a platform for rationally targeting and tuning hydride intermediates for reactivity towards CO₂ and proton sources.

This scaling relationship is subsequently utilized to target and design reactive hydrides at nickel and the validity of the relationship is established. Installation of highly electron-donating ligand frameworks demonstrates successful tuning of hydricity at first-row metal complexes and additional thermodynamic arguments enable for the rational selection of mild conditions for both electrocatalytic hydrogen evolution at extremely low overpotentials and the complete suppression thereof.

Finally, the electrocatalytic reactivity of these species with CO₂ is described. While development of nickel-based CO₂-to-formate catalysts using these methods is ultimately unsuccessful, this work provides insight on the utility and limitations of thermodynamic scaling relationships in catalyst design. Furthermore, the findings herein underscore the necessity of divergence from such scaling relationships and shed light on strategies by which that may be accomplished.

Chapter 1

CO₂ Capture & Utilization: The Necessity and Challenges of Implementing Carbon-Neutral Economies

1.1 The Necessity for Non-Petrochemical Fuel Sources

The prosperity of modern society can be quantified by a host of different metrics. Life expectancy, household incomes, literacy, and accessibility of information have all on average improved for the average human residing in first-world nations since the Industrial Revolution.¹⁻² These quality of life descriptors are buttressed by a single, shared keystone. All of them, and indeed the Industrial Revolution itself, are fundamentally dependent on the efficient production and accessibility of energy sources. In particular, transportation fuels have enabled widespread use of automobiles and air travel, and it is generally accepted that the enhanced mobility of populations has in turn allowed for urbanization and improved access to commodities ranging from healthcare to education.³ The last two centuries have been the age of oil. And the utilization

of petrochemical fuels and feedstocks has directly enabled this mobility leading to booming, global economies.

While the use of energy-dense transportation fuels from petrochemical sources has forged the foundation of modern society, we now face the repercussions of its virtually unchecked growth. There are two main concerns. Firstly, fossil fuel reserves are finite. While estimated extraction of oil reserves may remain inexpensive for the next half century or so, many of the most readily available sources have already been significantly depleted, leading to increased reliance on more challenging methods of extraction and the excavation of less-readily available reserves.⁴ These are often not only more costly but also often involve strategies that are more environmentally detrimental.⁵⁻⁶ This is to say nothing of the uneven global distribution of precious reserves, which has already led to geo-political conflict in the fight for control of such resources.⁷

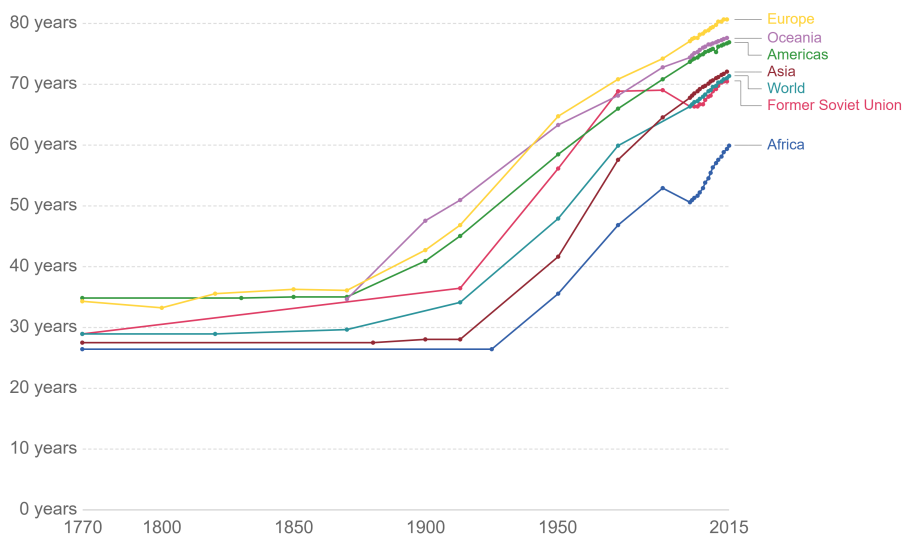


Figure 1.1: Improvements in global life expectancy since 1770. Adapted from references 1-2.

In addition to the fiscally and environmentally expensive toll that the continued extraction of fossil fuels poses, their use thus far has resulted in massive environmental pollution since the Industrial Revolution. The main product of hydrocarbon combustion is CO₂, whose atmospheric concentration has risen to an unprecedented level of ~410 ppm as a result of anthropogenic emissions.⁸⁻¹⁰ These increased levels of CO₂, which currently show no signs of abatement,

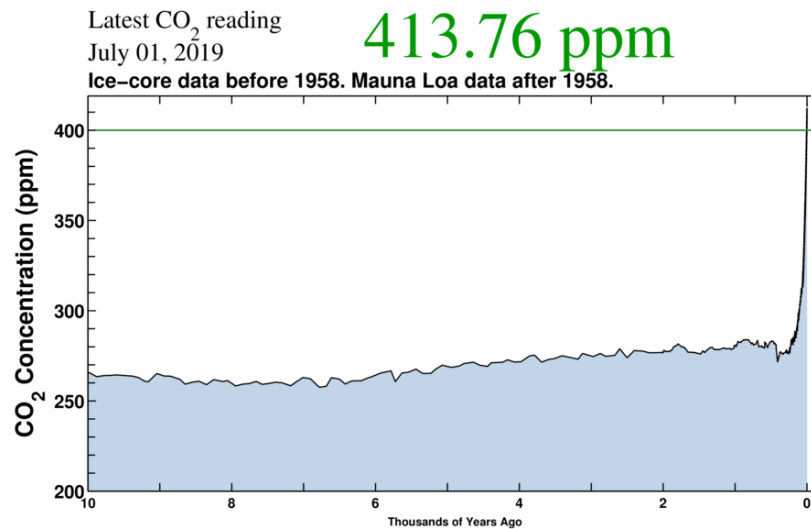


Figure 1.2: Atmospheric CO₂ concentrations for the last 10,000 years. Reproduced with permission from reference 8.

directly contribute to a variety of different environmental issues ranging from climate change as a result of their greenhouse gas properties to ocean acidification. Under current projections, average global temperature increases and other adverse effects related to rising CO₂ levels will yield irreversible environmental changes that will result in the probable extinction of species, food shortages, and increased frequency of extreme weather events. The need for a move away from fossil fuel use is clear.

The implementation of renewable energy sources such as wind and solar have experienced intense growth over the past several decades, but they still make up a small fraction of global energy production.¹¹ However, while increasing the percentage of energy derived from these renewables is absolutely necessary, it represents only half of the problem. While sources such as wind and solar continue to decrease in price, allowing for more economic feasibility of their use, they remain intermittent sources, wherein produced electricity must be directly utilized. As such, the greatest challenge currently facing society's energy problem is one of storage.

Many different approaches to the storage of renewably generated electricity exist. Large-scale flow batteries could serve as energy reservoirs alongside city grids, allowing for charging

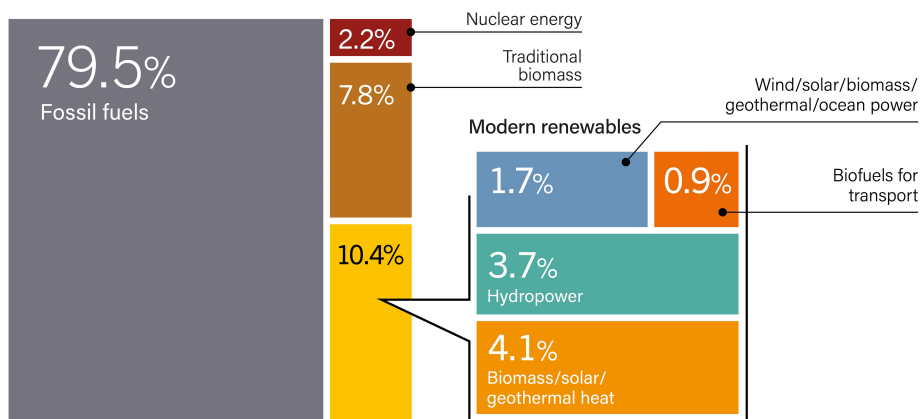


Figure 1.3: Estimated renewable share of total energy consumption from 2016. Adapted from reference 11.

during peak output hours during the day to power grids when solar fields, for instance, are no longer producing after sunset.¹² Alternatively, valuable yet generally cost-prohibitive processes might be driven by excess-produced renewable electricity. Desalination of sea water is energetically expensive, yet extremely valuable especially in areas where extended droughts have been prolific.¹³ As the cost of electrons produced *via* solar fields decreases, applying them to generate fresh water may become both a socially beneficial and economically viable approach to renewable utilization.¹⁴

However, these strategies are typically not well suited to powering transportation. The electrification of small, personal vehicles, such as the typical family car, represents an attractive approach to decreasing fossil fuel dependence provided that efficient grid storage systems can be successfully implemented. But any electric vehicles of this nature require efficient battery storage and therein lies their great limitation.

The energy density of even the most superior batteries is fundamentally limited, and therefore pale in comparison to the energy storage capable per unit mass of liquid fuels. (Figure 1.4) As such, even if relatively short-range transportation can be effectively electrified in coming decades, long range travel and transportation such as air and ship traffic will likely continue to require liquid fuels. While one can envision a variety of liquid fuels and reasonable cycles for

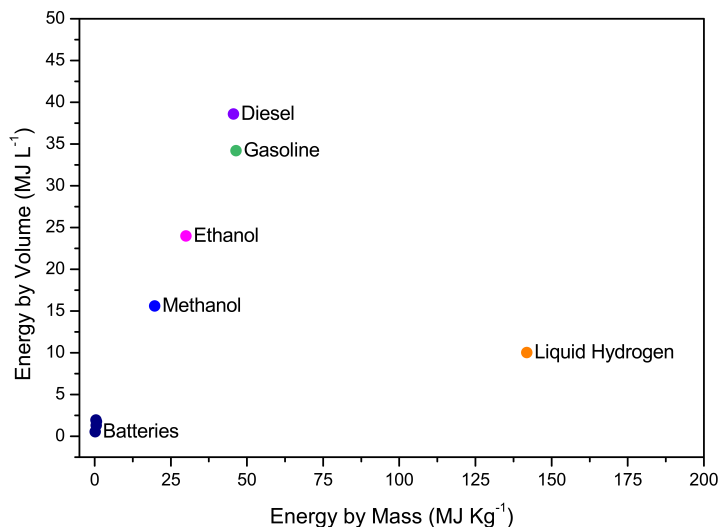


Figure 1.4: Energy density of selected storage methods. “Batteries” encompass average values for lithium-ion, alkaline, nickel-metal hydride, and lead-acid batteries. Data sourced from references 15-17.

their production and utilization, harnessing renewably-generated electricity to capture and convert atmospheric CO₂ represents a logical approach to combat the adverse effects of anthropogenic greenhouse gas emissions while simultaneously producing socially beneficial and economically profitable products. It is the opinion of this author that this marks perhaps the most pressing challenge facing modern society and represents the underlying motivation for the fundamental research presented within this dissertation.

1.2 Potential Routes of CO₂ Conversion to Liquid Fuels

Perhaps the clearest path of generating liquid fuels from a CO₂ reduction product is *via* the Fischer-Tropsch process, wherein a mixture of carbon monoxide and hydrogen, known as SynGas, reacts over a catalyst (typically iron-based) to form a distribution of hydrocarbons.^{18–19} However, the challenge lies in generating carbon monoxide from CO₂. While the thermal route of the Reverse Water-Gas-Shift reaction is capable of yielding CO from CO₂, it is plagued

by inefficiency, precluding true viability of such a pathway.²⁰ The invention of new, catalytic pathways from CO₂ to liquid fuels or precursors thereof is of absolute necessity in order to realize the goal of CO₂ utilization.

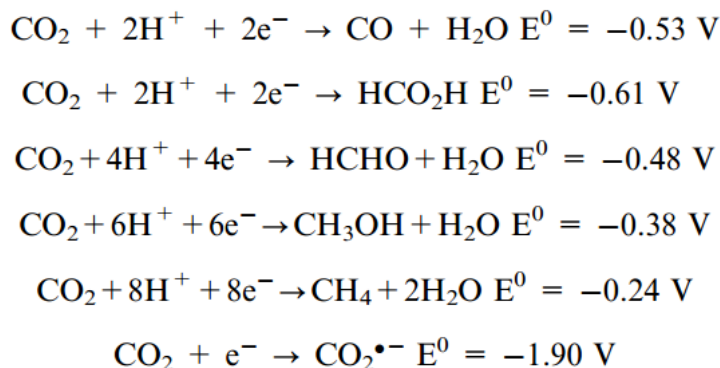


Figure 1.5: Standard reduction potentials of CO₂ to various products at standard conditions in aqueous solution vs. NHE.

Though a variety of catalytic pathways for the reduction of CO₂ can be envisioned, electrocatalytic approaches are particularly advantageous due to generally increased efficiencies, ease of direct use of renewably generated electricity, and atom economy.²¹ However, achieving efficient electrocatalytic reduction of CO₂ is by no means trivial, involving a plethora of both thermodynamic and kinetic challenges. While the thermodynamic reduction potential for many highly-reduced products is quite mild (Figure 1.5),²² the design of single synthetic catalysts capable of choreographing the six-electron, six-proton ballet of CO₂ reduction to methanol, for instance, marks a substantial kinetic challenge.

However, the two-electron reduction products, carbon monoxide and formic acid, are kinetically more accessible. Reflecting this, there exist a multitude of well-studied electrocatalytic systems capable of these two transformations.^{22–28} Furthermore, both reduction products represent economically interesting targets. While CO would likely be more readily implementable, providing a direct route to CO for SynGas in existing Fischer-Tropsch technology, formic acid is also of great interest either as a final product itself for use in fuel cells, or as an initial reduction product in a tandem catalytic pathway to more reduced fuels.²²

1.3 Fundamental Challenges in Catalyst Design

While the two-electron reduction products, CO and formic acid, may be more kinetically accessible, there remain a host of challenges associated with their efficient catalytic production from CO₂ for feasible implementation on an industrial scale. Homogeneous catalyst systems are often not particularly suited to industrial applications due to the difficulty of product separation as well as catalyst recovery and loading. However, they offer an incredible advantage over heterogeneous counterparts in their compatibility with spectroscopic, crystallographic, and solution-state electrochemical techniques which allow for the direct probing of catalyst intermediates and in turn, fundamental mechanistic aspects of such transformations. Such insight thereby enables tuning both kinetic and thermodynamic attributes of catalysts and their reactive intermediates to rationally target highly active and energetically efficient catalytic systems.

In the case of reduction to formic acid, one clear mechanistic pathway to deliver two electrons to CO₂ involves the transfer of a hydride from a transition metal catalyst site. However, as is discussed in detail in Chapter 2, the thermodynamics of this transfer are highly dependent on the electronics at the catalyst metal center and this activity is typically reserved for catalysts consisting of rare and expensive precious metals such as rhodium and iridium. Furthermore, the thermodynamics of hydride transfer are integral to the efficiency of such catalysts, and the fundamental understanding thereof may facilitate the targeted design of similarly effective catalysts consisting of inexpensive, earth-abundant materials.

Efficient catalysts often exhibit relatively level energetic landscapes, wherein catalyst intermediates are thermodynamically well-matched to substrates. This avoids unnecessary energetic barriers and troughs which may bottleneck catalytic pathways. And while reactive catalyst intermediates require reasonable thermodynamic driving force towards substrate reactivity in order to effect exergonic generation of desired products, excess driving force yields energetic inefficiencies manifested in either large overpotentials, energetically costly catalyst regeneration,

or both. Therefore, the rational design of effective and energetically efficient catalysts utilizing earth-abundant materials hinges upon our ability to target catalyst intermediates that reside in Goldilocks thermodynamic regions.

These approaches to the thermodynamic targeting and tuning of reactive hydride intermediates represent the overarching objectives of this body of work. In Chapter 2, the underlying thermodynamic requirements for hydride reactivity with CO_2 , as well as requisites for their generation by thermal or electrocatalytic means is discussed in terms of a variety of pertinent thermochemical relationships. These thermochemical relationships give rise to a particularly useful definition of hydride reactivity. From this, a highly instructive scaling relationship is detailed, which enables not only the prediction of metal hydride reactivity, but also the rational targeting and tuning thereof.

Chapter 3 subsequently details the validation of the utility of this scaling relationship by targeting and tuning reactive hydride intermediates at nickel. These reactivities are shown to be well-modeled by the scaling relationship discussed in Chapter 2, and additional thermochemical arguments regarding proton reactivity are employed to both benchmark quantitative parameters as well as select for highly efficient electrocatalytic hydrogen evolution (HER). This utility is clearly manifested in the demonstration of electrocatalytic overpotentials in a first-generation catalyst that rival the most optimized systems for electrocatalytic HER to date.

Having benchmarked the fundamental hydride thermodynamics in these systems, Chapter 4 seeks to leverage this understanding towards the underlying goal of CO_2 reactivity. While thermodynamic scaling relationships allow for the targeting of reactive intermediates, additional substrate interactions are also possible, which lead to divergent pathways and distinct catalyst selectivity. These reactivities and divergent pathways are discussed as well as the implications for future catalyst design. While development of nickel-based CO_2 -to-formate electrocatalysts is ultimately unsuccessful using these methods, this marks an important step in locating the corners of a puzzle consisting of many moving parts. Reflection on the utility and limitations

of thermodynamic strategies in catalyst design provides insight regarding both the successes and shortcomings of these approaches, which builds a foundation for the construction of new architectures, buttressed not only by intimate understanding of such scaling relationships but also by strategies to breach their confinement.

1.4 References

1. Roser, M., Life Expectancy. In *Published online at OurWorldInData.org*, Retrieved from: ” [Online Resource], 2019.
2. Riley, J. C., Estimates of Regional and Global Life Expectancy, 1800–2001. *Population and Development Review* **2005**, *31* (3), 537-543.
3. Del Rio, M.; Hargrove, W. L.; Tomaka, J.; Korc, M., Transportation Matters: A Health Impact Assessment in Rural New Mexico. *Int J Environ Res Public Health* **2017**, *14* (6), 629.
4. Kerr, R. A., The Next Oil Crisis Looms Large--and Perhaps Close. *Science* **1998**, *281* (5380), 1128.
5. Meng, Q., The impacts of fracking on the environment: A total environmental study paradigm. *Sci. Total Environ.* **2017**, *580*, 953-957.
6. Norris, J. Q.; Turcotte, D. L.; Moores, E. M.; Brodsky, E. E.; Rundle, J. B., Fracking in Tight Shales: What Is It, What Does It Accomplish, and What Are Its Consequences? *Annual Review of Earth and Planetary Sciences* **2016**, *44* (1), 321-351.
7. Froese, R.; Schilling, J., The Nexus of Climate Change, Land Use, and Conflicts. *Current Climate Change Reports* **2019**, *5* (1), 24-35.
8. Keeling, R. F. K., Charles D., Atmospheric Monthly In Situ CO₂ Data - Mauna Loa Observatory, Hawaii. *Scripps CO₂ Program Data* **2017**.
9. Lüthi, D.; Le Floch, M.; Bereiter, B.; Blunier, T.; Barnola, J.-M.; Siegenthaler, U.; Raynaud, D.; Jouzel, J.; Fischer, H.; Kawamura, K.; Stocker, T. F., High-resolution carbon dioxide concentration record 650,000–800,000 years before present. *Nature* **2008**, *453*, 379.
10. MacFarling Meure, C.; Etheridge, D.; Trudinger, C.; Steele, P.; Langenfelds, R.; van Ommen, T.; Smith, A.; Elkins, J., Law Dome CO₂, CH₄ and N₂O ice core records extended to 2000 years BP. *Geophysical Research Letters* **2006**, *33* (14).
11. Renewables 2018 Global Status Report (Paris: REN21 Secretariat), 2018.
12. Soloveichik, G. L., Flow Batteries: Current Status and Trends. *Chemical Reviews* **2015**, *115* (20), 11533-11558.
13. Tzen, E.; Morris, R., Renewable energy sources for desalination. *Solar Energy* **2003**, *75* (5), 375-379.

14. Paul Denholm, M. O. C., Gregory Brinkman, and Jennie Jorgenson, Overgeneration from Solar Energy in California: A Field Guide to the Duck Chart. National Renewable Energy Laboratory, 2015.
15. *Module 1, Hydrogen Properties*; College of the Desert: 2001.
16. IOR Energy. List of common conversion factors (Engineering conversion factors). [Accessed 7/5/2019].
17. Panasonic *Overview of lithium ion batteries*; 2007.
18. Ail, S. S.; Dasappa, S., Biomass to liquid transportation fuel via Fischer Tropsch synthesis – Technology review and current scenario. *Renewable and Sustainable Energy Reviews* **2016**, *58*, 267-286.
19. Jahangiri, H.; Bennett, J.; Mahjoubi, P.; Wilson, K.; Gu, S., A review of advanced catalyst development for Fischer–Tropsch synthesis of hydrocarbons from biomass derived syn-gas. *Catalysis Science & Technology* **2014**, *4* (8), 2210-2229.
20. A. Daza, Y.; N Kuhn, J., *CO₂ conversion by reverse water gas shift catalysis: Comparison of catalysts and mechanisms and their consequences for CO₂ conversion to liquid fuels*. 2016; Vol. 6.
21. De Luna, P.; Hahn, C.; Higgins, D.; Jaffer, S. A.; Jaramillo, T. F.; Sargent, E. H., What would it take for renewably powered electrosynthesis to displace petrochemical processes? *Science* **2019**, *364* (6438), eaav3506.
22. Benson, E. E.; Kubiak, C. P.; Sathrum, A. J.; Smieja, J. M., Electrocatalytic and homogeneous approaches to conversion of CO₂ to liquid fuels. *Chemical Society Reviews* **2009**, *38* (1), 89-99.
23. Machan, C. W.; Sampson, M. D.; Chabolla, S. A.; Dang, T.; Kubiak, C. P., Developing a Mechanistic Understanding of Molecular Electrocatalysts for CO₂ Reduction using Infrared Spectroelectrochemistry. *Organometallics* **2014**, *33* (18), 4550-4559.
24. Smieja, J. M.; Sampson, M. D.; Grice, K. A.; Benson, E. E.; Froehlich, J. D.; Kubiak, C. P., Manganese as a substitute for rhenium in CO₂ reduction catalysts: the importance of acids. *Inorg Chem* **2013**, *52* (5), 2484-91.
25. Lilio, A. M.; Reineke, M. H.; Moore, C. E.; Rheingold, A. L.; Takase, M. K.; Kubiak, C. P., Incorporation of Pendant Bases into Rh(diphosphine)₂ Complexes: Synthesis, Thermodynamic Studies, And Catalytic CO₂ Hydrogenation Activity of [Rh(P₂N₂)₂]⁺ Complexes. *J. Am. Chem. Soc.* **2015**, *137* (25), 8251-60.

26. Roy, S.; Sharma, B.; Pécaut, J.; Simon, P.; Fontecave, M.; Tran, P. D.; Derat, E.; Artero, V., Molecular Cobalt Complexes with Pendant Amines for Selective Electrocatalytic Reduction of Carbon Dioxide to Formic Acid. *J. Am. Chem. Soc.* **2017**, *139* (10), 3685-3696.
27. Costentin, C.; Robert, M.; Savéant, J.-M., Catalysis of the electrochemical reduction of carbon dioxide. *Chemical Society Reviews* **2013**, *42* (6), 2423-2436.
28. Costentin, C.; Drouet, S.; Robert, M.; Savéant, J.-M., A Local Proton Source Enhances CO₂ Electroreduction to CO by a Molecular Fe Catalyst. *Science* **2012**, *338* (6103), 90.

Chapter 2

Hydricity of Transition Metal Hydrides: Thermodynamic Considerations for CO₂ Reduction

2.1 Introduction

Transition metal hydride complexes are prolific in organometallic chemistry for both their laboratory and industrial applications. Hydride transfer from reactive metal hydrides is a critical step in a vast array of catalytic and stoichiometric transformations, including hydrogenation,^{1–8} hydrosilylation,^{9–10} olefin isomerization,¹¹ and hydroformylation¹² reactions. Additionally, within the scope of renewable energy storage *via* the production of chemical fuels, the use of transition metal hydrides for electrochemical H₂ evolution^{13–15} and the chemical^{16–22} or electrocatalytic^{7,23–25} reduction of CO₂ to carbon-based fuels is of particular interest. A key step for these reactions is formal hydride transfer from the metal hydride complex to a substrate, and thus hydride donor ability is a critical descriptor of metal hydride reactivity.

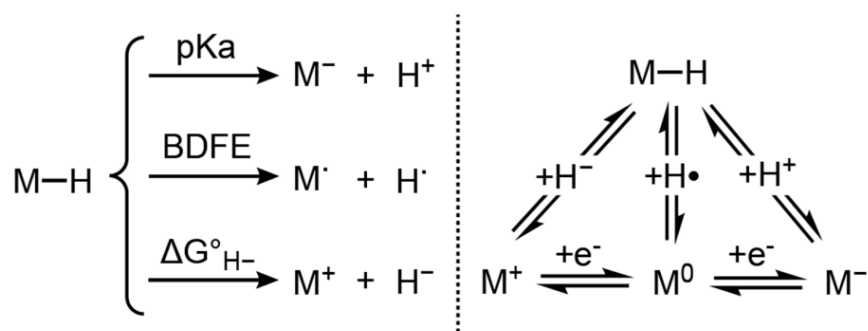
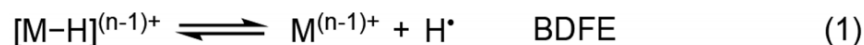


Figure 2.1: Modes of metal hydride bond dissociation.

Hydride donor ability, or hydricity ΔG_{H-}° , of a metal hydride $[M-H]^{(n-1)+}$ is formally defined as the heterolytic bond dissociation free energy of the metal hydride bond to yield the parent metal complex $[M]^{n+}$ and the hydride anion.²⁶ Cleavage of the metal hydride bond may also occur *via* homolytic dissociation to a hydrogen atom or heterolytic dissociation to a proton, given by the bond dissociation free energy (BDFE) or pK_a , respectively. These three metal hydride cleavage modes are depicted in Figure 2.1. Hydricity, BDFE, and pK_a of a metal hydride are interrelated through thermodynamic cycles involving the one-electron reduction potentials of the parent metal complex $[M]^{n+}$ and the known thermodynamic parameters for a hydride, hydrogen atom, and proton.²⁷ The relationship between these parameters is shown schematically in Figure 2.1.

The thermodynamic hydricities for a large number of transition metal hydrides have been experimentally determined in acetonitrile²⁷ and water.^{28–33} These measurements are generally performed by three common approaches for transition metal hydrides: (a) determining the equilibrium constant for the reaction of the metal hydride with a hydride acceptor of known hydricity; (b) establishing the pK_a of the metal hydride and the two-electron reduction potential for the $M^{n+}/(n-2)^+$ redox couple of the parent complex; or (c) measuring the equilibrium constant for H_2 heterolysis in the presence of a base for which the pK_a of the conjugate acid is known. Further details and experimental considerations regarding these approaches have been recently described by Wiedner and co-workers in an excellent review.²⁷

From Figure 2.1, there is an additional possible method for the determination of ΔG_{H-}° based on a thermochemical cycle using the BDFE. This approach is outlined in Figure 2.2. Here, the sum of the metal hydride BDFE, the free energy for the one-electron reduction of the parent complex $E_{1/2}(M^{n+/(n-1)+})$, and the free energy for reduction of a hydrogen atom to a hydride anion $\Delta G_{H\cdot/H-}^{\circ}$ yields the thermodynamic hydricity, given by equations (1) – (5), respectively. In acetonitrile, $\Delta G_{H\cdot/H-}^{\circ}$ is estimated to be 26.0 kcal mol⁻¹.³⁴ This relationship has been previously noted in the literature, but has not been applied to obtain hydricities for metal hydride complexes. The limited application of this relationship is attributed to the need for a reversible $E_{1/2}(M^{n+/(n-1)+})$ couple, which, especially for early transition metals, is often complicated by the instability of the reduced form $M^{(n-1)+}$ and by favorable solvation of the parent complex M^{n+} . This relationship has, however, been used to measure the hydride donor ability of various organic hydrides including NADH analogues.³⁵ While this approach has found limited practical utility for determining ΔG_{H-}° of transition metal complexes, we believe equation (5) to be one of the most informative and predictive relationships for hydride donor abilities of metal hydrides.



$$\Delta G_{H-}^{\circ} = \text{BDFE} + nFE_{1/2}(M^{n+/(n-1)+}) + \Delta G_{H\cdot/H-}^{\circ} \quad (5)$$

Figure 2.2: Hydricity in terms of BDFE and $E_{1/2}(M^{n+/(n-1)+})$.

Equation (5) predicts that for metal hydride bonds with similar BDFE, there is a linear relationship between hydricity and the first reduction potential. Such a direct correlation has been recognized before. Indeed, several theoretical reports have discussed this and other relationships between hydricity and other thermodynamic parameters for hydride systems.^{26,36–44} Notably,

Rousseau and co-workers^{36–38} have developed computational methods for the accurate calculation of hydricity for a series of nickel bis(diphosphine) hydrides and showed that the linear correlation according to equation (5) is valid in this dataset. From an experimental standpoint, a strong linear dependence of measured ΔG_{H-}° with $E_{1/2}(M^{n+/(n-1)+})$ was originally reported for six nickel hydrides bearing bidentate phosphine ligands,⁴⁵ which was later extended to include other closely related nickel bis(diphosphine) complexes.^{27,46–47} An analogous series of five palladium-hydride complexes exhibits similar behavior.⁴⁸ However, with the exception of limited comparisons of isostructural Group 10 hydrides,⁴⁹ cross-period analysis of experimental hydricities has been largely absent. Building upon this previous work, we sought to analyze the experimentally determined thermodynamic hydricities for a larger and more varied dataset of transition metal hydrides to examine broader trends and probe the generality of the relationship given by equation (5).

To this end, we herein establish a dataset containing transition metal hydrides with known hydricity values and reversible $E_{1/2}(M^{n+/(n-1)+})$ in acetonitrile. For this dataset, we find a remarkably strong linear relationship between ΔG_{H-}° and the first reduction potential across the entire dataset according to equation (5), independent of metal identity, dn electron configuration, complex charge, or ligand architecture. Implications of this general correlation on the nature of the metal hydride bond are considered. Furthermore, the significance and limitations of this result towards the prediction of hydricities are discussed in terms of the rational design and optimization of new metal hydride systems for small molecule conversion, and in particular, CO₂ reduction.

2.2 Results & Discussion

2.2.1 Dataset of Metal Hydride Complexes

As the first step towards establishing general trends in the thermodynamic data of metal hydrides, we compiled a comprehensive list of metal hydride complexes for which the hydricity

ΔG_{H-}° and the reduction potential of the $M^{n+/(n-1)+}$ couple are both known in acetonitrile. We stress that our dataset only includes metal hydrides where this first reduction $E_{1/2}(M^{n+/(n-1)+})$ is reversible in order to ensure that only well-characterized numbers are used; thus, many metal hydride complexes with measured hydricities are omitted from this analysis because the one-electron reduction of the parent $[M]^{n+}$ is not reversible. With this strict requirement, there are 51 metal hydrides included in our dataset. Many of these hydrides are included in a recent comprehensive review of hydricity by Wiedner and co-workers, along with other hydride complexes that do not meet our criteria listed above.

The hydricity ΔG_{H-}° and first one-electron reduction potential $E_{1/2}(M^{n+/(n-1)+})$ in acetonitrile for the selected metal hydrides $[M-H]^{(n-1)+}$ and corresponding parent complexes $[M]^{n+}$ in our dataset are summarized in Tables 2.1 – 2.3.⁵⁰ Structures of the parent complexes and associated ligands are presented in Figures 2.3 and 2.4. If solvent (acetonitrile) coordination to the metal follows hydride transfer, the hydricity includes the energetic contribution from solvent coordination. Additional thermodynamic data has been determined for many of these metal hydrides: the pK_a and second one-electron reduction potential $E_{1/2}(M^{n+/(n-1)+})$ are tabulated as well if available. All reduction potentials are reported versus the ferrocenium/ferrocene couple ($Fc^{+/0}$). For a few complexes, acetonitrile values are not available and benzonitrile data are used instead. It has been previously shown that differences between these thermochemical parameters in acetonitrile and benzonitrile are small.³⁴ For several nickel and platinum complexes, more than one hydricity measurement has been reported. In these cases, an averaged value is given in the tables below. Overall, the agreement between the averaged values is excellent.²⁷ Additionally, we note that $[Ni(dmpe)_2]_2^+$ as well as several of the 2nd and 3rd row transition metal complexes in this dataset exhibit a reversible two-electron reduction $E_{1/2}(M^{n+/(n-2)+})$, instead of two sequential one-electron redox couples $E_{1/2}(M^{n+/(n-1)+})$ and $E_{1/2}(M^{(n-1)/(n-2)+})$. In these cases, the first reduction potential $E_{1/2}(M^{n+/(n-1)+})$ is taken to occur at the potential of the overall two-electron process.⁵¹ This assumption does introduce some uncertainty in the reduction

potentials since $E_{1/2}(M^{n+/(n-2)+})$ for a reversible two-electron couple is given by the average of the two one-electron reduction potentials.⁵¹

As seen in Tables 2.1 – 2.3, our dataset includes Group 9 and 10 metal hydrides, as well as two ruthenium examples. The majority of hydricity measurements have been determined for bis(diphosphine) complexes of the general type $[HM(P-P)_2]^{n+}$ or $[HM(P_2^R N_2^{R'})_2]^{n+}$. This ligand architecture has proven to be very amenable to thermodynamic measurements, and systematic variation of the steric and electronic properties of the diphosphine ligands is facile.^{34,45} Nickel bis(diphosphine) complexes represent the largest subset of metal hydrides here. These complexes show two one-electron reductions, except for $[Ni(dmpe)_2]^+$ which exhibits a two-electron reduction at -1.39 V versus $Fc^{+/0}$, the most negative reduction potential in the nickel series.³⁴ Furthermore, the corresponding $[HNi(dmpe)_2]^+$ is the strongest hydride donor of the nickel complexes. As noted by Dubois,⁴⁹ isostructural palladium and platinum hydrides are typically stronger hydride donors (i.e. smaller ΔG_{H-}°) compared to their nickel analogues. Similarly, the hydride donor abilities measured for rhodium bis(diphosphine) complexes are also greater (i.e. smaller ΔG_{H-}°) than that of $[Co(dppe)_2(ACN)]^+$.^{52–56} Furthermore, our dataset also includes metal hydrides that are not based on the bis(diphosphine) architecture, including piano stool complexes of cobalt, iridium, and ruthenium bearing bidentate pyridine or phosphine ligands.

2.2.2 Correlation of Hydricity and Reduction Potential

Dubois and co-workers previously demonstrated that a linear free energy relationship exists between the hydricity ΔG_{H-}° of Ni-hydride complexes $[Ni(P-P)_2H]^+$ and the one-electron reduction potential $E^{II/I}$ of the parent complex $[Ni(P-P)_2]^+$, where P-P are the bidentate phosphine ligands dppv, dppe, dmpp, dedpe, depe, and dmpe.⁴⁵ In this series, as the hydride donor strength of $[Ni(P-P)_2H]^+$ increases, $E^{II/I}$ shifts more positive. A similar linear correlation has been noted for other limited datasets, including series of Ni bis($P_2^R N_2^{R'}$) and Pd bis(diphosphine) hydride complexes.^{26–27,46–48}

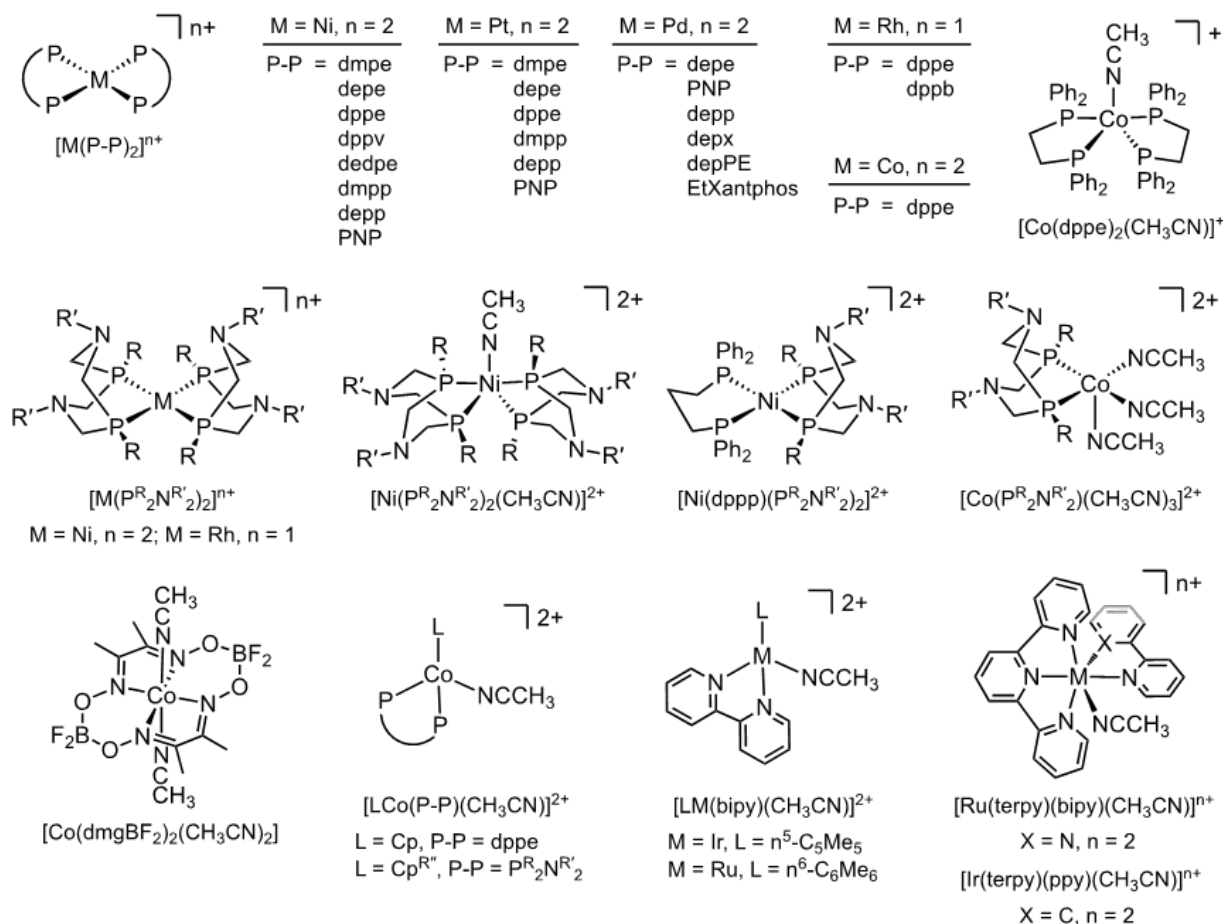


Figure 2.3: Structures and abbreviations for the parent complexes $[M]^{n+}$ of the metal hydrides $[M-H]^{(n-1)+}$.

Beyond these limited experimental reports, no systematic comparison of measured hydricities and one-electron reduction potentials across several transition metals and ligand sets has been discussed in the literature. Figure 2.5 represents the first example of such comparison on a large and varied dataset. In this figure, the hydricity for all of the metal hydrides in our dataset is plotted as a function of the respective $E_{1/2}(M^{n+}/(n-1)^+)$. A linear relationship is clearly demonstrated between the hydricity and reduction potential, which is remarkably independent of metal center and ligand environment. This trend spans a range of over 2 V in reduction potential and approximately 50 kcal mol⁻¹ in hydricity.

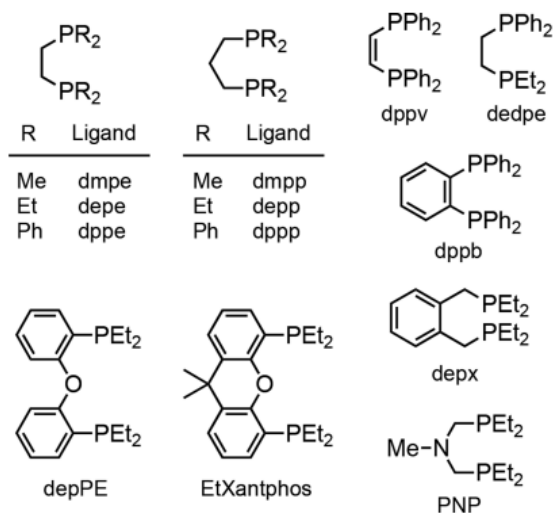


Figure 2.4: Phosphine ligand structures and abbreviations.

The linear correlation in Figure 2.5 can be effectively modeled by equation (5), which describes hydricity as a function of $E_{1/2}(M^{n+/(n-1)+})$ (or $E_{1/2}(M^{n+/(n-2)+})$) in the case of a two-electron reduction potential, *vide supra*) and the BDFE of the metal hydride bond. We note that although the set of equations describing the thermochemical cycle in Figure 2.2 have been developed for standard reduction potentials E_0 , we assume the equivalence of E_0 to the half-wave potential $E_{1/2}$ and use $E_{1/2}$ in place of E_0 for our thermodynamic arguments. By equation (5), ΔG_{H-}° is linearly dependent on the first reduction potential, with the slope of the line equal to nF (23.06 kcal mol⁻¹ V⁻¹ for a one-electron process) and the y-intercept equal to the sum of the metal hydride BDFE and $\Delta G_{H./-}^\circ$ (26.0 kcal mol⁻¹ in acetonitrile, *vide supra*).³⁴ The best-fit line for our dataset has a slope of 20.02 kcal mol⁻¹ V⁻¹, which is in reasonable agreement with the ideal value of 23.06 kcal mol⁻¹ V⁻¹ from equation (5). Defining the slope of the line as 23.06 kcal mol⁻¹ V⁻¹ also gives a similar fit to the data, and this line is plotted in Figure 2.5. We note that when only complexes that exhibit a one-electron reduction $E_{1/2}(M^{n+/(n-1)+})$ and not a two-electron reduction $E_{1/2}(M^{n+/(n-2)+})$ are considered, the slope of the best-fit line is in excellent agreement with the ideal value of 23.06 kcal mol⁻¹ V⁻¹, but the scatter of this smaller dataset is worse (see Figure 2.17 and 2.18).

Table 2.1: Thermodynamic data for nickel complexes.^a

Parent Complex	$E_{1/2}(d^8/d^9)$ (V vs. Fc ^{+ /0})	$E_{1/2}(d^9/d^{10})$ (V vs. Fc ^{+ /0})	ΔG_{H-}° (kcal/mol) ^b	pK _a ^c	Ref
[Ni(dmpe) ₂] ²⁺	-1.39	-1.39	49.3 ^d	24.3 ^e	34, 57
[Ni(P ₂ N ₂ ^R ^{R'}) ₂] ²⁺ ; R = Me, R' = Ph	-1.03	-1.29	54.0	20.5	58
[Ni(depe) ₂] ²⁺	-1.16	-1.29	55.3	23.8 ^e	34, 57
[Ni(P ₂ N ₂ ^R ^{R'}) ₂] ²⁺ ; R = Ph, R' = Me	-0.98	-1.14	55.6 ^f	18.5	46, 59-60
[Ni(P ₂ N ₂ ^R ^{R'}) ₂ (CH ₃ CN)] ²⁺ ; R = nBu, R' = Ph	-0.93	-1.23	57.1	–	47
[Ni(P ₂ N ₂ ^R ^{R'}) ₂ (CH ₃ CN)] ²⁺ ; R = Ph, R' = Bz	-0.94	-1.19	57.2	19.6	61
[Ni(P ₂ N ₂ ^R ^{R'}) ₂ (CH ₃ CN)] ²⁺ ; R = TMP, R' = Ph	-0.89	-1.17	57.6	–	47
[Ni(P ₂ N ₂ ^R ^{R'}) ₂ (CH ₃ CN)] ²⁺ ; R = 2-PhEt, R' = Ph	-0.90	-1.16	57.8	–	47
[Ni(P ₂ N ₂ ^R ^{R'}) ₂ (CH ₃ CN)] ²⁺ ; R = Ph, R' = C6H4-OMe	-0.87	-1.07	58.6	17.4	46
[Ni(P ₂ N ₂ ^R ^{R'}) ₂] ²⁺ ; R = Cy, R' = Bz-OMe	-0.85	-1.39	58.8	22.6	62
[Ni(P ₂ N ₂ ^R ^{R'}) ₂ (CH ₃ CN)] ²⁺ ; R = Ph, R' = Ph	-0.84	-1.02	59.1	16.4	61
[Ni(P ₂ N ₂ ^R ^{R'}) ₂ (CH ₃ CN)] ²⁺ ; R = Bz, R' = Ph	-0.83	-1.12	59.4	–	47
[Ni(dedpe) ₂] ²⁺	-0.99	-1.08	60.0	20.6	45
[Ni(P ₂ N ₂ ^R ^{R'})(P ₂ N ₂ ^R ^{R'})(CH ₃ CN)] ²⁺ ; R = Cy, R' = Ph	-0.76	-1.05	60.5	16.6	46
[Ni(P ₂ N ₂ ^R ^{R'}) ₂ (CH ₃ CN)] ²⁺ ; R = Cy, R' = Bz	-0.80	-1.28	60.9	21.5	61
[Ni(dmpp) ₂] ²⁺	-0.89	-1.33	60.9 ^d	23.9 ^e	34, 57
[Ni(P ₂ N ₂ ^R ^{R'}) ₂] ²⁺ ; R = Cy, R' = tBu	-0.81	-1.45	61.0	24.5	63
[Ni(dppe) ₂] ²⁺	-0.70	-0.88	62.8	14.4	34
[Ni(P ₂ N ₂ ^R ^{R'}) ₂ (CH ₃ CN)] ²⁺ ; R = Cy, R' = Ph	-0.62	-1.09	63.7	17.3	46
[Ni(depp) ₂] ²⁺	-0.61	-1.34	66.7 ^d	23.3	57, 61
[Ni(PNP) ₂] ²⁺	-0.64	-1.24	66.9	22.5	61
[Ni(dppv) ₂] ²⁺	-0.52	-0.83	67.4	13.9	45
[Ni(dppp)(P ₂ N ₂ ^R ^{R'})] ²⁺ ; R = Ph, R' = Bz	-0.52 ^e	-1.04 ^e	68.2	18.1	46, 64

^aValues in acetonitrile unless otherwise marked; ^bHydricity of the corresponding metal hydride complex;

^cAcidity of the corresponding metal hydride complex; ^dAveraged value; ^eMeasured in benzonitrile; ^fDFT-calculated value.

The correlation between hydricity and $E_{1/2}(M^{n+/(n-1)+})$ implies that the BDFE does not change significantly across this dataset of metal hydride complexes. It has been shown by Beauchamp^{70–72} and others^{45,48,73–76} that homolytic bond dissociation energies of metal hydrides typically do not vary by much (less than 10 kcal mol⁻¹) across a series of complexes compared to the large range of accessible hydricities. This difference has been attributed to the large redistribution of charge associated with heterolytic metal hydride cleavage, and consequently ΔG_{H-}° is much more sensitive to changes in the electronic structure of the metal hydride.⁵⁵ Furthermore, variations in BDFE are largely independent of the identity of the metal center, particularly for heavier atoms. Therefore, the spread from the model line in Figure 2.5 is small.

Table 2.2: Thermodynamic data for palladium and platinum complexes.^a

Parent Complex	$E_{1/2}(d^8/d^9)$ (V vs. $Fc^{+/0}$)	$E_{1/2}(d^9/d^{10})$ (V vs. $Fc^{+/0}$)	ΔG_{H-}° (kcal/mol) ^b	pK_a ^c	Ref
[Pt(dmpe) ₂] ²⁺	-1.73 ^d	-1.73 ^d	41.8 ^e	31.1	34, 57
[Pd(depe) ₂] ²⁺	-1.48	-1.48	43.0	23.2	48
[Pt(depe) ₂] ²⁺	-1.65	-1.65	44.0	29.7	34, 57
[Pt(dmpp) ₂] ²⁺	-1.53	-1.53	50.6 ^e	30.4	34, 57
[Pd(PNP) ₂] ²⁺	-1.21	-1.21	50.7	19.7	49
[Pt(dppe) ₂] ²⁺	-1.24	-1.24	52.8	22.3	34
[Pt(depp) ₂] ²⁺	-1.4 ^d	-1.4 ^d	53.7	–	57
[Pt(PNP) ₂] ²⁺	-1.36	-1.36	54.3	27.4	49
[Pd(depp) ₂] ²⁺	-1.22	-1.22	54.6	22.9	48
[Pd(depx) ₂] ²⁺	-0.94	-1.02	61.8	20.1	48
[Pd(depPE) ₂] ²⁺	-0.73	-0.92	66.9	18.6	48
[Pd(EtXantphos) ₂] ²⁺	-0.55	-0.94	70.9	18.8	48

^aValues in acetonitrile unless otherwise marked; ^bHydricity of the corresponding metal hydride complex;

^cAcidity of the corresponding metal hydride complex; ^dAveraged value; ^eMeasured in benzonitrile; ^fDFT-calculated value.

An average BDFE of 51 kcal mol⁻¹ for the metal hydrides in our dataset can be calculated from the y-intercept of the best-fit line in Figure 2.5. This BDFE is in good agreement with the value of 60 kcal mol⁻¹ commonly cited for the typical bond strength of transition metal hydrides.^{74–75,77} We note that two complexes with known hydricities have not been included in Figure 2.5: the hydricities of [Rh(depx)₂]⁺ and [Pt(EtXanphos)₂]²⁺ deviate considerably from this linear trend (Figure 2.19). In both cases, the chelate bite angle of these rigid bidentate phosphine ligands causes a large distortion from an ideal square planar geometry in the parent complexes, which stabilizes the lowest unoccupied molecular orbital (LUMO) and increases the hydride accepting ability.^{55,78}

Because the linear trend in Figure 2.5 is valid over a wide range of complexes with different metals and ligand structures, we expect other transition metal hydrides to approximately follow this qualitative trend as well. Therefore, this correlation may be utilized to approximate the hydricity of metal hydride complexes simply based on the measured reduction potential of the parent complex [M]ⁿ⁺, which can be obtained by cyclic voltammetry or other electrochemical

Table 2.3: Thermodynamic data for group eight and nine complexes. ^a

Parent Complex	$E_{1/2}(d^8/d^9)$ (V vs. $\text{Fc}^{+/0}$)	$E_{1/2}(d^9/d^{10})$ (V vs. $\text{Fc}^{+/0}$)	ΔG_{H-}° (kcal/mol) ^b	pK_a ^c	Ref
$[\text{Rh}(\text{P}_2^{\text{R}}\text{N}_2^{\text{R}'})_2]^+$; R = Ph, R' = Bz	-2.43	-2.43	28.4	44.6	52
$[\text{Rh}(\text{P}_2^{\text{R}}\text{N}_2^{\text{R}'})_2]^+$; R = Cy, R' = C6H4-OMe	-2.45	-2.45	30.2	46.6	52
$[\text{Rh}(\text{P}_2^{\text{R}}\text{N}_2^{\text{R}'})_2]^+$; R = Ph, R' = C6H4-OMe	-2.27	-2.27	31.3	31.3	52
$[\text{Rh}(\text{P}_2^{\text{R}}\text{N}_2^{\text{R}'})_2]^+$; R = Cy, R' = Ph	-2.39	-2.39	31.9	45.8	52
$[\text{Rh}(\text{dppb})_2]^+$	-2.02	-2.02	34.0	34.9	53
$[\text{Rh}(\text{dppe})_2]^+$	-2.12	-2.12	38.6 ^d	–	53-54
$[\text{Ru}(\text{terpy})(\text{bipy})(\text{CH}_3\text{CN})]^{2+}$	-1.68 ^f	-1.98 ^e	39.3	32.4	26
$[\text{Ir}(\text{terpy})(\text{ppy})(\text{CH}_3\text{CN})]^{2+}$	-1.33 ^f	–	43.2 ^d	–	65
$[\text{Co}(\text{dppe})_2]^+$	-1.56	-2.03	49.1	38.1	56
$[(\eta^6\text{-C}_6\text{Me}_6)\text{Ru}(\text{bipy})(\text{CH}_3\text{CN})]^{2+}$	-1.22 ^f	-1.22 ^e	54.0	22.5	26
$[\text{Co}(\text{P}_2^{\text{R}}\text{N}_2^{\text{R}'})_2(\text{CH}_3\text{CN})_3]^{2+}$; R = tBu, R' = Ph	-0.87 ^e	–	54.2 ^d	–	66
$[\text{Co}(\text{dmgBF}_2)_2(\text{CH}_3\text{CN})_2]$	-0.91 ^e	–	55.9 ^d	–	66
$[\text{Co}(\text{dppe})_2(\text{CH}_3\text{CN})]^{2+}$	-0.70 ^e	-1.56 ^g	59.7	23.6	56
$[\text{Cp} \cdot \text{Ir}(\text{bipy})(\text{CH}_3\text{CN})]^{2+}$	-1.07 ^{f,h}	-1.07 ^{e,h}	62.0	23.3	67
$[\text{CpCo}(\text{dppe})(\text{CH}_3\text{CN})]^{2+}$	-0.51 ^f	-0.93 ^e	71.5	18.4	68

^aValues in acetonitrile unless otherwise marked; ^bHydricity of the corresponding metal hydride complex;

^cAcidity of the corresponding metal hydride complex; ^dAveraged value; ^eMeasured in benzonitrile; ^fDFT-calculated value,

^e $E(d^7/d^8)$; ^f $E(d^6/d^7)$; ^g $E(d^8/d^9)$; ^hQuasi-reversible redox couple.

methods. This proposal was previously put forth by Rousseau and co-workers³⁶ for a series of nickel hydrides based on their experimental and DFT-calculated dataset of hydricities. A similar approach using a smaller dataset was recently applied to roughly estimate ΔG_{H-}° for three Co-hydride complexes.⁷⁹ Furthermore, investigations into how systematic ligand substitutions shift reduction potentials have been reported for several ligand classes.^{80–84} Thus, starting from a metal hydride in our dataset, the effect of ligand substitution on the hydricity can be estimated, providing a rational guide for the design of new metal hydrides with targeted hydricities.

The homolytic bond dissociation free energy of a metal hydride is also related to the free energy of proton dissociation of the metal hydride bond and the second one-electron reduction potential of the parent complex $E_{1/2}(M^{(n-1)/(n-2)+})$, as given by Figure 2.7.⁷³ Considering the small variation in BDFE across our dataset, we expect an equivalent linear correlation to exist between the pK_a of the metal hydride and the second reduction potential, with the slope of the line

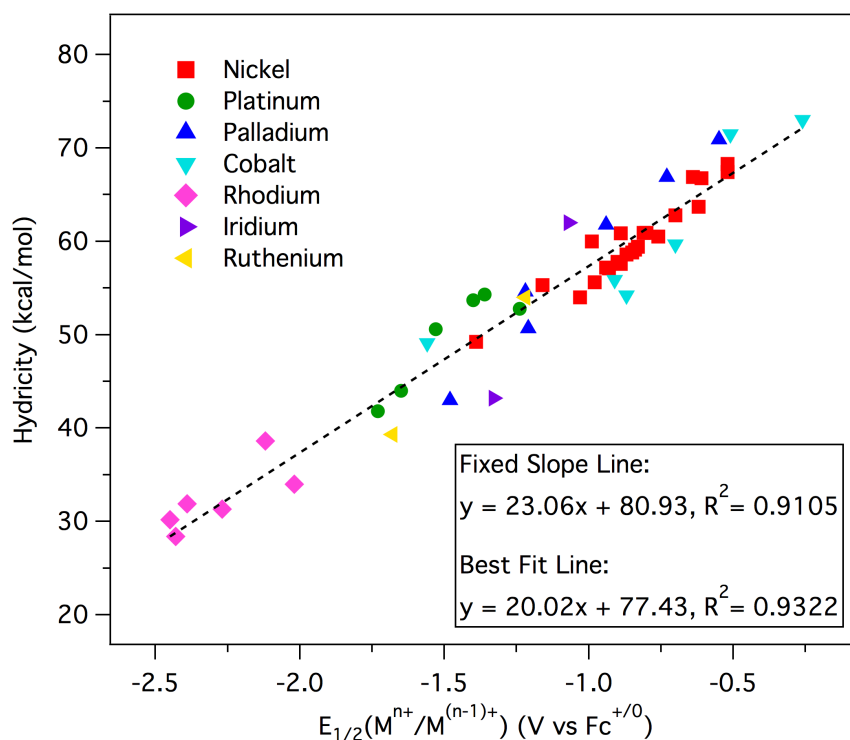


Figure 2.5: Correlation of ΔG_{H-}° with the first one-electron reduction potential of the parent metal complex. Fixed slope line given by black dashed trace.

being $-nF$ ($-23.06 \text{ kcal mol}^{-1} \text{ V}^{-1}$) and the y-intercept being the sum of the metal hydride BDFE and $\Delta G_{H+/H}^{\circ}$ ($53.6 \text{ kcal mol}^{-1}$ in acetonitrile).⁸⁵ The free energies of proton dissociation, given by $1.364 \times \text{pK}_a$, is plotted a function of $E_{1/2}(M^{(n-1)/(n-2)+})$ in Figure 2.6. Similar to above, the half-wave potential $E_{1/2}$ for the $M^{(n-1)/(n-2)+}$ (or $M^{n+/(n-2)+}$ for a two-electron reduction) is used in place of the standard reduction potential E_0 in this thermochemical cycle. As expected, a linear trend is observed with a slope of $-25.38 \text{ kcal mol}^{-1} \text{ V}^{-1}$. Modeling the data by equation (9) with a fixed slope of $-23.06 \text{ kcal mol}^{-1} \text{ V}^{-1}$ also shows reasonable agreement, and this line is plotted in Figure 2.6.

Equations (5) and (9) provide two methods for calculating the BDFE of the metal hydride bond from either of the heterolytic dissociation energies: hydricity or pK_a . The self-consistency of our dataset is demonstrated by comparing the BDFE value for each metal hydride calculated using equation (5) versus equation (9). Complexes for which the hydricity was calculated

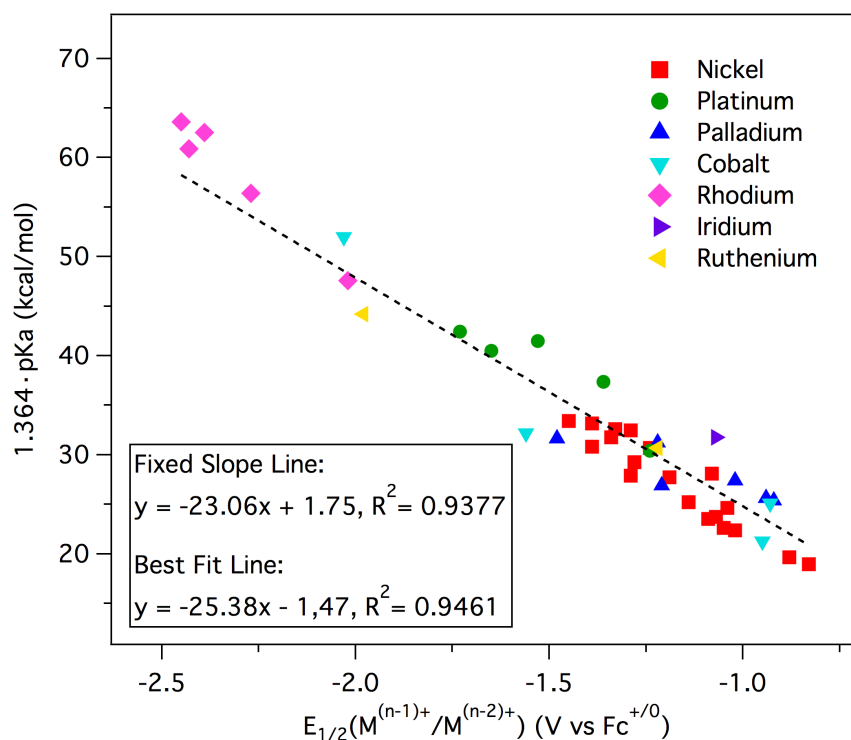


Figure 2.6: Correlation of pK_a with the second reduction potential of the parent metal complex. Fixed slope line given by black dashed trace.

from an experimentally determined pK_a (i.e. the “potential- pK_a ” method)²⁷ or the pK_a was calculated from an experimentally determined ΔG_{H-}° were excluded from this analysis in order to avoid drawing conclusions from circular mathematical relationships. This comparison is shown graphically in Figure 2.20. As expected, the slope and y-intercept for this data equal one and zero within error, respectively.

2.2.3 Expansion to Other Hydride Classes

The chemical reactivity and biological activity of natural organic hydride donors and related synthetic derivatives have been the subject of much research in recent decades. In nature, hydride transfers are mediated by 1,4-dihydronicotinamide adenine dinucleotide (NADH) and the oxidized form NAD⁺ are critical in many biological transformations.^{86–88} Many related

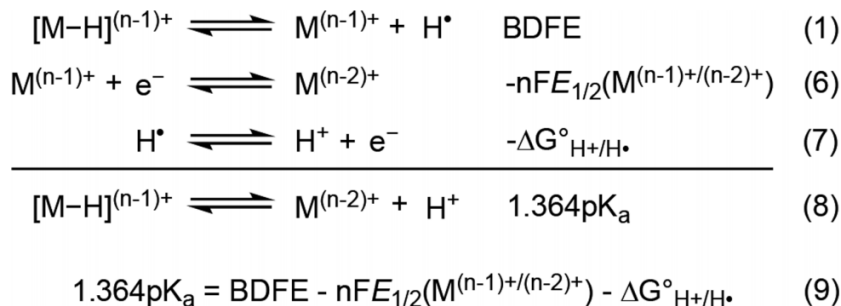


Figure 2.7: Acidity in terms of BDFE and $E_{1/2}(M^{(n-1)+/(n-2)+})$.

nicotinamide compounds have been prepared as structural analogues of NADH for systematic studies on hydricity.^{89–90}

Hydride transfer from an organic hydride donor is directly analogous to that from a metal hydride complex; thus, the same equations given above for relating the thermodynamic parameters for a metal hydride bond can also be applied to organic hydride donors. Here, we extend our hydricity dataset to include several organic hydrides that fall into two general categories: NADH analogues and arylmethanes.^{35,91–92} For these compounds, the reactive hydride bond in question is a carbon-hydrogen bond, and the parent complex is the corresponding organic cation R^+ . The hydricity $\Delta G^\circ_{H^-}$ and first one-electron reduction potential $E_{1/2}(R^{+/0})$ in acetonitrile for these organic hydride donors are presented in Table 2.5.

Figure 2.8 shows the hydricity of the NADH compounds and arylmethanes plotted as a function of $E_{1/2}(R^{+/0})$. Similar to the metal hydride dataset, a linear correlation exists between $\Delta G^\circ_{H^-}$ and the first reduction potential, and this relationship is well described by equation (5) with the slope of the line equal to nF ($23.06 \text{ kcal mol}^{-1} \text{ V}^{-1}$). As stated previously, the reversible reduction potential $E_{1/2}(R^{+/0})$ is assumed to be equivalent to the standard reduction potential E_0 . The agreement between the thermodynamic data for the organic hydrides and the model given by equation (5) is better compared to that of the metal hydrides due to the smaller range of homolytic bond strengths for the carbon-hydrogen bonds in this series. This result demonstrates the general utility of this approach for visualizing trends in the thermodynamic parameters of hydride donors.

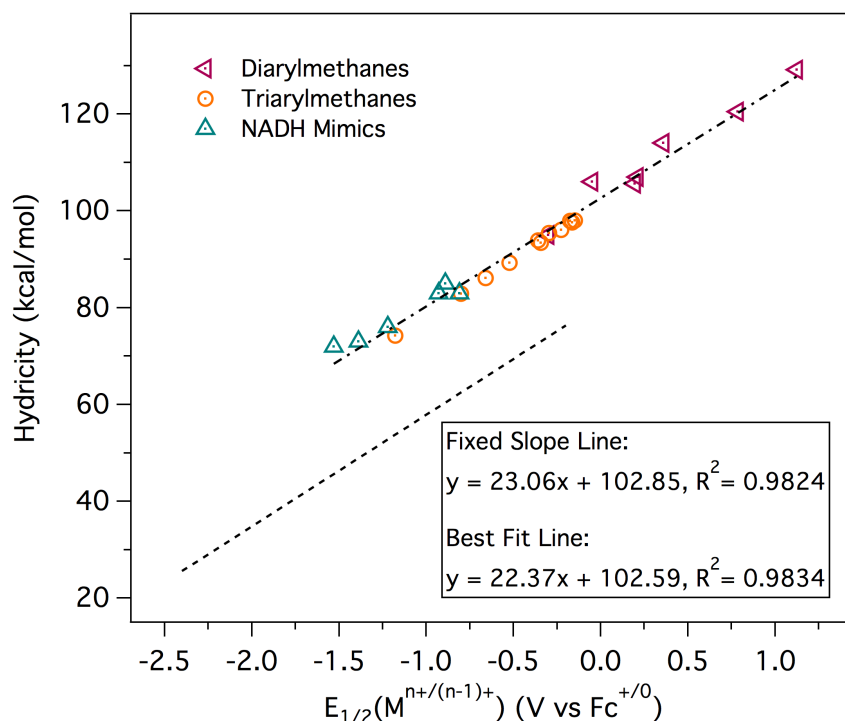


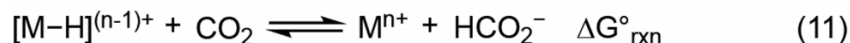
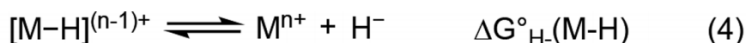
Figure 2.8: Correlation of $\Delta G_{H^-}^\circ$ with the first one-electron reduction potential for organic compounds. Fixed slope line for metal hydrides given by lower black dashed trace.

Comparing the fixed slope lines in Figures 2.5 and 2.8, the y-intercept for the organic hydride donor dataset is approximately 22 kcal mol^{-1} higher. Since equation (5) gives that the y-intercept is the sum of the carbon-hydride BDFE and $\Delta G_{H^-}^\circ$, this 22 kcal mol^{-1} difference is the difference in the carbon-hydride versus metal hydride average homolytic bond dissociation free energies. This result is further illustrated in Figure 2.21: the BDFE for each hydride donor was calculated using the model trend line from Figure 2.5 or 2.8 for metal or organic compounds, respectively, and the calculated BDFEs were plotted as a function of the first reduction potential. For both datasets, the BDFEs are only weakly correlated with reduction potential, but fall into two distinct regions for metal or carbon-based hydride donors. This formalism further illustrates that large hydride donor ability is not indicative of a weaker metal hydride bond.

2.2.4 Implications for CO₂ Reduction

Hydride addition to CO₂

The generality of the linear relationship in Figure 2.5 across a large scope of metal hydrides allows for some broad statements to be made regarding the hydricity of a metal hydride catalyst and the reaction conditions required for CO₂ reduction. Reduction of CO₂ to formate using a metal hydride, either via thermal hydrogenation or electrochemical means, requires hydride transfer to CO₂. Without considering the exact mechanism of hydride transfer, it is well established that the overall energy of this transformation can be assessed by comparing the hydricity of the metal hydride to that of formate, given by equations (4) and (10) – (12) in Figure 2.9.^{20,25–27,31,46} Given that the hydricity of formate $\Delta G_{H^-}^{\circ}(\text{HCO}_2^-)$ in acetonitrile is 44 kcal mol⁻¹,²⁵ the hydricity of the metal hydride must be less than 44 kcal mol⁻¹ for $\Delta G_{\text{Rxn}}^{\circ}$ defined by equation (12) to be exergonic. This requirement is shown graphically in Figure 2.10, where the horizontal line establishes a border between metal hydrides capable of hydride donation to CO₂ ($\Delta G_{H^-}^{\circ}(\text{M-H}) < 44$ kcal mol⁻¹) and those expected to accept a hydride from formate ($\Delta G_{H^-}^{\circ}(\text{M-H}) > 44$ kcal mol⁻¹). It is clear that most known metal hydrides are not suitable for CO₂ reduction *via* direct hydride transfer under standard conditions. It is also evident that unassisted organic hydride donors are ineffective for CO₂ reduction since all of these hydricities lie above the horizontal line.



$$\Delta G_{\text{rxn}}^{\circ} = \Delta G_{\text{H}^-}^{\circ}(\text{M-H}) - \Delta G_{\text{H}^-}^{\circ}(\text{HCO}_2^-) \quad (12)$$

Figure 2.9: Hydricity requirements for hydride transfer to CO₂.

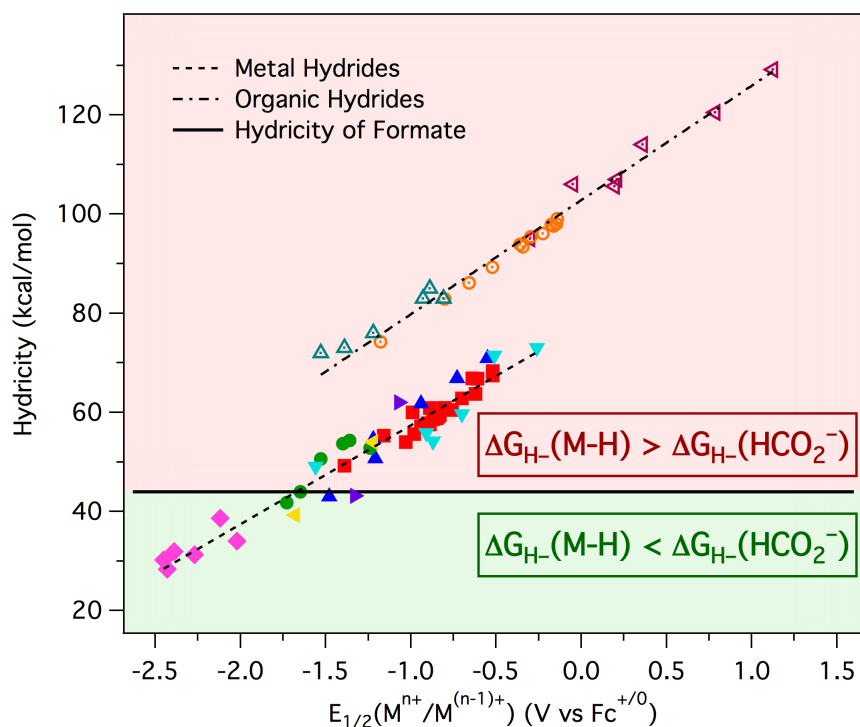
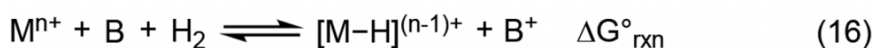
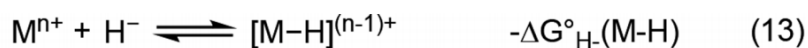


Figure 2.10: Comparison of ΔG_{H-}° of metal hydrides (filled points), organic hydride donors (open points), and formate (solid black trace). Hydricities in the red region fall above $\Delta G_{H-}^{\circ}(\text{HCO}_2^-)$, and are not capable of hydride transfer to CO_2 . Hydricities in the green region fall below $\Delta G_{H-}^{\circ}(\text{HCO}_2^-)$, and are able to reduce CO_2 *via* hydride transfer. Fixed slope line for metal hydrides given by lower black dashed trace. Fixed slope line for organic hydrides given by upper black dashed trace.

CO₂ Hydrogenation: Metal Hydride Generation

A key step often proposed for the hydrogenation of CO_2 to formate with transition metal hydride complexes is generation of the active metal hydride catalyst *via* base-assisted H_2 cleavage through deprotonation of a dihydrogen complex⁹³ or a metal dihydride.⁵² The strength of the base required to facilitate H_2 activation is determined by the hydricity of the metal hydride. This relationship is given by the thermochemical cycles in Figure 2.11, where the hydricity of H_2 is $\Delta G_{H-}^{\circ}(\text{H}_2) = 76.0 \text{ kcal mol}^{-1}$ in acetonitrile.⁵⁷ The minimum strength of the base (i.e. the minimum pK_a of the conjugate acid BH^+) required for H_2 cleavage can thus be calculated for a given hydricity (Figure 2.12), and can be plotted as the right y-axis on the same graph as

$\Delta G_{H-}^{\circ}(\text{M-H})$ versus $E_{1/2}(\text{M}^{n+}/(n-1)^{+})$ (Figure 2.13). From this figure, which may be viewed as a modified Pourbaix diagram, the minimum base strength required for H_2 cleavage is obtained by drawing a horizontal line from a hydricity on the left axis to the corresponding pK_a on the right axis. Thus, this figure not only provides a qualitative guide for the rational tuning of catalyst hydricity, but also directs the selection of an appropriate base for catalysis. For example, if $E_{1/2}(\text{M}^{n+}/(n-1)^{+})$ of the parent complex is known, ΔG_{H-}° of the corresponding metal hydride as well as the associated pK_a required for H_2 activation can be easily estimated. It is clear that for metal hydrides capable of hydride transfer to CO_2 ($\Delta G_{H-}^{\circ} < 44 \text{ kcal mol}^{-1}$), the added base must have $\text{pK}_a(\text{BH}^+) > 23.5$ in acetonitrile for H_2 cleavage to be thermodynamically favorable under standard conditions.



$$\Delta G_{\text{rxn}}^{\circ} = \Delta G_{\text{H}}^{\circ}(\text{H}_2) - \Delta G_{\text{H}}^{\circ}(\text{M-H}) - 1.364\text{pK}_a(\text{BH}^+) \quad (17)$$

Figure 2.11: Strength of the base required for H_2 cleavage for a given hydricity. B = base, BH^+ = conjugate acid of B.

CO_2 Electrocatalytic Reduction: Metal Hydride Generation

The two-electron, two-proton reduction of CO_2 to formic acid in acetonitrile necessarily requires the presence of a Brønsted acid. Protonation of the two-electron reduced parent complex is the typical pathway for electrochemical generation of the metal hydride, which may then transfer the hydride to CO_2 . The pK_a of the Brønsted acid required to protonate $[\text{M}]^{(n-2)+}$ is readily obtained from the pK_a of the metal hydride (Figure 2.6). Under electrocatalytic conditions, protonation of the metal hydride may also occur if the acid is sufficiently strong, resulting in

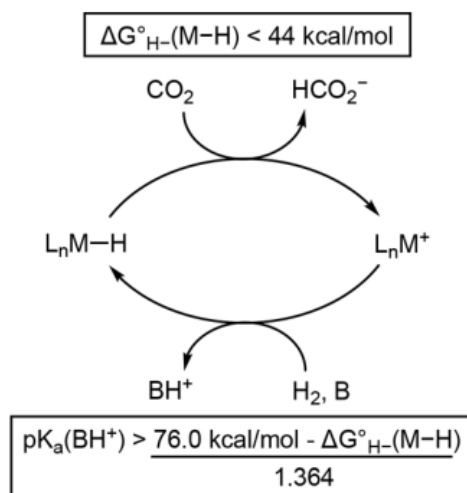


Figure 2.12: Representative catalytic cycle for CO₂ hydrogenation with a metal hydride. Hydrity requirement for favorable CO₂ reduction given by top equation. pK_a requirement for favorable H₂ activation given by bottom equation. B = base, BH⁺ = conjugate acid of B.

competitive H₂ evolution and decreasing the Faradaic efficiency for CO₂ reduction to formic acid. The thermochemical cycles describing H₂ evolution are identical to those shown in Figure 2.11: ΔG°_{rxn} defined by equation (17) must be less than zero in order for competitive H₂ evolution to be thermodynamically unfavorable. Therefore, the maximum acid strength (i.e. the minimum pK_a) for which H₂ generation is endergonic may be estimated for a given ΔG°_{H-} using the same equation in Figure 2.12, and can be plotted as the right y-axis with $\Delta G^{\circ}_{H-}(M-H)$ versus $E_{1/2}(M^{n+}/(n-1)^+)$ in the modified Pourbaix diagram (Figure 2.13). For metal hydrides capable of CO₂ reduction ($\Delta G^{\circ}_{H-} < 44 \text{ kcal mol}^{-1}$), the added acid must have pK_a > 23 in order to thermodynamically avoid H₂ evolution. Furthermore, Figure 2.6 indicates that the metal hydrides with $\Delta G^{\circ}_{H-} < 44 \text{ kcal mol}^{-1}$ generally have pK_a values above 29, thus limiting the possible acids that may be appropriate for CO₂ reduction to approximately $23 < pK_a < 29$.

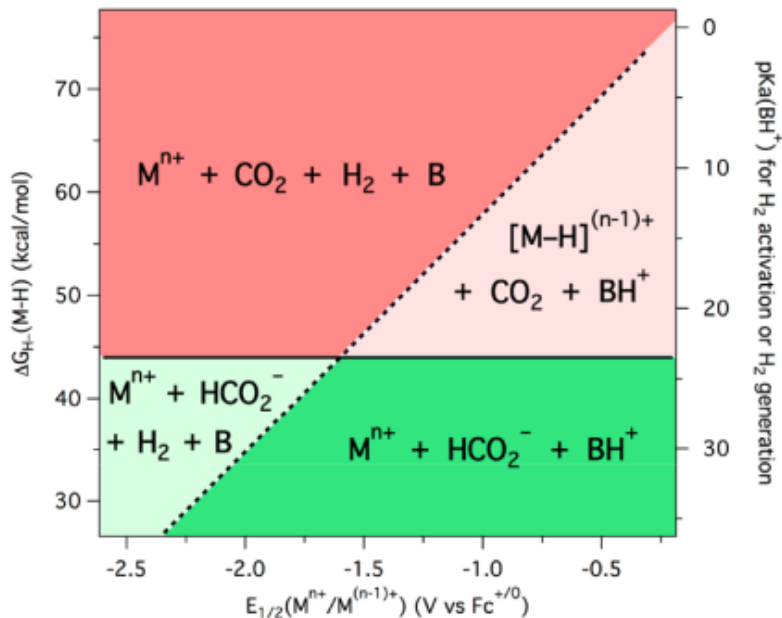
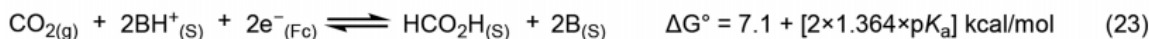
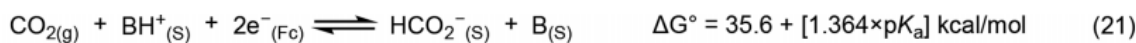


Figure 2.13: Modified Pourbaix diagram indicating the thermodynamic stability of a metal hydride and BH^+ relative to CO_2 and H_2 . For CO_2 hydrogenation, right axis gives the minimum $\text{pK}_a(\text{BH}^+)$ of the added base for heterolytic H_2 cleavage for a given $\Delta G_{H-}^\circ(\text{M-H})$ on the left axis. For electrocatalytic CO_2 reduction, right axis gives the minimum $\text{pK}_a(\text{BH}^+)$ of the added acid to avoid H_2 evolution *via* protonation of a metal hydride with a given $\Delta G_{H-}^\circ(\text{M-H})$ on the left axis. Fixed slope line for metal hydrides given by black dashed trace. Hydricity of formate given by the black solid trace.

CO_2 Electrocatalytic Reduction: Overpotential.

A critical parameter for benchmarking the activity of an electrocatalyst is the overpotential η , which is the difference between the operating potential of the catalyst E_{cat} and the thermodynamic potential for the reaction of interest, E° . The thermodynamic potential for the CO_2 /formic acid couple in aqueous solution is -0.61 V versus NHE at pH 7;⁹⁴ however, to the best of our knowledge, no value for $E^\circ(\text{CO}_2/\text{HCO}_2\text{H})$ in acetonitrile or other organic solvent has been reported. Standard reduction potentials for CO_2/CO and CO_2/CH_4 have been calculated from the well-established aqueous standard potentials and $E^\circ(\text{H}^+/\text{H}_2)$ in acetonitrile.⁹⁵ A similar approach was recently applied to derive the standard reduction potential for N_2 to various reduced products including ammonia.⁹⁶



$$\boxed{E^\circ(\text{CO}_{2(\text{g})}/\text{HCO}_2\text{H}_{(\text{S})}) = -0.15 \text{ V} - 0.059 \text{p}K_a} \quad (24)$$

Figure 2.15: Thermochemical cycle used to estimate $E^\circ(\text{CO}_2/\text{HCO}_2\text{H})$ in acetonitrile. B = base, BH^+ = conjugate acid of B. S = acetonitrile.

Given that the standard reduction potentials for CO_2 reduction to formate and formic acid are known in water, the influence of solvent on these thermodynamic potentials can be evaluated. Table 2.4 summarizes E° for the CO_2 /formate and CO_2 /formic acid couples in both acetonitrile and water, as well as E° for the CO_2 /CO couple for comparison. The protonation of formate to formic acid results in a 0.62 V shift to more positive potential for $E^\circ(\text{CO}_2/\text{HCO}_2\text{H})$ compared to $E^\circ(\text{CO}_2/\text{HCO}_2^-)$. In water, the direction of this potential shift is the same, but the magnitude of the shift is significantly smaller, only 0.116 V. This large variance may be attributed to the difference in the $\text{p}K_a$ scales in acetonitrile solvent versus aqueous solution.⁹⁶ The standard potentials for CO_2 reduction to formic acid or CO very similar in both solvents, with $E^\circ(\text{CO}_2/\text{HCO}_2\text{H})$ occurring at slightly more cathodic potentials compared to $E^\circ(\text{CO}_2/\text{CO})$ in acetonitrile and water.

Table 2.4: Comparison of standard reduction potentials for CO_2 to formate/formic acid or CO.

Reduction Reaction	E°	
	MeCN	H_2O
$\text{CO}_{2(\text{g})}/\text{HCO}_2^-_{(\text{S})}$	$-0.77 \text{ V} - 0.030 \text{p}K_a$	$-0.23 \text{ V} - 0.030 \text{pH}$
$\text{CO}_{2(\text{g})}/\text{HCO}_2\text{H}_{(\text{S})}$	$-0.15 \text{ V} - 0.059 \text{p}K_a$	$-0.114 \text{ V} - 0.059 \text{pH}$
$\text{CO}_{2(\text{g})}/\text{CO}_{(\text{g})}$	$-0.12 \text{ V} - 0.059 \text{p}K_a$	$-0.104 \text{ V} - 0.059 \text{pH}$

The dependence of E° for CO_2 reduction to formate/formic acid on solution acidity is overlaid in Figure 2.16 with the hydricity trend line for metal hydrides as well as the hydricity of formate. The point on the graph at which the $E^\circ(\text{CO}_2/\text{HCO}_2^-)$ and $E^\circ(\text{CO}_2/\text{HCO}_2\text{H})$ lines intersect occurs at the pK_a of formic acid. As previously discussed, for a given hydricity on the left axis, the minimum pK_a of acid to prevent H_2 evolution is defined by the corresponding value on the right axis. The addition of the standard reduction potential variation in Figure 2.16 now also enables E° for formate or formic acid to be readily obtained at a particular $\text{pK}_a(\text{BH}^+)$. The overpotential for CO_2 reduction can then be estimated from the difference between E° at $\text{pK}_a(\text{BH}^+)$ and the operating potential of the metal hydride catalyst, which, for $[\text{M}]^{n+}$ that undergoes a two-electron reduction, is $E_{1/2}(\text{M}^{n+}/(n-1)^+)$, allowing for a set of appropriate reaction conditions and the associated overpotential for CO_2 reduction to be quickly predicted. As expected, the overpotential for electrocatalytic reduction will clearly decrease as weaker acids are used.

Since there is appreciable uncertainty associated with the solvation energy of the hydride anion¹⁰⁰ and the pK_a of formic acid in acetonitrile has not been reported, equations (21) and (24) are at best rough approximations for the standard reduction potential of the CO_2 /formate and CO_2 /formic acid couples. With these caveats in mind, the overpotential for CO_2 reduction using a metal hydride catalyst may be discussed. The approximate set of experimental conditions where CO_2 reduction to formate is viable (*vide supra*) is indicated by the green region in Figure 2.16. Within this region, if we consider a hypothetical metal hydride with $\Delta G_{H-}^\circ = 43$ kcal/mol, $E_{1/2}(\text{M}^{n+}/(n-1)^+) \sim -1.65$ V versus $\text{Fc}^{+/0}$ for the parent complex from our qualitative hydricity model in Figure 2.5. A Brønsted acid with $\text{pK}_a < 29$ is typically required to make a metal hydride with this hydricity (*vide supra*). For a buffer solution at this minimum acid strength, the standard reduction potential for CO_2 reduction is $E^\circ(\text{CO}_2/\text{HCO}_2^-) = -1.64$ V versus $\text{Fc}^{+/0}$. Assuming that the parent complex $[\text{M}]^{n+}$ undergoes a two-electron reduction at $E_{1/2}$, the minimum overpotential for electrocatalysis under these conditions is 10 mV. However, electrocatalytic reactions are

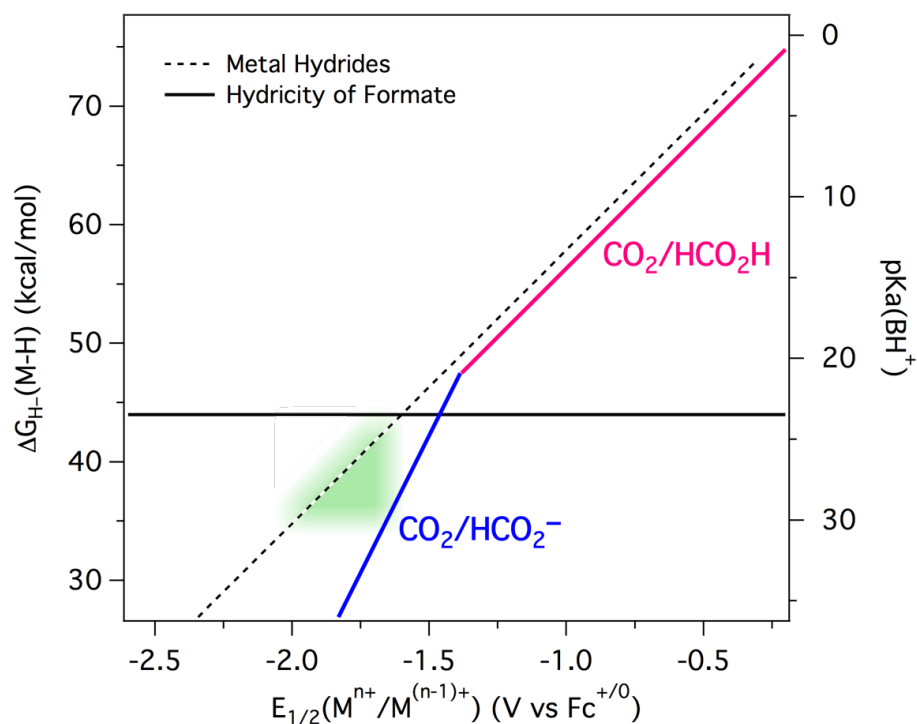


Figure 2.16: Comparison of the standard reduction potential for the CO_2 /formic acid (pink line) and CO_2 /formate (blue line) couples as a function of $\text{pK}_a(\text{BH}^+)$ (right axis), overlaid with the fixed slope correlation of $\Delta G_{H-}^\circ(\text{M-H})$ and $E_{1/2}(\text{M}^{n+}/\text{M}^{(n-1)+})$. Right axis gives the minimum $\text{pK}_a(\text{BH}^+)$ for heterolytic H_2 cleavage for a given $\Delta G_{H-}^\circ(\text{M-H})$ on the left axis. Highlighted green section indicates the approximate region of viability for formate production.

typically performed at least 0.1 V beyond the peak potential; therefore, a practical minimum value for the attainable overpotential for CO_2 reduction to formate with a metal hydride catalyst is roughly 100 mV.

2.2.5 Limitations of the Model.

This formalism represents a useful tool for predicting the hydricity and reactivity of metal hydride systems, but it is not without limitations and should only be considered a qualitative guide. Our dataset was constructed using 51 metal hydrides for which the corresponding parent complexes display reversible $\text{M}^{n+}/\text{M}^{(n-1)+}$ redox couples. For complexes that do not exhibit reversible electrochemistry, the utilization of this model to predict hydricities is unreliable,

although relative hydricity trends may still be correct.⁷⁹ Care must be taken to ensure that the reduction potential of the coordinately unsaturated or acetonitrile-solvento parent complex is utilized to estimate hydricity, and not that of other M-X species such as the halide complex. Furthermore, the existence of a reversible $M^{n+/(n-1)+}$ redox couple for the parent complex does not indicate the accessibility or stability of the corresponding metal hydride, and therefore this guide is best used in conjunction with experimental methods to characterize any new metal hydrides and confirm their predicted reactivity.

Significant deviations from the model in Figure 2.5 are possible even for complexes that do exhibit reversible $M^{n+/(n-1)+}$ redox couples, as exemplified by $[\text{Rh}(\text{depX})_2]^+$ and $[\text{Pt}(\text{EtXanphos})_2]_2^+$ which both contain bidentate phosphine ligands with constrained chelate bite angles that decrease the hydricity of the metal hydrides (*vide supra*).^{55,78} Additionally, the predictive power of this hydricity model is predicated on the assumption that the BDFE of metal hydride bonds remains largely constant regardless of metal identity and ligand framework. However, changes in the oxidation state of metal hydrides have been shown to dramatically change the BDFE.^{26,56,69,101–102} For example, one-electron reduction of $[\text{Co}(\text{CpC}_5\text{F}_4\text{N})(\text{P}_2^{\text{R}}\text{N}_2^{\text{R}'})\text{H}]^+$ ($\text{R} = \text{tBu}$, $\text{R}' = \text{Ph}$) to the Co(II)-hydride results in a significant decrease of over 15 kcal/mol in the metal hydride BDFE.⁶⁹ Similarly, one-electron oxidation of the isolable $[\text{W}(\text{Cp})(\text{CO})_2(\text{IMes})\text{H}]$ to the cationic hydride complex is accompanied by a decrease of approximately 25 kcal/mol in metal hydride BDFE.¹⁰² It is clear from these large BDFE changes that these reduced or oxidized metal hydrides would not fit the hydricity/reduction potential trend well. Other examples exist where changes in the hydride oxidation state do not significantly alter the BDFE: one-electron reduction of $[\text{Ru}(\text{terpy})(\text{bipy})\text{H}]^+$ reduces the metal hydride BDFE by only 1 kcal/mol and thus both $[\text{Ru}(\text{terpy})(\text{bipy})\text{H}]^+$ and $[\text{Ru}(\text{terpy})(\text{bipy})\text{H}]^0$ are consistent with the linear relationship in Figure 2.5.²⁶ In light of such unpredictable variations in BDFE and hydricity with oxidation state, we therefore conclude that the linear model should not be applied to estimate hydricities upon changes in the oxidation state of metal hydrides.

While hydricity is a useful descriptor for the inherent hydride donating ability of a metal-hydride, it does not account for the mechanism of hydride transfer, and depending on the mechanism, hydricity may not be an accurate predictor of metal hydride reactivity. For example, bifunctional hydrogenation catalysts do not operate *via* direct hydride transfer from a metal hydride. Instead, a proximal protic ligand site facilitates outer-sphere dihydrogen transfer to the substrate *via* cooperative (concerted or asynchronous) proton and hydride transfer from the ligand and metal, respectively.^{1,103–106} Also, several examples of Lewis acid assisted catalysis for CO₂ hydrogenation and formic acid dehydrogenation have been reported.^{107–109} In these reactions, a simple comparison of the hydricities of the free substrate and metal hydride catalyst does not accurately reflect the thermodynamics of hydride transfer to/from the Lewis acid-associated substrate. Furthermore, only the thermodynamic hydricity of metal hydrides is considered here: the kinetic hydricity describes the relative rate of hydride transfer to a given hydride acceptor. Kinetic considerations are outside of the scope of our hydricity model, but nonetheless are critical in the design of hydride transfer catalysts. A marriage of predictive thermodynamic and kinetic hydricity trends would be especially instructive for the targeted design of metal hydrides: a step toward this goal was recently reported by Wiedner and co-workers for a series of cobalt and rhodium complexes.⁷⁹

2.3 Conclusion

In this report, we established a dataset of metal hydrides for which measured hydricities and reversible $[M]^{n+/(n-1)+}$ couples are known in acetonitrile or benzonitrile. This dataset includes a wide variety of hydride complexes with diverse metal identity, ligand architecture, geometry, electronic configuration, and overall charge. Despite the large variance in the nature of the metal hydride, a strong correlation between the hydricity and the first reduction potential of the parent metal complex $E_{1/2}(M^{n+/(n-1)+})$ is observed. The linear relationship between hydricity

and $E_{1/2}(M^{n+/(n-1)+})$ is described by a well-established model relating these two parameters to the homolytic bond dissociation free energy (BDFE) of the metal hydride bond. The relatively small variation in BDFE across this entire dataset gives rise to the observed qualitative correlation between hydricity and $E_{1/2}(M^{n+/(n-1)+})$. This model clearly illustrates that large hydride donor ability is not necessarily indicative of a weaker metal hydride bond.

The linear model provides a simple means for roughly estimating hydricity based on $E_{1/2}(M^{n+/(n-1)+})$, thus enabling the thermodynamic driving force of hydride transfer reactions to be predicted based on the relative hydricities of metal and substrate. In the case of CO₂ reduction to formate, consideration of additional reaction parameters, in particular the strength of the Brønsted base or acid reagent, is critical for both in thermal CO₂ hydrogenation in the presence of base or electrocatalytic CO₂ reduction in the presence of a proton source. Using our model, estimates for the thermodynamic requirements of the base and acid can be readily predicted: the graphical representation of these interrelated parameters in Figure 2.16 is especially useful for the overall design of catalytic systems. Analogous thermochemical arguments can also be applied for the reverse reactions of formic acid dehydrogenation and electrocatalytic formate oxidation. Furthermore, as the hydricities of additional small molecules relevant to other catalytic transformations are determined (such as ΔG_{H-}° for methanediol, an intermediate in the six-electron, six-proton reduction of CO₂ to methanol), this qualitative approach will become more broadly applicable for many catalytic reactions beyond CO₂ reduction to formic acid.

Acknowledgements

Chapter 2, in full, is a reprint of the material as it appears in Waldie, K. M.;[‡] Ostericher, A. L.;[‡] Reineke, M.; Sasayama, A. F.; Kubiak, C. P. "Hydricity of Transition-Metal Hydrides: Thermodynamic Considerations for CO₂ Reduction" *ACS Catalysis*, **2018**, 8, 1313-1324. The dissertation author was the primary co-author of this paper. We would like to acknowledge the

early contributions to this work and the helpful discussions of Candace Seu, and the experimental contributions of Alyssia Lilio and Michael Doud. We would like to acknowledge productive discussions with members of the molecular catalysis group at Pacific Northwest National Laboratory. We would also like to acknowledge our reviewers for useful advice about presenting this study. This work was supported by the Air Force Office of Scientific Research through the MURI program under AFOSR Award FA9550-10-1-0572.

2.4 References

1. Casey, C. P.; Guan, H., An efficient and chemoselective iron catalyst for the hydrogenation of ketones. *Journal of the American Chemical Society* **2007**, *129*, 5816-5817.
2. Karvembu, R.; Prabhakaran, R.; Natarajan, K., Shvo's diruthenium complex: a robust catalyst. *Coordination Chemistry Reviews* **2005**, *249*, 911-918.
3. Baratta, W.; Chelucci, G.; Gladiali, S.; Siega, K.; Toniutti, M.; Zanette, M.; Zangrando, E.; Rigo, P., Ruthenium(II) Terdentate CNN Complexes: Superlative Catalysts for the Hydrogen-Transfer Reduction of Ketones by Reversible Insertion of a Carbonyl Group into the Ru-H Bond. *Angewandte Chemie International Edition* **2005**, *44*, 6214-6219.
4. Balaraman, E.; Gunanathan, C.; Zhang, J.; Shimon, L. J. W.; Milstein, D., Efficient hydrogenation of organic carbonates, carbamates and formates indicates alternative routes to methanol based on CO₂ and CO. *Nature Chemistry* **2011**, *3*, 609-614.
5. Wang, D.; Astruc, D., The Golden Age of Transfer Hydrogenation. *Chemical Reviews* **2015**, *115*, 6621-6686.
6. Bullock, R. M., Catalytic ionic hydrogenations. *Chemistry - A European Journal* **2004**, *10*, 2366-2374.
7. Kang, P.; Cheng, C.; Chen, Z.; Schauer, C. K.; Meyer, T. J.; Brookhart, M., Selective Electrocatalytic Reduction of CO₂ to Formate by Water-Stable Iridium Dihydride Pincer Complexes. *Journal of the American Chemical Society* **2012**, *134*, 5500-5503.
8. Brewster, T. P.; Miller, A. J. M.; Heinekey, D. M.; Goldberg, K. I., Hydrogenation of Carboxylic Acids Catalyzed by Half-Sandwich Complexes of Iridium and Rhodium. *Journal of the American Chemical Society* **2013**, *135*, 16022-16025.
9. Díez-González, S.; Nolan, S. P., Transition Metal-Catalyzed Hydrosilylation of Carbonyl Compounds and Imines. A Review. *Organic Preparations and Procedures International* **2007**, *39*, 523-559.
10. Morris, R. H., Asymmetric hydrogenation, transfer hydrogenation and hydrosilylation of ketones catalyzed by iron complexes. *Chemical Society Reviews* **2009**, *38*, 2282-2291.
11. Larionov, E.; Li, H.; Mazet, C., Well-defined transition metal hydrides in catalytic isomerizations. *Chemical Communications* **2014**, *50*, 9816-9826.
12. Pospech, J.; Fleischer, I.; Franke, R.; Buchholz, S.; Beller, M., Alternative metals for homogeneous catalyzed hydroformylation reactions. *Angewandte Chemie International Edition* **2013**, *52*, 2852-2872.

13. Artero, V.; Fontecave, M., Some general principles for designing electrocatalysts with hydrogenase activity. *Coordination Chemistry Reviews* **2005**, *249* (15-16), 1518-1535.
14. McKone, J. R.; Marinescu, S. C.; Brunschwig, B. S.; Winkler, J. R.; Gray, H. B., Earth-abundant hydrogen evolution electrocatalysts. *Chemical Science* **2014**, *5*, 865-878.
15. Bullock, R. M.; Appel, A. M.; Helm, M. L., Production of hydrogen by electrocatalysis: making the H-H bond by combining protons and hydrides. *Chemical Communications* **2014**, *50*, 3125-3143.
16. Onishi, N.; Xu, S.; Manaka, Y.; Suna, Y.; Wang, W.-H.; Muckerman, J. T.; Fujita, E.; Himeda, Y., CO₂ Hydrogenation Catalyzed by Iridium Complexes with a Proton- Responsive Ligand. *Inorganic Chemistry* **2015**, *54*, 5114-5123.
17. Fong, H.; Peters, J. C., Hydricity of an Fe-H Species and Catalytic CO₂ Hydrogenation. *Inorganic Chemistry* **2015**, *54*, 5124-5135.
18. Bertini, F.; Gorgas, N.; Stöger, B.; Peruzzini, M.; Veiros, L. F.; Kirchner, K.; Gonsalvi, L., Efficient and Mild Carbon Dioxide Hydrogenation to Formate Catalyzed by Fe(II) Hydrido Carbonyl Complexes Bearing 2,6-(Diaminopyridyl)diphosphine Pincer Ligands. *ACS Catalysis* **2016**, *6* (5), 2889-2893.
19. Zall, C. M.; Linehan, J. C.; Appel, A. M., Triphosphine-Ligated Copper Hydrides for CO₂ Hydrogenation: Structure, Reactivity, and Thermodynamic Studies. *Journal of the American Chemical Society* **2016**, *138*, 9968-9977.
20. Rawat, K. S.; Mahata, A.; Pathak, B., Catalytic Hydrogenation of CO₂ by Fe-Complexes Containing Pendant Amines: Role of Water and Base. *Journal of Physical Chemistry C* **2016**, *120*, 26652-26662.
21. Burgess, S. A.; Kendall, A. J.; Tyler, D. R.; Linehan, J. C.; Appel, A. M., Hydrogenation of CO₂ in Water Using a Bis(diphosphine) Ni-H Complex. *ACS Catalysis* **2017**, *7*, 3089-3096.
22. Pugh, J. R.; Bruce, M. R. M.; Sullivan, B. P.; Meyer, T. J., Formation of a Metal-Hydride Bond and the Insertion of CO₂. Key steps in the electrocatalytic reduction of carbon dioxide to formate anion. *Inorganic Chemistry* **1991**, *30*, 86-91.
23. Taheri, A.; Berben, L., Making C-H Bonds with CO₂: Production of Formate by Molecular Electrocatalysts. *Chemical Communications* **2016**, *52*, 1768-1777.
24. DuBois, D. L.; Berning, D. E., Hydricity of transition-metal hydrides and its role in CO₂ reduction. *Applied Organometallic Chemistry* **2000**, *14* (12), 860-862.

25. Matsubara, Y.; Fujita, E.; Doherty, M. D.; Muckerman, J. T.; Creutz, C., Thermodynamic and kinetic hydricity of ruthenium(II) hydride complexes. *Journal of the American Chemical Society* **2012**, *134* (38), 15743-57.
26. Wiedner, E. S.; Chambers, M. B.; Pitman, C. L.; Bullock, R. M.; Miller, A. J. M.; Appel, A. M., Thermodynamic Hydricity of Transition Metal Hydrides. *Chemical Reviews* **2016**, *116* (15), 8655-8692.
27. Creutz, C.; Chou, M. H., Hydricities of d(6) metal hydride complexes in water. *Journal of the American Chemical Society* **2009**, *131* (8), 2794-5.
28. Pitman, C. L.; Brereton, K. R.; Miller, A. J., Aqueous Hydricity of Late Metal Catalysts as a Continuum Tuned by Ligands and the Medium. *Journal of the American Chemical Society* **2016**, *138* (7), 2252-60.
29. Chou, M.; Creutz, C.; Mahajan, D.; Sutin, N.; Zipp, A. P., Nature of Bis(2,2'-bipyridine)rhodium(I) in Aqueous Solutions. *Inorganic Chemistry* **1982**, *21*, 3989-3997.
30. Tsay, C.; Livesay, B. N.; Ruelas, S.; Yang, J. Y., Solvation effects on transition metal hydricity. *Journal of the American Chemical Society* **2015**, *137* (44), 14114-21.
31. Connelly Robinson, S. J.; Zall, C. M.; Miller, D. L.; Linehan, J. C.; Appel, A. M., Solvent influence on the thermodynamics for hydride transfer from bis(diphosphine) complexes of nickel. *Dalton Transactions* **2016**, *45*, 10017-10023.
32. Taheri, A.; Thompson, E. J.; Fettinger, J. C.; Berben, L. A., An Iron Electrocatalyst for Selective Reduction of CO₂ to Formate in Water: Including Thermochemical Insights. *ACS Catalysis* **2015**, *5*, 7140-7151.
33. Berning, D. E.; Noll, B. C.; DuBois, D. L., Relative Hydride, Proton, and Hydrogen Atom Transfer Abilities of [HM(diphosphine)₂]PF₆ Complexes (M = Pt, Ni). *Journal of the American Chemical Society* **1999**, *121* (49), 11432-11447.
34. Zhang, X.-M.; Bruno, J. W.; Enyinnaya, E., Hydride Affinities of Arylcarbenium Ions and Iminium Ions in Dimethyl Sulfoxide and Acetonitrile. *Journal of Organic Chemistry* **1998**, *63* (14), 4671-4678.
35. Chen, S.; Rousseau, R.; Raugei, S.; Dupuis, M.; DuBois, D. L.; Bullock, R. M., Comprehensive thermodynamics of nickel hydride bis(diphosphine) complexes: A predictive model through computations. *Organometallics* **2011**, *30*, 6108-6118.
36. Chen, S.; Ho, M.-H.; Bullock, R. M.; Dubois, D. L.; Dupuis, M.; Rousseau, R.; Raugei, S., Computing free energy landscapes: Application to Ni-based electrocatalysts with pendant amines for H₂ production and oxidation. *ACS Catalysis* **2014**, *4*, 229-242.

37. Raugei, S.; Dubois, D. L.; Rousseau, R.; Chen, S.; Ho, M.-H.; Bullock, R. M.; Dupuis, M., Toward molecular catalysts by computer. *Accounts of Chemical Research* **2015**, *48*, 248-255.
38. Solis, B. H.; Hammes-Schiffer, S., Substituent Effects on Cobalt Diglyoxime Catalysts for Hydrogen Evolution. *Journal of the American Chemical Society* **2011**, *133*, 19036-19039.
39. Horvath, S.; Fernandez, L. E.; Appel, A. M.; Hammes-Schiffer, S., pH-dependent reduction potentials and proton-coupled electron transfer mechanisms in hydrogen-producing nickel molecular electrocatalysts. *Inorganic Chemistry* **2013**, *52*, 3643-3652.
40. Raugei, S.; Helm, M. L.; Hammes-Schiffer, S.; Appel, A. M.; O'Hagan, M.; Wiedner, E. S.; Bullock, R. M., Experimental and Computational Mechanistic Studies Guiding the Rational Design of Molecular Electrocatalysts for Production and Oxidation of Hydrogen. *Inorganic Chemistry* **2016**, *55*, 445-460.
41. Huynh, M. T.; Anson, C. W.; Cavell, A. C.; Stahl, S. S.; Hammes-Schiffer, S., Quinone 1 e⁻ and 2 e⁻/2 H⁺ Reduction Potentials: Identification and Analysis of Deviations from Systematic Scaling Relationships. *Journal of the American Chemical Society* **2016**, *138*, 15903-15910.
42. Glezakou, V.-A.; Rousseau, R.; Elbert, S. T.; Franz, J. A., Trends in Homolytic Bond Dissociation Energies of Five- and Six-Coordinate Hydrides of Group 9 Transition Metals: Co, Rh, Ir. *Journal of Physical Chemistry A* **2017**, *121*, 1993-2000.
43. Sandhya, K. S.; Suresh, C. H., Quantification of Thermodynamic Hydridity of Hydride Complexes of Mn, Re, Mo, and W Using the Molecular Electrostatic Potential. *Journal of Physical Chemistry A* **2017**, *121*, 2814-2819.
44. Berning, D. E.; Miedaner, A.; Curtis, C. J.; Noll, B. C.; Rakowski DuBois, M. C.; DuBois, D. L., Free-Energy Relationships between the Proton and Hydride Donor Abilities of [HNi(diphosphine)₂]⁺ Complexes and the Half-Wave Potentials of Their Conjugate Bases. *Organometallics* **2001**, *20* (9), 1832-1839.
45. Galan, B. R.; Schoffel, J.; Linehan, J. C.; Seu, C.; Appel, A. M.; Roberts, J. A.; Helm, M. L.; Kilgore, U. J.; Yang, J. Y.; DuBois, D. L.; Kubiak, C. P., Electrocatalytic oxidation of formate by [Ni(P₂N₂^R)₂(CH₃CN)]²⁺ complexes. *Journal of the American Chemical Society* **2011**, *133* (32), 12767-79.
46. Kilgore, U. J.; Stewart, M. P.; Helm, M. L.; Dougherty, W. G.; Kassel, W. S.; DuBois, M. R.; DuBois, D. L.; Bullock, R. M., Studies of a series of [Ni(P₂N₂^RPh)₂(CH₃CN)]²⁺ complexes as electrocatalysts for H₂ production: substituent variation at the phosphorus atom of the P₂N₂ ligand. *Inorganic Chemistry* **2011**, *50* (21), 10908-18.

47. Raebiger, J. W.; Miedaner, A.; Curtis, C. J.; Miller, S. M.; Anderson, O. P.; DuBois, D. L., Using ligand bite angles to control the hydricity of palladium diphosphine complexes. *Journal of the American Chemical Society* **2004**, *126* (17), 5502-14.
48. Curtis, C. J.; Miedaner, A.; Raebiger, J. W.; DuBois, D. L., Periodic Trends in Metal Hydride Donor Thermodynamics: Measurement and Comparison of the Hydride Donor Abilities of the Series $\text{HM}(\text{PNP})_2^{2+}$ (M = Ni, Pd, Pt; $\text{PNP} = \text{Et}_2\text{PCH}_2\text{N}(\text{Me})\text{CH}_2\text{PEt}_2$). *Organometallics* **2004**, *23* (3), 511-516.
49. Several hydricities in Tables 2.1 – 2.3 differ from those reported in the original literature due to variation in acidity scales and rounding differences. Here, we use the recalculated values reported by Wiedner and co-workers (ref. 27) when applicable.
50. Evans, D. H., One-electron and two-electron transfers in electrochemistry and homogeneous solution reactions. *Chemical Reviews* **2008**, *108*, 2113-2144.
51. Lilio, A. M.; Reineke, M. H.; Moore, C. E.; Rheingold, A. L.; Takase, M. K.; Kubiak, C. P., Incorporation of Pendant Bases into $\text{Rh}(\text{diphosphine})_2$ Complexes: Synthesis, Thermodynamic Studies, And Catalytic CO_2 Hydrogenation Activity of $[\text{Rh}(\text{P}_2\text{N}_2)_2]^+$ Complexes. *Journal of the American Chemical Society* **2015**, *137* (25), 8251-60.
52. Price, A. J.; Ciancanelli, R.; Noll, B. C.; Curtis, C. J.; DuBois, D. L.; DuBois, M. R., $\text{HRh}(\text{dppb})_2$, a Powerful Hydride Donor. *Organometallics* **2002**, *21* (22), 4833-4839.
53. Qi, X.-J.; Fu, Y.; Liu, L.; Guo, Q.-X., Ab Initio Calculations of Thermodynamic Hydricities of Transition-Metal Hydrides in Acetonitrile. *Organometallics* **2007**, *26* (17), 4197-4203.
54. Raebiger, J. W.; DuBois, D. L., Thermodynamic Studies of $\text{HRh}(\text{depx})_2$ and $[\text{H}_2\text{Rh}(\text{depx})_2](\text{CF}_3\text{SO}_3)$: Relationships between Five-Coordinate Monohydrides and Six-Coordinate Dihydrides. *Organometallics* **2005**, *24* (1), 110-118.
55. Ciancanelli, R.; Noll, B. C.; DuBois, D. L.; DuBois, M. R., Comprehensive Thermodynamic Characterization of the Metal–Hydrogen Bond in a Series of Cobalt–Hydride Complexes. *Journal of the American Chemical Society* **2002**, *124* (12), 2984-2992.
56. Curtis, C. J.; Miedaner, A.; Ellis, W. W.; DuBois, D. L., Measurement of the Hydride Donor Abilities of $[\text{HM}(\text{diphosphine})_2]^+$ Complexes (M = Ni, Pt) by Heterolytic Activation of Hydrogen. *Journal of the American Chemical Society* **2002**, *124* (9), 1918-1925.
57. Wiese, S.; Kilgore, U. J.; DuBois, D. L.; Bullock, R. M., $[\text{Ni}(\text{P}_2^{\text{Me}}\text{N}_2^{\text{Ph}})_2](\text{BF}_4)_2$ as an Electrocatalyst for H_2 Production. *ACS Catalysis* **2012**, *2* (5), 720-727.
58. Yang, J. Y.; Bullock, R. M.; Dougherty, W. G.; Kassel, W. S.; Twamley, B.; DuBois, D. L.; Rakowski DuBois, M., Reduction of oxygen catalyzed by nickel diphosphine complexes with positioned pendant amines. *Dalton Transactions* **2010**, *39* (12), 3001-10.

59. Xue, L.; Ahlquist, M. S., A DFT study: why do $[\text{Ni}(\text{P}_2^{\text{R}}\text{N}_2^{\text{R}'})_2]^{2+}$ complexes facilitate the electrocatalytic oxidation of formate? *Inorganic Chemistry* **2014**, *53* (7), 3281-9.
60. Frazee, K.; Wilson, A. D.; Appel, A. M.; Rakowski DuBois, M.; DuBois, D. L., Thermodynamic Properties of the Ni–H Bond in Complexes of the Type $[\text{HNi}(\text{P}_2^{\text{R}}\text{N}_2^{\text{R}'})_2](\text{BF}_4)$ and Evaluation of Factors That Control Catalytic Activity for Hydrogen Oxidation/Production. *Organometallics* **2007**, *26* (16), 3918-3924.
61. Lense, S.; Ho, M.-H.; Chen, S.; Jain, A.; Raugei, S.; Linehan, J. C.; Roberts, J. A. S.; Appel, A. M.; Shaw, W., Incorporating Amino Acid Esters into Catalysts for Hydrogen Oxidation: Steric and Electronic Effects and the Role of Water as a Base. *Organometallics* **2012**, *31*, 6719-6731.
62. Yang, J. Y.; Smith, S. E.; Liu, T.; Dougherty, W. G.; Hoffert, W. A.; Kassel, W. S.; Rakowski DuBois, M.; DuBois, D. L.; Bullock, R. M., Two pathways for electrocatalytic oxidation of hydrogen by a nickel bis(diphosphine) complex with pendant amines in the second coordination sphere. *Journal of the American Chemical Society* **2013**, *135* (26), 9700-12.
63. Yang, J. Y.; Bullock, R. M.; Shaw, W. J.; Twamley, B.; Frazee, K.; Dubois, M. R.; Dubois, D. L., Mechanistic Insights into Catalytic H_2 Oxidation by Ni Complexes Containing a Diphosphine Ligand with a Positioned Amine Base. *Journal of the American Chemical Society* **2009**, *131*, 5935-5945.
64. Garg, K.; Matsubara, Y.; Ertem, M. Z.; Lewandowska-Andralojc, A.; Sato, S.; Szalda, D. J.; Muckerman, J. T.; Fujita, E., Striking Differences in Properties of Geometric Isomers of $[\text{Ir}(\text{tpy})(\text{ppy})\text{H}]^+$: Experimental and Computational Studies of their Hydricities, Interaction with CO_2 , and Photochemistry. *Angewandte Chemie International Edition* **2015**, *54*, 14128-14132.
65. Wiedner, E. S.; Bullock, R. M., Electrochemical Detection of Transient Cobalt Hydride Intermediates of Electrocatalytic Hydrogen Production. *Journal of the American Chemical Society* **2016**, *138*, 8309-8318.
66. Barrett, S. M.; Pitman, C. L.; Walden, A. G.; Miller, A. J. M., Photoswitchable hydride transfer from iridium to 1-methylnicotinamide rationalized by thermochemical cycles. *Journal of the American Chemical Society* **2014**, *136*, 14718-14721.
67. Elgrishi, N.; Kurtz, D. A.; Dempsey, J. L., Reaction Parameters Influencing Cobalt Hydride Formation Kinetics: Implications for Benchmarking H_2 -Evolution Catalysts. *Journal of the American Chemical Society* **2017**, *139*, 239-244.
68. Fang, M.; Wiedner, E. S.; Dougherty, W. G.; Kassel, W. S.; Liu, T.; Dubois, D. L.; Bullock, R. M., Cobalt Complexes Containing Pendant Amines in the Second Coordination Sphere as Electrocatalysts for H_2 Production. *Organometallics* **2014**, *33*, 5820-5833.

69. Simoes, J. A. M.; Beauchamp, J. L., Transition metal-hydrogen and metal-carbon bond strengths: the keys to catalysis. *Chemical Reviews* **1990**, *90* (4), 629-688.
70. Mandich, M. L.; Halle, L. F.; Beauchamp, J. L., Determination of the metal-hydrogen and metal-methyl bond dissociation energies of the second-row, Group 8 transition metal cations. *Journal of the American Chemical Society* **1984**, *106* (16), 4403-4411.
71. Armentrout, P. B.; Halle, L. F.; Beauchamp, J. L., Periodic trends in transition metal-hydrogen, metal-carbon, and metal-oxygen bond dissociation energies. Correlation with reactivity and electronic structure. *Journal of the American Chemical Society* **1981**, *103* (21), 6501-6502.
72. Wayner, D. D. M.; Parker, V. D., Bond energies in solution from electrode potentials and thermochemical cycles. A simplified and general approach. *Accounts of Chemical Research* **1993**, *26* (5), 287-294.
73. Tilset, M.; Parker, V. D., Solution homolytic bond dissociation energies of organotransition-metal hydrides. *Journal of the American Chemical Society* **1989**, *111* (17), 6711-6717.
74. Elkind, J. L.; Armentrout, P. B., Transition-metal hydride bond energies: first and second row. *Inorganic Chemistry* **1986**, *25*, 1078-1080.
75. Tilset, M., In *Electron Transfer in Chemistry*, Balzani, V., Ed. Wiley-VCH: Weinheim, Germany, 2008; pp 677-713.76. Halpern, J., Activation of carbonhydrogen bonds by metal complexes: Mechanistic, kinetic and thermodynamic considerations. *Inorganica Chimica Acta* **1985**, *100*, 41-48.
77. Miedaner, A.; Raebiger, J. W.; Curtis, C. J.; Miller, S. M.; DuBois, D. L., Thermodynamic Studies of $[\text{HPt}(\text{EtXantphos})_2]^+$ and $[\text{H}_2\text{Pt}(\text{EtXantphos})_2]^{2+}$. *Organometallics* **2004**, *23* (11), 2670-2679.
78. Jeletic, M. S.; Hulley, E.; Helm, M. L.; Mock, M. T.; Appel, A. M.; Wiedner, E. S.; Linehan, J. C., Understanding the Relationship Between Kinetics and Thermodynamics in CO_2 Hydrogenation Catalysis Understanding the Relationship Between Kinetics and Thermodynamics in CO_2 Hydrogenation Catalysis. *ACS Catalysis* **2017**, *7*, 6008-6017.
79. Lever, A. B. P., Electrochemical Parametrization of Metal Complex Redox Potentials, Using the Ruthenium(III)/Ruthenium(II) Couple To Generate a Ligand Electrochemical Series. *Inorganic Chemistry* **1990**, *29*, 1271-1285.
80. Kadish, K. M.; Morrison, M. M.; Constant, L. A.; Dickens, L.; Davis, D. G., A Study of Solvent and Substituent Effects on the Redox Potentials and Electron-Transfer Rate Constants of Substituted Iron meso-Tetraphenylporphyrins. *Journal of the American Chemical Society* **1976**, *98*, 8387-8390.

81. Masui, H.; Lever, A. B. P.; Dodsworth, E. S., Substituent Effects and Bonding Characteristics in (o-Benzoquinone Diimine)Bis(Bipyridine)Ruthenium(II) Complexes. *Inorganic Chemistry* **1993**, *32*, 258-267.
82. Vlcek, A. A., Ligand based redox series. *Coordination Chemistry Reviews* **1982**, *43*, 39-62.
83. Maestri, M.; Armaroli, N.; Balzani, V.; Constable, E. C.; Thompson, A. M. W. C., Complexes of the Ruthenium(II)-2,2',6',2''-Terpyridine Family - Effect of Electron-Accepting and Electron-Donating Substituents on the Photophysical and Electrochemical Properties. *Inorganic Chemistry* **1995**, *34*, 2759-2767.
84. Ellis, W. W.; Raebiger, J. W.; Curtis, C. J.; Bruno, J. W.; DuBois, D. L., Hydricities of BzNADH, C₅H₅Mo(PMe₃)(CO)₂H, and C₅Me₅Mo(PMe₃)(CO)₂H in Acetonitrile. *Journal of the American Chemical Society* **2004**, *126*, 2738-2743.
85. Stout, D. M.; Meyers, A. I., Recent advances in the chemistry of dihydropyridines. *Chemical Reviews* **1982**, *82*, 223-243.
86. Pollak, N.; Dölle, C.; Ziegler, M., The power to reduce: pyridine nucleotides – small molecules with a multitude of functions. *Biochemical Journal* **2007**, *402*, 205-218.
87. Belenky, P.; Bogan, K. L.; Brenner, C., NAD⁺ metabolism in health and disease. *Trends in Biochemical Sciences* **2007**, *32*, 12-19.
88. McSkimming, A.; Colbran, S. B., The coordination chemistry of organo-hydride donors: new prospects for efficient multi-electron reduction. *Chemical Society Reviews* **2013**, *42*, 5439-5488.
89. Lee, I. S. H.; Ostovic, D.; Kreevoy, M., Marcus theory of hydride transfer from an anionic reduced deazaflavin to NAD⁺ analogs. *Journal of the American Chemical Society* **1988**, *110*, 3989-3993.
90. Handoo, K. L.; Cheng, J. P.; Parker, V. D., Hydride affinities of organic radicals in solution. A comparison of free radicals and carbenium ions as hydride ion acceptors. *Journal of the American Chemical Society* **1993**, *115* (12), 5067-5072.
91. Klippenstein, J.; Arya, P.; Wayner, D. D. M., Relative bond dissociation energies for some NADH model compounds from hydride transfer/electron transfer equilibria in acetonitrile. *Journal of Organic Chemistry* **1991**, *56* (24), 6736-6737.
92. Osadchuk, I.; Tamm, T.; Ahlquist, M. S. G., Theoretical Investigation of a Parallel Catalytic Cycle in CO₂ Hydrogenation by (PNP)IrH₃. *Organometallics* **2015**, *34*, 4932-4940.

93. Benson, E. E.; Kubiak, C. P.; Sathrum, A. J.; Smieja, J. M., Electrocatalytic and homogeneous approaches to conversion of CO₂ to liquid fuels. *Chemical Society Reviews* **2009**, *38* (1), 89-99.
94. Pegis, M. L.; Roberts, J. A. S.; Wasylenko, D. J.; Mader, E. A.; Appel, A. M.; Mayer, J. M., Standard Reduction Potentials for Oxygen and Carbon Dioxide Couples in Acetonitrile and N,N-Dimethylformamide. *Inorganic Chemistry* **2015**, *54*, 11883-11888.
95. Lindley, B. M.; Appel, A. M.; Krogh-Jespersen, K.; Mayer, J. M.; Miller, A. J. M., Evaluating the Thermodynamics of Electrocatalytic N₂ Reduction in Acetonitrile. *ACS Energy Letters* **2016**, *1*, 698-704.
96. Appel, A. M.; Helm, M. L., Determining the Overpotential for a Molecular Electrocatalyst. *ACS Catalysis* **2014**, *4*, 630-633.
97. Stirling, M. J.; Sweeney, G.; MacRory, K.; Blacker, A. J.; Page, M. J., The Kinetics and Mechanism of the Organo-Iridium-Catalysed Enantioselective Reduction of Imines. *Organic & Biomolecular Chemistry* **2016**, *14*, 3614-3622.
98. Bratsch, S. G., Standard Electrode Potentials and Temperature Coefficients in Water at 298.15 K. *Journal of Physical and Chemical Reference Data* **1989**, *18*, 1-21.
99. Kelly, C. A.; Rosseinsky, D. R., Estimates of hydride ion stability in condensed systems: energy of formation and solvation in aqueous and polar-organic solvents. *Physical Chemistry Chemical Physics* **2001**, *3*, 2086-2090.
100. Wiedner, E. S.; Appel, A. M.; DuBois, D. L.; Bullock, R. M., Thermochemical and mechanistic studies of electrocatalytic hydrogen production by cobalt complexes containing pendant amines. *Inorganic Chemistry* **2013**, *52*, 14391-14403.
101. Roberts, J. a. S.; Appel, A. M.; DuBois, D. L.; Bullock, R. M., Comprehensive thermochemistry of W-H bonding in the metal hydrides CpW(CO)₂(IMes)H, [CpW(CO)₂(IMes)H]^{•+}, and [CpW(CO)₂(IMes)(H)₂]⁺. Influence of an N-heterocyclic carbene ligand on metal hydride bond energies. *Journal of the American Chemical Society* **2011**, *133*, 14604-14613.
102. Shvo, Y.; Czarkie, D.; Rahamim, Y.; Chodosh, D. F., A new group of ruthenium complexes: structure and catalysis. *Journal of the American Chemical Society* **1986**, *108*, 7400-7402.
103. Noyori, R.; Yamakawa, M.; Hashiguchi, S., Metal-ligand bifunctional catalysis: a nonclassical mechanism for asymmetric hydrogen transfer between alcohols and carbonyl compounds. *Journal of Organic Chemistry* **2001**, *66*, 7931-7944.
104. Badiei, Y. M.; Wang, W.-H.; Hull, J. F.; Szalda, D. J.; Muckerman, J. T.; Himeda, Y.; Fujita, E., Cp*Co(III) Catalysts with Proton-Responsive Ligands for Carbon Dioxide Hydrogenation in Aqueous Media. *Inorg. Chem.* **2013**, *52*, 12576-12586.

105. Ramakrishnan, S.; Waldie, K. M.; Warnke, I.; De Crisci, A. G.; Batista, V. S.; Waymouth, R. M.; Chidsey, C. E. D., Experimental and Theoretical Study of CO₂ Insertion into Ruthenium Hydride Complexes. *Inorganic Chemistry* **2016**, *55*, 1623-1632.
106. Bernskoetter, W. H.; Hazari, N., Reversible Hydrogenation of Carbon Dioxide to Formic Acid and Methanol: Lewis Acid Enhancement of Base Metal Catalysts. *Accounts of Chemical Research* **2017**, *50*, 1049-1058.
107. Jiang, Y.; Blacque, O.; Fox, T.; Berke, H., Catalytic CO₂ Activation Assisted by Rhenium Hydride/B(C₆F₅)₃ Frustrated Lewis Pairs - Metal Hydrides Functioning as FLP Bases. *Journal of the American Chemical Society* **2013**, *135*, 7751-7760.
108. Bielinski, E. A.; Lagaditis, P. O.; Zhang, Y.; Mercado, B. Q.; Würtele, C.; Bernskoetter, W. H.; Hazari, N.; Schneider, S., Lewis acid-assisted formic acid dehydrogenation using a pincer-supported iron catalyst. *Journal of the American Chemical Society* **2014**, *136*, 10234-10237.

2.5 Appendix A

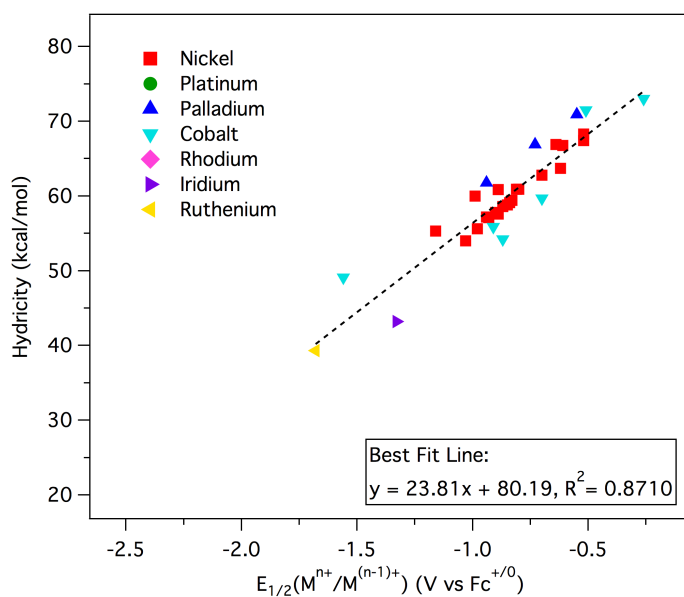


Figure 2.17: Correlation of ΔG_{H-}° with the first one-electron reduction potential of the parent metal complex. Only complexes that exhibit a one-electron $E_{1/2}(M^{n+}/M^{(n-1)+})$ redox couple are included.

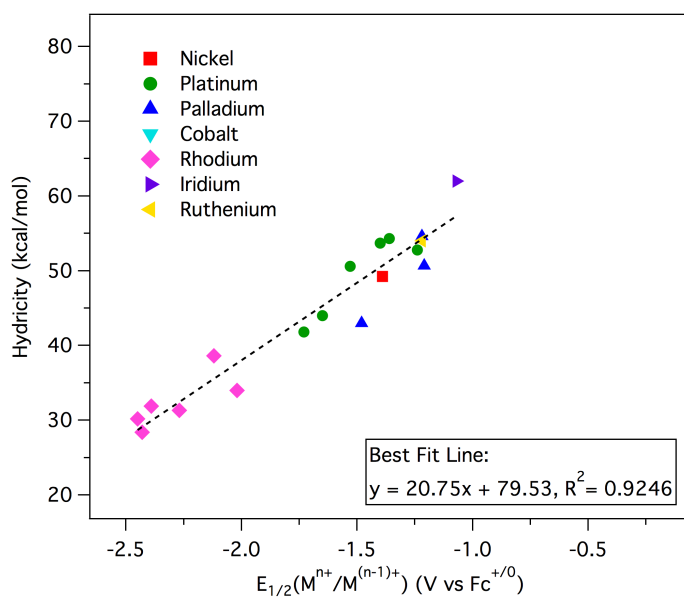

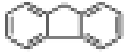
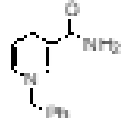
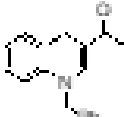






Figure 2.18: Correlation of ΔG_{H-}° with the first two-electron reduction potential of the parent metal complex. Only complexes that exhibit a two-electron $E_{1/2}(M^{n+}/M^{(n-2)+})$ redox couple are included.

Table 2.5: Organic hydride donor dataset.

Hydride Donor	$E_{1/2}(M^+/M^0)$ (V vs. $Fe^{+/0}$)	ΔG_{red}^\ddagger (kcal/mol)	Ref
	-0.3	95	1
p-OMe-C ₆ H ₄ CH ₂ CN	0.195	105.6	2
Ph ₃ CH	-0.05	106	1
p-CN-C ₆ H ₄ CH ₂ Ph	0.210	107.0	2
	0.36	114	1
PhCH ₂ CN	0.785	120.5	2
p-CN-C ₆ H ₄ CH ₂ CN	1.125	129.2	2
(p-Me ₂ NC ₆ H ₄) ₂ CH	-1.178	74.2	2
p-Me ₂ NC ₆ H ₄ CHPh ₂	-0.801	82.9	2
(p-CH ₂ OC ₆ H ₄) ₂ CH	-0.659	86.1	2
(p-CH ₂ OC ₆ H ₄) ₂ CHPh	-0.522	89.3	2
(p-CH ₂ C ₆ H ₄) ₂ CH	-0.344	93.4	2
p-CH ₂ OC ₆ H ₄ CHPh ₂	-0.360	93.9	2
p-CH ₂ SC ₆ H ₄ CHPh ₂	-0.296	95.4	2
p-CH ₂ C ₆ H ₄ CHPh ₂	-0.227	96.1	2
m-CH ₂ O-C ₆ H ₄ CHPh ₂	-0.163	97.6	2
p-C ₆ H ₅ -C ₆ H ₄ CHPh ₂	-0.176	97.9	2
p-F-C ₆ H ₄ CHPh ₂	-0.147	98.0	2
Ph ₂ CH	-0.141	99.1	2
	-1.53	72	1,3
	-1.39	73	1,3
	-1.22	76	1,3
	-0.81	83	1,3
	-0.93	83	1,3
	-0.89	85	1,3

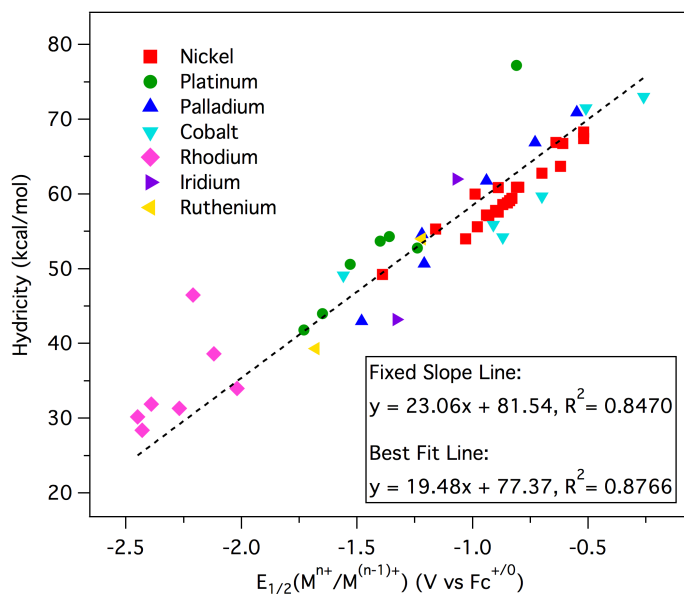


Figure 2.19: Correlation of ΔG_{H-}° with the first one-electron reduction potential of the parent metal complex, including $[\text{Rh}(\text{depx})_2]^+$ and $[\text{Pt}(\text{EtXanphos})_2]^{2+}$. Fixed slope line given by black dashed trace.

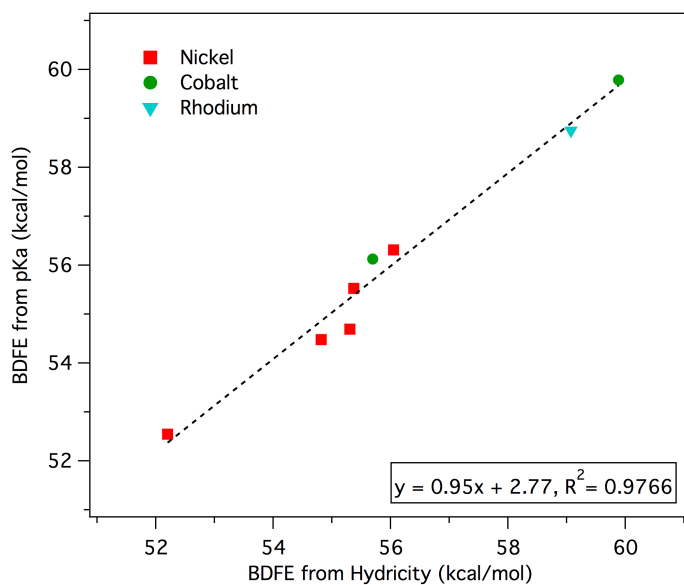


Figure 2.20: Agreement between BDFE calculated from pK_a and hydricity values. Only systems for which the parent metal complex exhibit a one-electron $E_{1/2}(M^{n+}/(n-1)^+)$ redox couple are included.

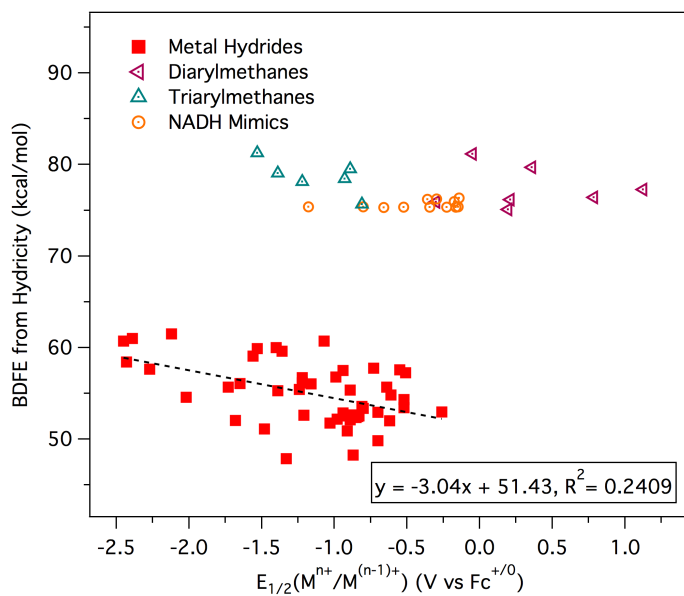


Figure 2.21: BDFE calculated from known hydrivity values as function of experimental reduction potential.

Appendix A References

1. Handoo, K. L.; Cheng, J. P.; Parker, V. D. *J. Am. Chem. Soc.* **1993**, *115*, 5067-5072.
2. Zhang, X.-M.; Bruno, J. W.; Enyinnaya, E. *J. Org. Chem.* **1998**, *63*, 4671-4678.
3. Klippenstein, J.; Arya, P.; Wayner, D. D. M. *J. Org. Chem.* **1991**, *56*, 6736-6737.

Chapter 3

Utilization of Thermodynamic Scaling Relationships in Hydricity to Develop Nickel Hydrogen Evolution Reaction Electrocatalysts with Weak Acids and Low Overpotentials

3.1 Introduction

The implementation of renewable energy technologies such as wind and solar has seen significant growth in recent years.¹ However, due to the intermittent nature of these resources, the viability of sustainable energy economies on a global scale hinges on the development of efficient methods for energy storage and conversion.^{2–4} The electrochemical generation of chemical fuels such as H₂ from wind and solar power is a promising solution to this challenge. While platinum is known to be an active and efficient catalyst for the hydrogen evolution reaction (HER), its cost

and low abundance render it impractical for large-scale use. Therefore, the development of highly active, efficient, and earth-abundant first-row transition metal catalysts for HER is integral to the future of such technologies.

Molecular catalysts offer the advantage over heterogeneous systems in their ease of tuning thermodynamic and kinetic parameters through ligand design and modification and amenability to detailed mechanistic studies. A variety of molecular systems based on nickel, iron, and cobalt have been developed, which exhibit excellent activity.⁵⁻⁷ However, most of these systems are only studied with strong acid substrates and, with few exceptions,⁸ are still stymied by high overpotentials, resulting in low energy efficiencies.

While kinetic design in the form of proton relays is ubiquitous in state of the art molecular HER catalysts, thermodynamic approaches to leveling energy-surfaces to improve energetic efficiencies are under-utilized. The key mechanistic step in these systems often involves protonation of a metal-hydride intermediate by a Brønsted acid source. The thermodynamic favorability of hydrogen evolution by this mechanism can be described according to Figure 3.1 in terms of the hydricity of the metal-hydride intermediate ($\Delta G_{H^-}^\circ$), the pK_a of the added acid (BH), and the hydricity of dihydrogen ($\Delta G_{H_2}^\circ = 76.0 \text{ kcal mol}^{-1}$ in acetonitrile).⁹ Therefore, given the hydricity of a metal-hydride intermediate, proton sources of sufficient but not excessive acidity can be rationally selected such that eq. 5 becomes negative (HER is exergonic) while minimizing overpotentials.

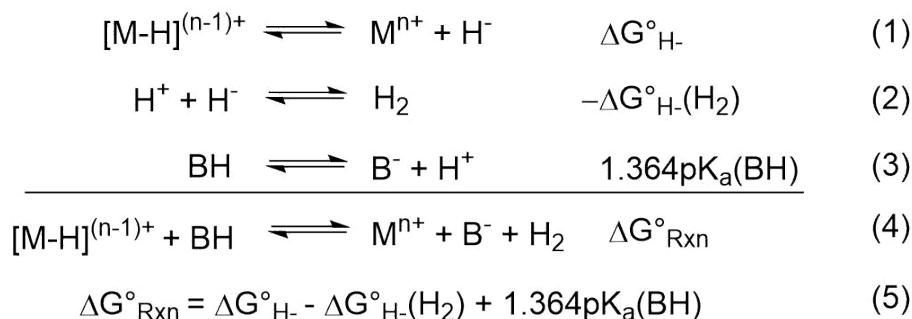


Figure 3.1: Hydrogen evolution in terms of metal-hydride hydricity.

Our lab has recently reported on thermodynamic scaling relationships that relate the hydricity of transition-metal hydrides to the first reduction potential of the parent d^8 metal complex ($E_{1/2}(M^{n+/(n-1)+})$).¹⁰ These relationships allow for the targeting, tuning, and prediction of metal-hydride hydricities and can subsequently be used in the consideration of the pK_a 's of added acids to match proton sources to hydricities of hydride intermediates in order to favor hydrogen evolution with low overpotentials.

Herein we report the synthesis and characterization of new, heteroleptic nickel(II) complexes bearing chelating bis-N-heterocyclic carbene (bis-NHC) ligands in conjunction with bidentate phosphine ligands. The strong donating ability of the bidentate carbene ligand dramatically shifts the metal-based reduction potentials more than 0.4 V negative compared to analogous nickel(II) bis-diphosphine complexes. The hydricities of the corresponding Ni(II)-hydride complexes are estimated from the Ni(II/0) reduction potential, as well as from the Brønsted acid strength at which H_2 evolution is thermodynamically favorable. These systems represent the strongest known nickel-based hydride donors, and thermochemical cycles are used to select mild operating conditions to favor efficient electrocatalytic H_2 evolution (HER).

3.2 Results & Discussion

3.2.1 Synthesis and Characterization

The synthesis of the bis-NHC ligand precursor and the nickel dibromide complex $[Ni(\text{bis-NHC})Br_2]$ were recently described.¹¹ By this procedure, treatment of the ligand precursor with nickel(II) acetate in molten tetrabutylammonium bromide affords the dibromide complex. Subsequent halide abstraction with sodium hexafluorophosphate in the presence of 1,2-bis(diphenylphosphino)ethane (dppe) or 1,2-bis(dimethylphosphino)ethane (dmpe) yields complexes **1** and **2**, respectively, as pale-yellow powders (Figure 3.2).

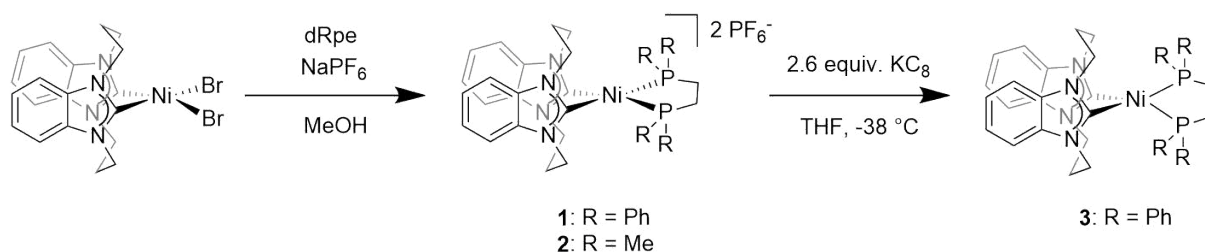


Figure 3.2: Synthesis of **1**, **2**, and **3**.

Single crystals of **1** and **2** suitable for X-Ray crystallographic studies were obtained by vapor diffusion of diethyl ether into solutions of chloroform (for **1**) or acetonitrile (for **2**). Both complexes exhibit distorted square planar geometries at nickel where the bis-NHC and phosphine ligands are coordinated in a bidentate fashion wherein the benzimidazole rings of the tethered bis-NHC ligand lie orthogonal to the nickel plane (Figure 3.3). The C1-Ni-C2 angles are 79.8° and 81.6° for **1** and **2**, respectively, which is significantly smaller than the ideal square planar bite angle of 90°. The unusual architecture and rigidity of the tethered bis-NHC ligand enforces these pinched bite angles and results in a strained coordination environment.

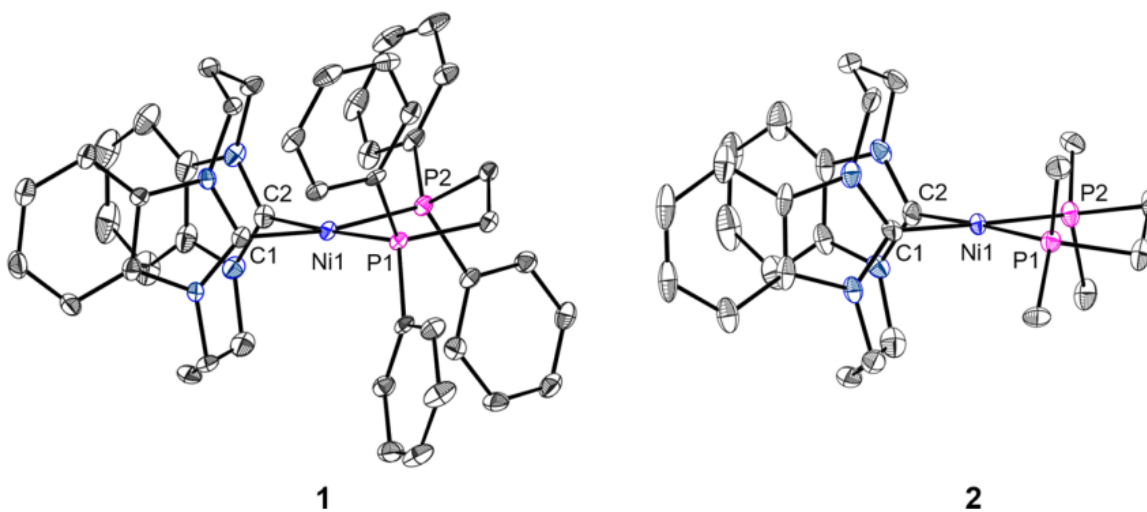


Figure 3.3: Crystal structures of **1** and **2**. Thermal ellipsoids are drawn at the 50% probability level. Hydrogen atoms and PF₆ counterions are omitted for clarity.

Treatment of **1** with KC_8 (2.6 equivalents) in tetrahydrofuran affords the doubly-reduced, charge-neutral species **3**. Single crystals suitable for X-ray crystallographic studies were obtained by vapor diffusion of pentane into a saturated solution of **3** in tetrahydrofuran. The distorted tetrahedral geometry about the metal is consistent with a two-electron, metal-based reduction to yield the formally $\text{Ni}(0)$ complex (Figure 3.4). The pinched C1-Ni-C2 bite angle arising from the rigidity of the bis-NHC ligand observed in **1** and **2** widens only marginally to 81.8° in the tetrahedral arrangement. Therefore, the coordination environment, distorted from an ideal 109.5° tetrahedral bond angle, exhibits comparatively more strain at the bis-NHC chelate. Analogous attempts to isolate the reduced state of **2** were unsuccessful. However, based on the similarity in geometry and electrochemical behavior (*vide infra*) of both **1** and **2**, the doubly-reduced state of **2** likely adopts a similar tetrahedral coordination environment about the formally $\text{Ni}(0)$ metal center.

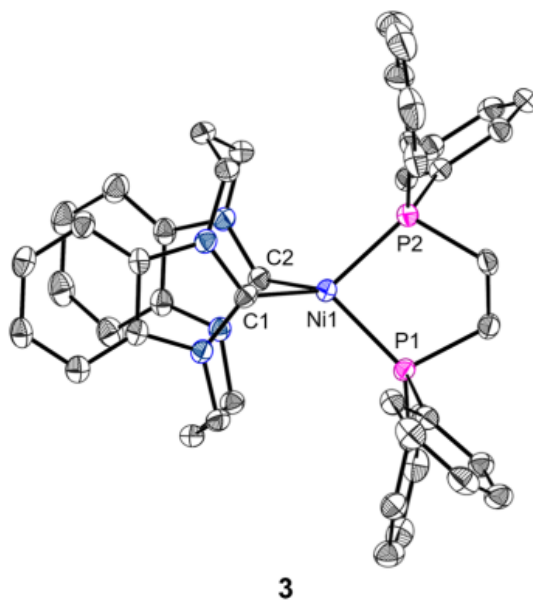


Figure 3.4: Crystal structure of **3**. Thermal ellipsoids are drawn at the 50% probability level. Hydrogen atoms are omitted for clarity.

3.2.2 Electrochemistry

Cyclic voltammetry studies of **1** and **2** were performed in acetonitrile with tetra-n-butylammonium hexafluorophosphate as supporting electrolyte. Complexes **1** and **2** both display a single reversible reduction at -1.53 V and -1.87 V versus the ferrocenium/ferrocene couple ($\text{Fc}^{+/0}$), respectively. The peak-to-peak separations for both reduction features are 49 mV at 0.1 V s^{-1} scan rate, compared to 63 mV for ferrocene under the same conditions. These data support assignment of these redox couples as two-electron processes, most likely where two electrons are added in a sequential fashion with the second reduction being more favorable than the first. The two-electron reduction occurs at a potential more than 300 mV more negative for the dmpe complex **2**, which is attributed to donor effects from the bidentate phosphine ligand: the methyl groups in dmpe make this ligand more electron-donating than dppe and thus shift the reduction potential to more negative values.

Table 3.1: Cyclic voltammetry data and predicted hydricities for **1** and **2**.

	$E_{1/2}$ (V vs. $\text{Fc}^{+/0}$)	ΔE_p (mV)	Predicted ΔG_{H-}° (kcal mol^{-1}) ^a
1	-1.53	49	45.6
2	-1.87	49	37.8

a. Predicted ΔG_{H-}° calculated from $E_{1/2}(M^{n+/(n-1)+})$ based on the fixed-slope line in Figure 3.6.

Neither the bis-NHC nor diphosphine ligands in **1** and **2** are expected to be reduced at these potentials, so the two-electron redox couples are assigned as metal-based Ni(II/0) processes. The observation of a two-electron reduction feature with a first-row transition metal complexes is rare, even more so in the absence of redox-active ligands capable of accepting electron density as needed. Such multi-electron behavior is typically reserved for noble metal complexes. This trend

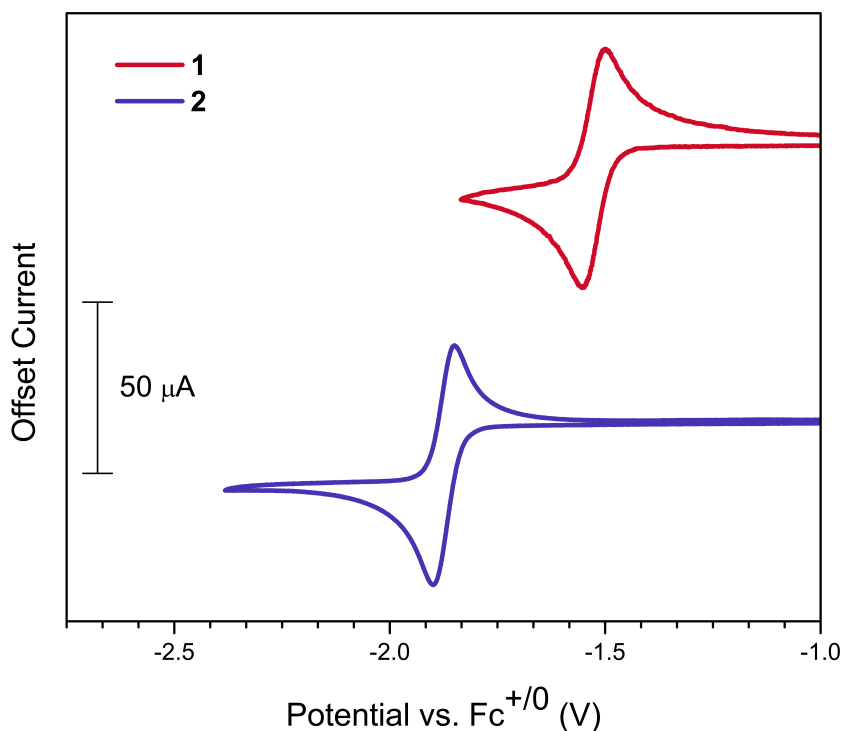


Figure 3.5: Cyclic voltammograms of **1** (red) and **2** (blue) in acetonitrile (1 mM nickel in 0.1 M Bu₄NPF₆). Scan rate 100 mV/s.

is well exemplified by the [M(diphosphine)₂]ⁿ⁺ family of complexes: for M = Ni, two separate one-electron redox processes assigned as the Ni(II/I) and Ni(I/0) couples are observed,^{9,12–19} but for M = Pt, Pd, or Rh a single, reversible two-electron M(II/0) reduction is typically seen.^{9,12,20–23}

Interestingly, a similar two-electron Ni(II/0) couple has been observed for the closely related complex [Ni(dmpe)₂]²⁺, containing two strongly donating dmpe ligands. This complex exhibits the most negative reduction potential ($E_{1/2} = -1.39$ V vs. Fc^{+/0}) of the bis-diphosphine analogues of nickel.¹² The reduction potentials for **1** and **2** are 0.14 and 0.48 V more negative than for [Ni(dmpe)₂]²⁺, indicating an even larger increase in electron density at the metal through the use of highly σ -donating NHC ligands. This approach of introducing very electron rich ligands may be a general strategy for obtaining two-electron reactivity at first row transition

metal complexes. Here, it likely reflects the destabilization of Ni(I) relative to Ni(II) with strong σ -donor ligands.

3.2.3 Estimation of Hydricity

Our lab has recently reported on a scaling relationship between hydricity and the first reduction potential of the parent metal complex, $E_{1/2}(M^{n+/(n-1)+})$, which holds across a wide variety of d^8 transition-metal hydride complexes.¹⁰ Using the thermochemical cycle shown in Figure 3.2, hydricity can be expressed in terms of the free energy of reduction to form a hydride from hydrogen ($\Delta G_{H./-}^\circ$, 26.0 kcal mol⁻¹ in acetonitrile),¹² the bond dissociation free energy (BDFE) of the metal-hydride bond, and the first reduction potential of the parent complex $E_{1/2}(M^{n+/(n-1)+})$ (Equation 9). Since the variation in BDFE of most transition metal hydrides is comparatively small, this relationship provides a qualitative handle for prediction of ΔG_{H-}° for a metal-hydride species based solely on the reduction potential of the parent metal complex.

Using the fixed slope (nF) line (eq. 9) and the reduction potentials of **1** (-1.53 V) and **2** (-1.87 V), the hydricities of the corresponding hydrides, **1H**, and **2H**, are predicted to be 45.6 kcal mol⁻¹ and 37.8 kcal mol⁻¹, respectively. Attempts to chemically isolate and experimentally measure the hydricities were unsuccessful due to instability of the hydride species; however, judicious selection of an added weak acid will either allow electrochemical generation and observation of a Ni(II) hydride or electrocatalytic hydrogen evolution. This effect can readily be seen through the relationship in eq. 5 (Figure 3.1). Here, the change in Gibbs free energy for HER is in terms of the hydricity of dihydrogen ($\Delta G_{H-}^\circ(H_2) = 76.0$ kcal mol⁻¹ in acetonitrile),⁹ the hydricity of the metal hydride (ΔG_{H-}°), and the pK_a of the added acid (BH). This relationship provides a means to experimentally benchmark hydricities of electrochemically-generated hydrides based upon the selection of acids such that eq. 5 becomes negative and HER is an exergonic process.

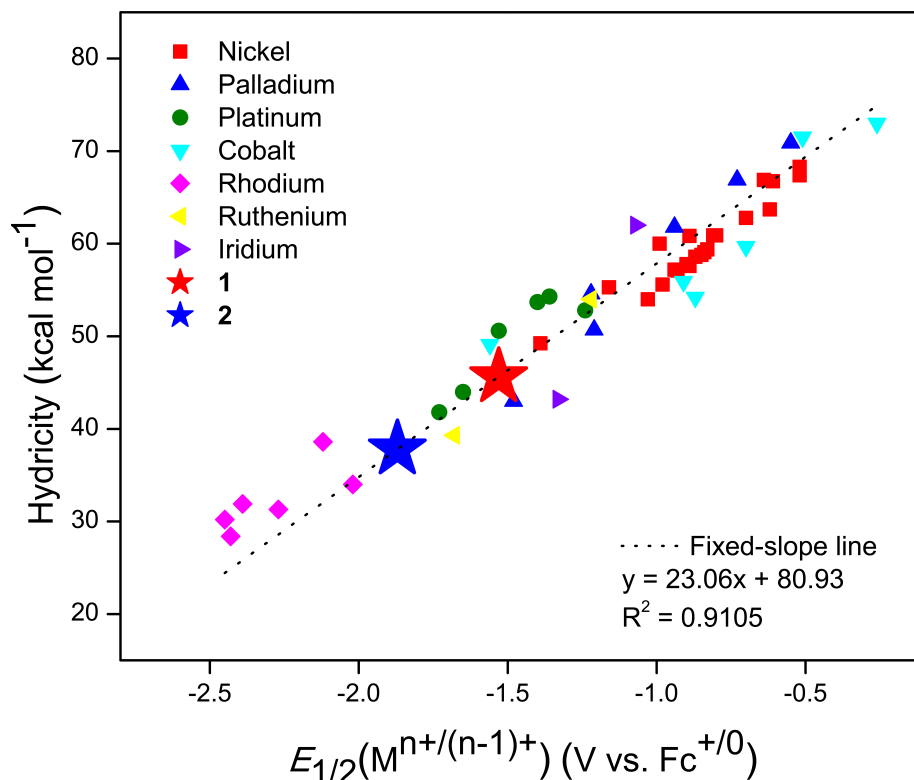


Figure 3.6: Hydricities of transition metal hydrides as a function of $E_{1/2}(M^{n+/(n-1)+})$ in acetonitrile. $E_{1/2}(Ni^{II/0})$ and corresponding predicted ΔG_{H-}° for **1** and **2** indicated by the red and blue stars, respectively. Adapted from Ref. 10.

Experimental support for the above relationship can be found in the electrochemical response of **2** when two different weak acids are used. When cyclic voltammograms of **2** are recorded in the presence of methanol ($pK_a = 29.0$ in DMSO, pK_a in acetonitrile unknown)²⁴ a loss of reversibility of the Ni(II/0) couple is observed with the growth of a new oxidative feature at -1.15 V vs. $Fc^{+/0}$ (Figure 3.8). The loss of reversibility in the Ni(II/0) couple is best explained as protonation of the Ni(0) species by methanol. Methanol is then too weak of an acid to further protonate the hydride to form H_2 and the re-oxidation of the hydride is observed at -1.15 V vs. $Fc^{+/0}$. When a more stronger acid, such as phenol ($pK_a = 29.14$ in acetonitrile),²⁵ is used, a sudden current increase is observed at the Ni(II/0) couple (Figure 3.9). This behavior now indicates electrocatalytic hydrogen evolution and eq. 9 must be negative under these conditions.

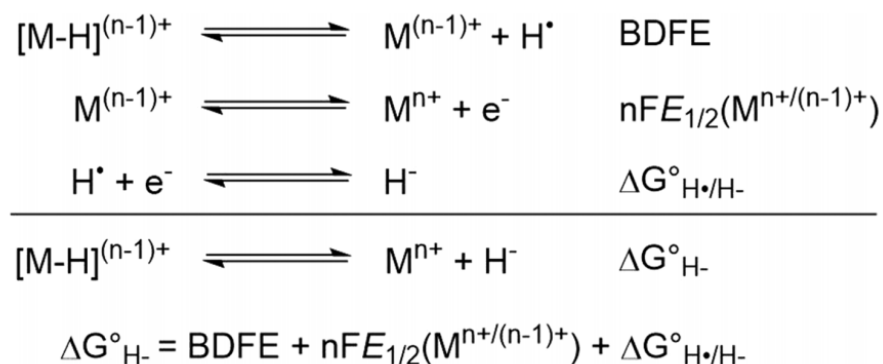


Figure 3.7: Hydricity in terms of $E_{1/2}(M^{n+/(n-1)+})$.

This allows assignment of an upper bound for the hydricity of **1H** at $\Delta G^{\circ}_{H^{-}} = 36.4 \text{ kcal mol}^{-1}$, if the pK_a of phenol is taken as 29.1.

It is important to note however, that phenol is known to exhibit significant homoconjugation in acetonitrile, which will significantly lower the pK_a . To avoid artificial depression of the calculated hydricity, the homoconjugation of phenol must be considered. At concentrations of 0.1 M, the pK_a of phenol in acetonitrile can be estimated at 25.9 (see Appendix B), which gives a benchmarked hydricity of $\Delta G^{\circ}_{H^{-}} < 40.6 \text{ kcal mol}^{-1}$.²⁶ This avoids artificial depression of the calculated hydricity, and is in excellent agreement with the hydricity of $37.8 \text{ kcal mol}^{-1}$, predicted by the scaling relationship between $\Delta G^{\circ}_{H^{-}}$ and $E_{1/2}(\text{Ni}^{II/I})$. (Fig. 3.6, eq. 9).

Applying the same treatment to **1**, the corresponding hydride is predicted to be insufficiently hydridic to favor HER with phenol under these conditions. This is confirmed upon the addition of phenol where only electrochemical generation and oxidation of the hydride species is observed (Figure 3.28). HER with complex **1**, however, becomes favorable when more protic acids such as triethylammonium tetrafluoroborate (HNEt_3BF_4 , $pK_a = 18.82$ in acetonitrile)²⁷ are used. The addition of HNEt_3BF_4 results in modest current increase at the Ni(II/0) couple and loss of the Ni(II)-H oxidative feature, behavior indicative of HER catalyzed by **1** (Figure 3.29). The hydricity of the electrochemically-generated hydride corresponding to **1** is therefore calculated to have an upper bound of $50.3 \text{ kcal mol}^{-1}$ which is in excellent agreement with the hydricity

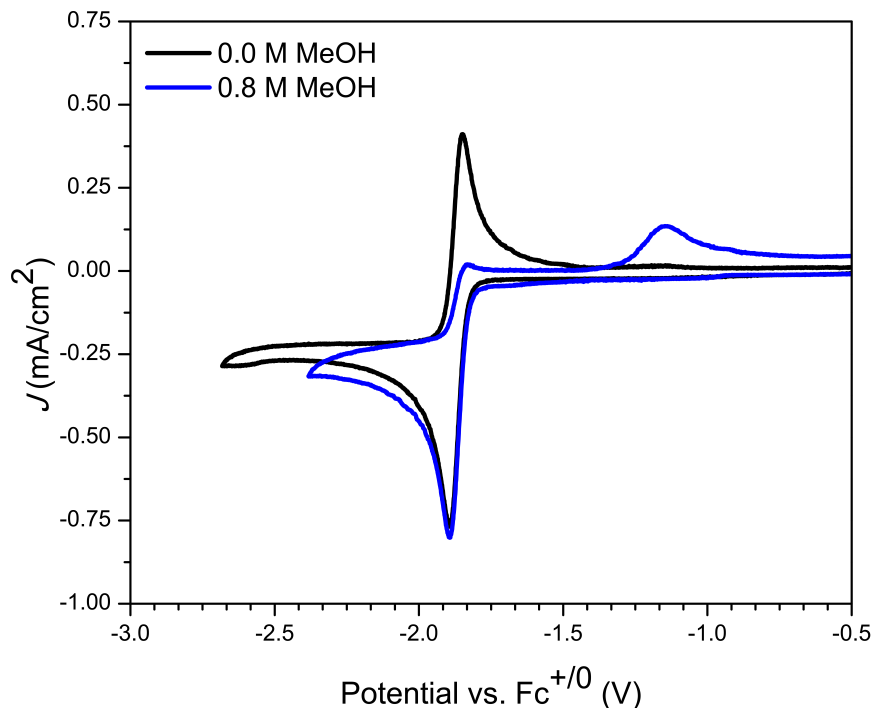


Figure 3.8: Cyclic voltammetry of **2** in the absence and presence of 0.8 M methanol in acetonitrile (1 mM **2** in 0.1 M Bu₄PF₆). Scan rate 100 mV/s.

of 45.6 kcal mol⁻¹ predicted by E_{1/2}(NiIII/I). These results demonstrate how, through judicious selection of acids, benchmarks for hydricities can readily be assigned. Furthermore, these results support that consideration of the acid pK_a can readily switch electrocatalytic hydrogen evolution on or off.

3.2.4 Electrocatalytic Hydrogen Evolution

The further addition of phenol to a solution of **2** in acetonitrile gives rise to a significant increase in current by cyclic voltammetry at the potential of the two-electron Ni(II/0) couple, as shown in Figure 3.9. The origin of this current enhancement was verified by controlled potential electrolysis: quantitative Faradaic efficiency for H₂ was observed at -1.9 V versus Fc^{+ / 0} using 1 mM **2** with 0.2 M phenol (Figures 3.26-27). The direct reduction of phenol at glassy carbon is not observed by cyclic voltammetry at these potentials (Figure 3.25), and controlled potential

electrolysis in the absence of nickel catalyst showed negligible H₂ production. Additionally, catalysis by the freely-diffusing, homogeneous species was further corroborated by lack of current enhancement in a rinse test, in which the same glassy carbon working electrode from an electrocatalytic CV experiment was scanned in a fresh solution in the absence of catalyst (Figure 3.24).

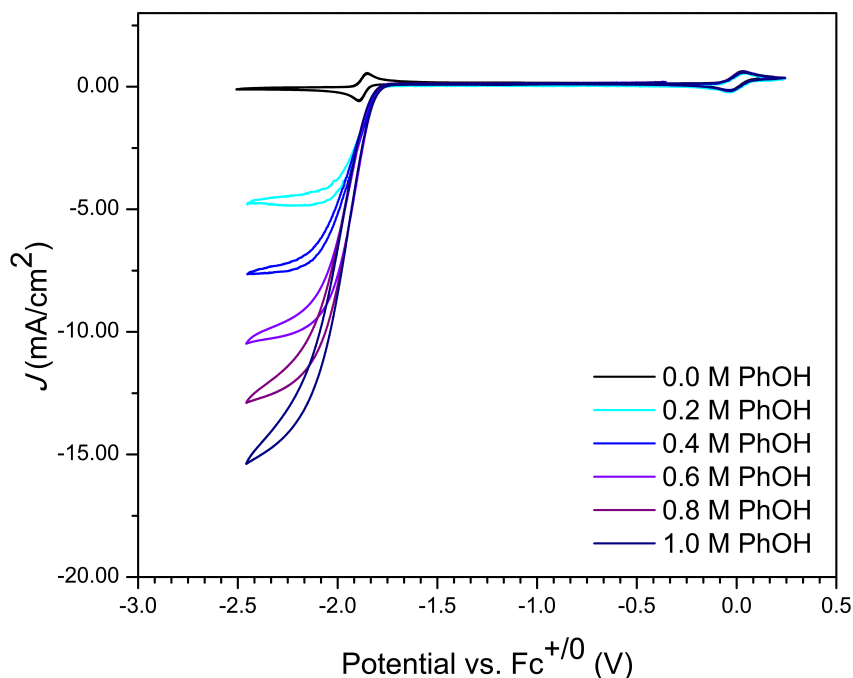


Figure 3.9: Cyclic voltammograms of **2** with increasing phenol concentration in acetonitrile (1 mM **2** in 0.1 M Bu₄NPF₆). Scan rate 100 mV/s.

The S-shaped plateau current responses in Figure 3.9 are indicative of pseudo first-order kinetic conditions and thus allow for estimation of the catalytic turnover frequency (TOF) from the catalytic current enhancement i_{cat}/i_p . The plateau catalytic current (i_{cat}) and the peak current without substrate (i_p) are given by eqs. 10 and 11, respectively, from which eq. 12 is obtained. This equation gives the TOF in terms of the scan rate in V s⁻¹ (v), number of electrons in the reversible, non-catalytic redox process (n_p), Faraday's constant (F), universal gas constant (R), temperature (T), and the number of electrons in the catalytic reaction (n_{cat}).²⁸ From Figure 3.9, E_{cat} is taken as the start of the catalytic current plateau ($E_{cat} = -2.22$ V versus Fc^{+/0}), which

gives $i_{cat}/i_p = 25.1$ in the presence of 1.0 M phenol and an estimated TOF of 977 s^{-1} . However, this calculated TOF is likely an underestimate, as substrate saturation is not yet achieved at these concentrations of phenol.

$$i_{cat} = n_{cat}FA[cat](Dk_{cat}[Q]^y)^{1/2} \quad (10)$$

$$i_p = 0.4463n_p^{3/2}FA[cat]\left(\frac{F}{RT}\right)^{1/2}v^{1/2}D^{1/2} \quad (11)$$

$$TOF = k_{cat}[Q] = \frac{Fvn_p^3}{RT}\left(\frac{0.4463}{n_{cat}}\right)^2\left(\frac{i_{cat}}{i_p}\right)^2 \quad (12)$$

The overpotential (η) for H_2 evolution is given by the difference between $E_{cat/2}$ and $E_{H^+}^\circ$, where $E_{cat/2}$ is the catalytic half-current potential and $E_{H^+}^\circ$ is the standard thermodynamic potential for proton reduction with phenol under 1 atm H_2 in acetonitrile. For complex **2**, $E_{cat/2}$ is taken to be $-1.97 \text{ V vs. Fc}^{+/0}$. Accounting for the significant homoconjugation of phenol in acetonitrile solution according to Artero et al. (see Appendix B for details), we estimate $E_{BH}^\circ = -1.57 \text{ V vs. Fc}^{+/0}$ for 1.0 M phenol, which gives an overpotential of $\eta = 0.40 \text{ V}$.²⁶ Thus, while the absolute operating potential of **2** for electrocatalytic H_2 evolution is rather negative, this approach of matching the strength of the Brønsted acid source to the catalyst hydricity has proven to be an effective method for minimizing the catalytic overpotential while still obtaining efficient H_2 evolution activity.

We note that while **2** is an effective catalyst for H_2 evolution using phenol as a weak Brønsted acid, complex **1** does not exhibit electrocatalytic behavior under identical conditions with phenol, in accordance with the predicted weaker hydride donating ability of this system (vide infra). Furthermore, **1** demonstrates only marginal activity for H_2 evolution in the presence of stronger organic acids such as triethylammonium hexafluorophosphate ($\text{pK}_a = 18.82$ in acetonitrile)²⁷ (Figure 3.29). Taking $E_{cat} = -1.51 \text{ V vs. Fc}^{+/0}$ gives $i_{cat}/i_p = 1.29$, corresponding to a TOF of 2.6 s^{-1} and an overpotential of 0.29 V (see Appendix B). The lower activity of **1** may be due to comparatively large steric crowding at the nickel center from the bulkier dppe ligand. Further studies to confirm this hypothesis are underway.

Catalytic Tafel plots can be used to benchmark the electrocatalytic activity of **2** with respect to other molecular HER catalysts. By this method, the catalytic operating overpotential and TOF for H₂ evolution are compared independent of reaction conditions. The Tafel plots for **2** and other known HER catalysts were constructed in accordance with the procedure described by Artero and Saveant (see Appendix B for details), and are shown in Figure 3.10.²⁹ Catalysts are compared based on the location of the curve shoulder; those exhibiting the best energetic efficiencies (lowest overpotentials) and highest rates are characterized by a shoulder in the upper-left-most region of the plot.

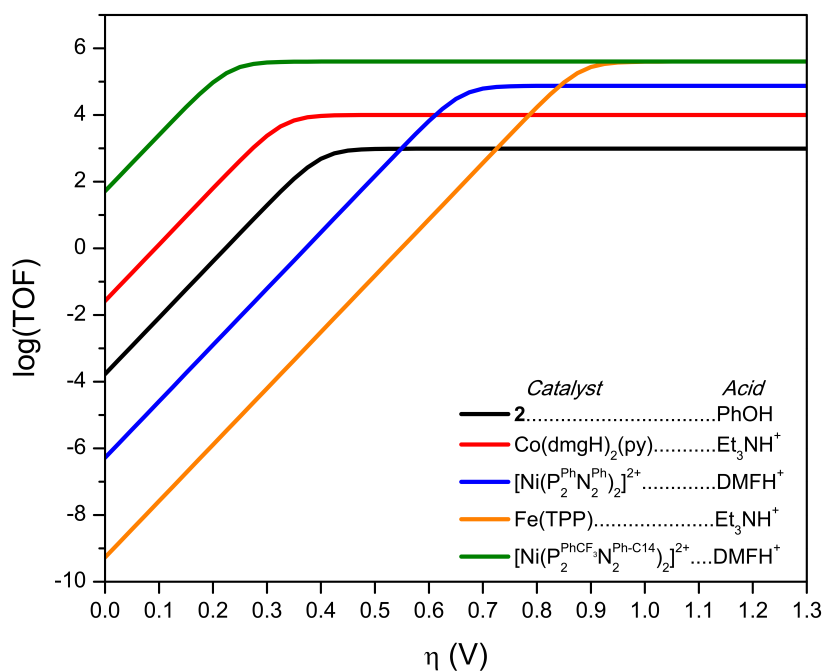


Figure 3.10: Catalytic Tafel plots for **2**, Co(dmgH)₂(py) (DMF solution),⁷ [Ni(P₂^{Ph}N₂^{Ph})₂]²⁺ (CH₃CN solution),⁵ Fe(TPP) (DMF solution),⁶ [Ni(P₂^{PhCF₃}N₂^{Ph-C14})₂]²⁺ (hexanedinitrile/H₂O solution)⁸ with 1.0 M Brønsted acid.

As seen in Figure 3.10, under the comparison conditions (1.0 M phenol), complex **2** exhibits $\log \text{TOF}_{\text{max}} = 2.99$, which is lower than the maximum rate observed for four of the most active known molecular HER catalysts. For example, **2** is 2.61 orders of magnitude slower than [Ni(P₂^{PhCF₃}N₂^{Ph-C14})₂]²⁺, the best molecular systems reported to date.⁸ While **2** is

outperformed in terms of catalytic rate, it does exhibit competitive overpotentials. Moreover, these low overpotentials are achieved through the utilization of a weak Brønsted acid source (phenol), just sufficiently acidic to favor H₂ evolution from **2H**. The other catalytic systems in Figure 3.10 were examined with much stronger organic acids. Such matching of the acid strength with the catalyst hydricity should be considered as an effective means for targeting low overpotentials for H₂ evolution.

3.3 Conclusion

Thermodynamic scaling relationships can be effectively utilized to target and predict hydricities of new, first-row transition metal complexes. Utilization of the bis-NHC ligands presented here successfully pushes reduction potentials at nickel more negative than even the most donating of their homoleptic bis-diphosphine analogues. This not only imparts two-electron redox behavior more typically observed at noble metals, but also highly reactive corresponding hydride species. Though instability of the hydrides precludes direct experimental measurement of hydricities, the hydricities can be successfully benchmarked by the selection of organic acids such that protonation of the metal hydride species is thermodynamically favored or disfavored.

Though **2** is outperformed in rate and overpotential by the recently-reported system by Wiedner et al., it remains among the lowest operating overpotentials for state of the art molecular HER catalysts. This underscores the importance of substrate selection with respect to the reduction potential of the parent complex and the hydricity of the hydride intermediate. Selecting acids such that hydrogen evolution with a given hydride is exergonic but near ergoneutral effectively levels energy landscapes, providing a mechanism by which overpotentials can be rationally minimized.

However, it is also clear that thermodynamic scaling relationships alone are not sufficient to predict and design new catalysts, as evidenced by the lack of activity of **1** with more acidic proton sources. We postulate that this is a kinetic effect, likely due to the increased steric bulk of

the dppe ligand, whereas the unhindered nickel center in **2** allows for efficient catalysis despite the absence of proton relays found in other competitive molecular HER catalysts. Further studies are ongoing to elucidate secondary-sphere kinetic effects, influence of respective acid sources, and reactivity with other substrates such as CO₂.

3.4 Experimental

General Considerations. All reactions were carried out under a nitrogen atmosphere using standard Schlenk and glovebox techniques. Solvents were sparged with argon, dried on a custom dry solvent system over alumina columns, and stored over molecular sieves before use. All reagents were obtained from commercial suppliers and used without further purification unless otherwise noted. Tetrabutylammonium hexafluorophosphate (TBAPF₆, Aldrich, 98%) was twice recrystallized from methanol and dried under a vacuum at 90°C overnight before use. The dibromide complex [Ni(bis-NHC)Br₂] and triethylammonium tetrafluoroborate (HNEt₃BF₄), were prepared according to literature procedures.^{11,32–33}

Instrumentation. ¹H and ³¹P NMR spectra were recorded on a Jeol 500 MHz spectrometer and ¹³C{¹H} NMR spectra were recorded on a Varian 500 MHz spectrometer. ¹H and ¹³C{¹H} NMR chemical shifts are reported relative to TMS (δ = 0) and referenced against residual solvent proton and carbon peaks, respectively. High resolution mass spectra were collected on an Agilent 6230 Accurate-Mass TOFMS.

Electrochemical experiments were performed in 0.1 M tetra-n-butylammonium hexafluorophosphate solution in acetonitrile using a Gamry Reference 600 potentiostat. A single-compartment cell was used for cyclic voltammetry experiments with a glassy carbon working electrode (3 mm in diameter, Bioanalytical Systems, Inc.), Pt wire counter electrode, and Ag/AgCl pseudo-reference electrode. All potentials are referenced to the Fc⁺⁰ couple using ferrocene as an internal reference. Controlled potential electrolysis experiments were carried out in a

custom 90 mL cell designed in our laboratory. The setup included a carbon rod working electrode, graphite rod counter electrode separated from the solution by a porous glass frit, and Ag/AgNO₃ pseudo-reference electrode separated from the solution by a Vycor tip. For the catalytic electrolysis studies, the cell was charged with nickel catalyst (1 mM) and phenol (0.2 M) in 0.1 M tetra-n-butylammonium hexafluorophosphate solution in acetonitrile. Hydrogen evolution was quantified by analyzing 1 mL aliquots of the headspace on a Hewlett-Packard 7890A Series gas chromatograph with two molsieve columns (30 m x 0.53 mm ID x 25 μm film). The partial pressure of H₂ in the headspace was determined by comparison to gas standard samples. Henry's Law was used to calculate the total H₂ production, given as the sum of headspace and dissolved hydrogen (see Appendix B).

X-ray Crystallography. Single crystal X-ray diffraction studies were carried out on a Bruker Kappa APEX-II CCD diffractometer equipped with Mo K_α radiation (λ = 0.71073 Å) or a Bruker Kappa APEX CCD diffractometer equipped with Cu K_α radiation (λ = 1.54184 Å). The crystals were mounted on a Cryo-loop with Paratone oil and data were collected under a nitrogen gas stream at 100(2) K using ω and φ scans. Data were integrated using the Bruker SAINT software program and scaled using the software program. Solution by direct methods (SHELXS) produced a complete phasing model consistent with the proposed structure. All non-hydrogen atoms were refined anisotropically by full-matrix least-squares (SHELXL-97).³⁴ All hydrogen atoms were placed using a riding model. Their positions were constrained relative to their parent atom using the appropriate HFIX command in SHELXL-97. Crystallographic data, structure refinement parameters, and additional notes on structure refinement are summarized in Appendix B.

Synthesis. [Ni(bis-NHC)(dppe)](PF₆)₂ **1**. A solution of NaPF₆ (425 mg, 2.69 mmol) in methanol (10 mL) was added via cannula to a stirred solution of [Ni(bis-NHC)Br₂] (207 mg, 0.387 mmol) and dppe (186 mg, 0.467 mmol) in methanol (15 mL), resulting in immediate precipitation of a pale solid. The reaction mixture was stirred at room temperature for 3 hours

and subsequently filtered. The collected solid was washed with methanol (3 x 10 mL) and diethyl ether (3 x 10 mL) and dried in vacuo at 90 °C overnight, yielding **1** as a pale yellow solid (340 mg, 83%). Crystals suitable for x-ray diffraction were grown by vapor diffusion of diethyl ether into a saturated solution of **1** in chloroform. ¹H NMR (CD₃CN): δ 7.62 (4H, m, Ph), 7.56 (8H, m, Ph), 7.46 (8H, m, Ph), 7.29 (4H, m, Ar-H), 7.23 (4H, m, Ar-H), 4.42 (4H, t br), 4.32 (4H, m br), 3.07 (4H, d, J = 18.0 Hz), 2.12 (2H, d, J = 8 Hz), 1.71 (2H, m br). ¹³C{¹H} NMR (CD₃CN): δ 179.5 (NiC), 135.3 (Ar), 133.6 (Ph), 133.4 (t, PCH₂, J = 19.5 Hz), 130.7 (t, PCH₂, J = 20.5 Hz), 128.5 (br, ArCN), 125.2 (CH₂), 111.6 (CH₂), 49.5 (CH₂), 26.6 (CH₂). ³¹P{¹H} NMR (CD₃CN): δ 52.1 (s), -144.0 ppm (m, PF₆). HRMS calcd for [C₄₆H₄₄N₄NiP₂CF₃CO₂]⁺ [(M + TFA - H)⁺] m/z 885.2240; found 885.2236.

[Ni(bis-NHC)(dmpe)](PF₆)₂ **2**. Complex **2** was prepared following the same procedure as for **1**, except dmpe was used in place of dppe. Yield 250 mg (82%). Crystals suitable for x-ray diffraction were grown by vapor diffusion of diethyl ether into a saturated solution of **2** in acetonitrile. ¹H NMR (CD₃CN): δ 7.43 (4H, m, Ar-H), 7.25 (4H, m, Ar-H), 4.84 (8H, m br), 2.34 (m br), 2.23 (4H, d, J = 17.5 Hz), 1.99 (2H, m br), 1.67 (12H, m br, CH₃). ¹³C{¹H} NMR (CD₃CN): δ 184.7 (NiC), 135.4 (Ar), 124.9 (Ar), 111.6 (CH₂) 49.6 (CH₂), 27.6 (t, J = 90 Hz, PCH₃), 27.2 (CH₂), 12.3 (t, J = 60 Hz, PCH₃). ³¹P{¹H} NMR (CD₃CN): δ 44.7 (s), -143.9 ppm (m, PF₆). HRMS calcd for [C₂₆H₃₆N₄NiP₂CF₃CO₂]⁺ [(M + TFA - H)⁺] m/z 637.1608; found 637.1614.

[Ni(bis-NHC)(dppe)]₀ **3**. To a suspension of **1** (30.0 mg, 0.0282 mmol) in THF (2 mL) was added a suspension of KC₈ (9.9 mg, 0.733 mmol) in THF (2 mL) at -38°C. The mixture was agitated for 5 minutes and allowed to warm to room temperature during which it became a deep red. The mixture was filtered through celite and solvent was removed in vacuo. The resulting solid was washed with pentane and then extracted in benzene and filtered through celite. Solvent was removed in vacuo yielding **3** as a dark red powder (16.2 mg, 74%) Crystals suitable for x-ray diffraction were grown by vapor diffusion of pentane into a saturated solution of **3** in

tetrahydrofuran. ^1H NMR (C_6D_6): δ 7.97 (8H, m, Ph), 7.16 (8H, Ph, m), 7.08 (4H, m, Ph), 6.49 (4H, m, Ar-H), 6.29 (4H, m Ar-H), 5.38 (4H, t, $J = 13$ Hz), 3.25 (4H, d, $J = 15$ Hz), 2.15 (4H, t, $J = 7$ Hz), 1.62 (2H, q, $J = 13.5$ Hz), 1.04 (2H, m). $^{13}\text{C}\{^1\text{H}\}$ NMR (C_6D_6): δ 214.8 (NiC), 144.1 (t, $J = 36.5$ Hz, Ph), 135.0 (Ph), 133.5 (Ar), 133.2 (t, $J = 37.5$ Hz, Ph), 132.7 (Ar), 128.9 (Ph), 127.3 (Ph), 120.6 (Ph), 107.7 (Ar), 45.5 (CH₂), 31.0 (CH₂), 26.4 (m, NCH₂), 24.8 (CH₂). $^{31}\text{P}\{^1\text{H}\}$ NMR (CD_3CN): δ 29.6 ppm.

Acknowledgements

Chapter 3, in full, is a reprint of the material as it appears in Ostericher, A. L.; Waldie, K. M.; Kubiak, C. P. "Utilization of Thermodynamic Saling Relationships in Hydricity to Develop Nickel Hydrogen Evolution Reaction Electrocatalysts with Weak Acids and Low Overpotentials" *ACS Catalysis*, **2018**, *8*, 9596-9603. The dissertation author was the primary author of this paper. We acknowledge Dr. Mark H. Reineke for early contributions relating to this work, Tyler Porter for invaluable discussions, and the UCSD Molecular Mass Spectrometry Facility for sample analysis. This work was supported by the Air Force Office of Scientific Research through the MURI program under AFOSR Award FA9550-10-1-0572 and is based in part upon work performed by the Joint Center for Artificial Photosynthesis, a DOE Energy Innovation Hub, supported through the Office of Science of the U.S. Department of Energy under Award No. DE-SC0004993.

3.5 References

1. Renewables 2018 Global Status Report (Paris: REN21 Secretariat), 2018. 2. Armstrong, R. C.; Wolfram, C.; de Jong, K. P.; Gross, R.; Lewis, N. S.; Boardman, B.; Ragauskas, A. J.; Ehrhardt-Martinez, K.; Crabtree, G.; Ramana, M. V., The frontiers of energy. *Nature Energy* **2016**, *1* (1), 15020.
3. Lewis, N. S., Research opportunities to advance solar energy utilization. *Science* **2016**, *351* (6271), aad1920.
4. Shaner, M. R.; Atwater, H. A.; Lewis, N. S.; McFarland, E. W., A comparative technoeconomic analysis of renewable hydrogen production using solar energy. *Energy & Environmental Science* **2016**, *9* (7), 2354-2371.
5. Helm, M. L.; Stewart, M. P.; Bullock, R. M.; DuBois, M. R.; DuBois, D. L., A Synthetic Nickel Electrocatalyst with a Turnover Frequency Above 100,000 s⁻¹ for H₂ Production. *Science* **2011**, *333* (6044), 863-866.
6. Bhugun, I.; Lexa, D.; Savéant, J.-M., Homogeneous Catalysis of Electrochemical Hydrogen Evolution by Iron(0) Porphyrins. *Journal of the American Chemical Society* **1996**, *118* (16), 3982-3983.
7. Razavet, M.; Artero, V.; Fontecave, M., Proton Electroreduction Catalyzed by Cobaloximes: Functional Models for Hydrogenases. *Inorganic Chemistry* **2005**, *44* (13), 4786-4795.
8. Klug, C. M.; Cardenas, A. J. P.; Bullock, R. M.; O'Hagan, M.; Wiedner, E. S., Reversing the Tradeoff between Rate and Overpotential in Molecular Electrocatalysts for H₂ Production. *ACS Catalysis* **2018**, *8* (4), 3286-3296.
9. Curtis, C. J.; Miedaner, A.; Ellis, W. W.; DuBois, D. L., Measurement of the Hydride Donor Abilities of [HM(diphosphine)₂]⁺ Complexes (M = Ni, Pt) by Heterolytic Activation of Hydrogen. *Journal of the American Chemical Society* **2002**, *124* (9), 1918-1925.
10. Waldie, K. M.; Ostericher, A. L.; Reineke, M. H.; Sasayama, A. F.; Kubiak, C. P., Hydricity of Transition-Metal Hydrides: Thermodynamic Considerations for CO₂ Reduction. *ACS Catalysis* **2018**, *8* (2), 1313-1324.
11. Reineke, M. H.; Porter, T. M.; Ostericher, A. L.; Kubiak, C. P., Synthesis and Characterization of Heteroleptic Ni(II) Bipyridine Complexes Bearing Bis(N-heterocyclic carbene) Ligands. *Organometallics* **2018**, *37* (3), 448-453.
12. Berning, D. E.; Noll, B. C.; DuBois, D. L., Relative Hydride, Proton, and Hydrogen Atom Transfer Abilities of [HM(diphosphine)₂]PF₆ Complexes (M = Pt, Ni). *Journal of the American Chemical Society* **1999**, *121* (49), 11432-11447.

13. Berning, D. E.; Miedaner, A.; Curtis, C. J.; Noll, B. C.; Rakowski DuBois, M. C.; DuBois, D. L., Free-Energy Relationships between the Proton and Hydride Donor Abilities of $[\text{HNi}(\text{diphosphine})_2]^+$ Complexes and the Half-Wave Potentials of Their Conjugate Bases. *Organometallics* **2001**, *20* (9), 1832-1839.
14. Galan, B. R.; Schoffel, J.; Linehan, J. C.; Seu, C.; Appel, A. M.; Roberts, J. A.; Helm, M. L.; Kilgore, U. J.; Yang, J. Y.; DuBois, D. L.; Kubiak, C. P., Electrocatalytic oxidation of formate by $[\text{Ni}(\text{P}^{\text{R}}_2 \text{N}^{\text{R}'_2})_2(\text{CH}_3\text{CN})]^{2+}$ complexes. *J Am Chem Soc* **2011**, *133* (32), 12767-79.
15. Wiese, S.; Kilgore, U. J.; DuBois, D. L.; Bullock, R. M., $[\text{Ni}(\text{PMe}_2\text{NPh}_2)_2](\text{BF}_4)_2$ as an Electrocatalyst for H_2 Production. *ACS Catalysis* **2012**, *2* (5), 720-727.
16. Yang, J. Y.; Bullock, R. M.; Dougherty, W. G.; Kassel, W. S.; Twamley, B.; DuBois, D. L.; Rakowski DuBois, M., Reduction of oxygen catalyzed by nickel diphosphine complexes with positioned pendant amines. *Dalton Transactions* **2010**, *39* (12), 3001-3010.
17. Frazee, K.; Wilson, A. D.; Appel, A. M.; Rakowski DuBois, M.; DuBois, D. L., Thermodynamic Properties of the Ni-H Bond in Complexes of the Type $[\text{HNi}(\text{P}_2^{\text{R}}\text{N}_2^{\text{R}'})_2](\text{BF}_4)$ and Evaluation of Factors That Control Catalytic Activity for Hydrogen Oxidation/Production. *Organometallics* **2007**, *26* (16), 3918-3924.
18. Yang, J. Y.; Bullock, R. M.; Shaw, W. J.; Twamley, B.; Frazee, K.; DuBois, M. R.; DuBois, D. L., Mechanistic Insights into Catalytic H_2 Oxidation by Ni Complexes Containing a Diphosphine Ligand with a Positioned Amine Base. *Journal of the American Chemical Society* **2009**, *131* (16), 5935-5945.
19. Yang, J. Y.; Smith, S. E.; Liu, T.; Dougherty, W. G.; Hoffert, W. A.; Kassel, W. S.; DuBois, M. R.; DuBois, D. L.; Bullock, R. M., Two Pathways for Electrocatalytic Oxidation of Hydrogen by a Nickel Bis(diphosphine) Complex with Pendant Amines in the Second Coordination Sphere. *Journal of the American Chemical Society* **2013**, *135* (26), 9700-9712.
20. Raebiger, J. W.; Miedaner, A.; Curtis, C. J.; Miller, S. M.; Anderson, O. P.; DuBois, D. L., Using Ligand Bite Angles To Control the Hydricity of Palladium Diphosphine Complexes. *Journal of the American Chemical Society* **2004**, *126* (17), 5502-5514.
21. Curtis, C. J.; Miedaner, A.; Raebiger, J. W.; DuBois, D. L., Periodic Trends in Metal Hydride Donor Thermodynamics: Measurement and Comparison of the Hydride Donor Abilities of the Series $\text{HM}(\text{PNP})^{2+}$ ($\text{M} = \text{Ni}, \text{Pd}, \text{Pt}$; $\text{PNP} = \text{Et}_2\text{PCH}_2\text{N}(\text{Me})\text{CH}_2\text{PEt}_2$). *Organometallics* **2004**, *23* (3), 511-516.
22. Lilio, A. M.; Reineke, M. H.; Moore, C. E.; Rheingold, A. L.; Takase, M. K.; Kubiak, C. P., Incorporation of Pendant Bases into $\text{Rh}(\text{diphosphine})_2$ Complexes: Synthesis, Thermodynamic Studies, And Catalytic CO_2 Hydrogenation Activity of $[\text{Rh}(\text{P}_2\text{N}_2)_2]^+$ Complexes. *J Am Chem Soc* **2015**, *137* (25), 8251-60.

23. Price, A. J.; Ciancanelli, R.; Noll, B. C.; Curtis, C. J.; DuBois, D. L.; DuBois, M. R., HRh(dppb)₂, a Powerful Hydride Donor. *Organometallics* **2002**, *21* (22), 4833-4839.
24. Olmstead, W. N.; Margolin, Z.; Bordwell, F. G., Acidities of water and simple alcohols in dimethyl sulfoxide solution. *The Journal of Organic Chemistry* **1980**, *45* (16), 3295-3299.
25. Kütt, A.; Movchun, V.; Rodima, T.; Dansauer, T.; Rusanov, E. B.; Leito, I.; Kaljurand, I.; Koppel, J.; Pihl, V.; Koppel, I.; Ovsjannikov, G.; Toom, L.; Mishima, M.; Medebielle, M.; Lork, E.; Röschenthaler, G.-V.; Koppel, I. A.; Kolomeitsev, A. A., Pentakis(trifluoromethyl)phenyl, a Sterically Crowded and Electron-withdrawing Group: Synthesis and Acidity of Pentakis(trifluoromethyl)benzene, -toluene, -phenol, and -aniline. *The Journal of Organic Chemistry* **2008**, *73* (7), 2607-2620.
26. Fourmond, V.; Jacques, P. A.; Fontecave, M.; Artero, V., H₂ evolution and molecular electrocatalysts: determination of overpotentials and effect of homoconjugation. *Inorg Chem* **2010**, *49* (22), 10338-47.
27. Kaljurand, I.; Kütt, A.; Sooväli, L.; Rodima, T.; Mäemets, V.; Leito, I.; Koppel, I. A., Extension of the Self-Consistent Spectrophotometric Basicity Scale in Acetonitrile to a Full Span of 28 pK_a Units: Unification of Different Basicity Scales. *The Journal of Organic Chemistry* **2005**, *70* (3), 1019-1028.
28. Faulkner, A. J. B. a. L. R., *Electrochemical Methods*. Wiley: New York, 1980.
29. Artero, V.; Saveant, J. M., Toward the Rational Benchmarking of Homogeneous H₂-Evolving Catalysts. *Energy Environ Sci* **2014**, *7* (11), 3808-3814.
30. Shi, Z.; Thummel, R. P., N,N'-Bridged Derivatives of 2,2'-Bibenzimidazole. *The Journal of Organic Chemistry* **1995**, *60* (18), 5935-5945.
31. McCarthy, B. D.; Martin, D. J.; Rountree, E. S.; Ullman, A. C.; Dempsey, J. L., Electrochemical Reduction of Brønsted Acids by Glassy Carbon in Acetonitrile—Implications for Electrocatalytic Hydrogen Evolution. *Inorganic Chemistry* **2014**, *53* (16), 8350-8361.32. Sheldrick, G., A short history of SHELX. *Acta Crystallographica Section A* **2008**, *64* (1), 112-122.

3.6 Appendix B

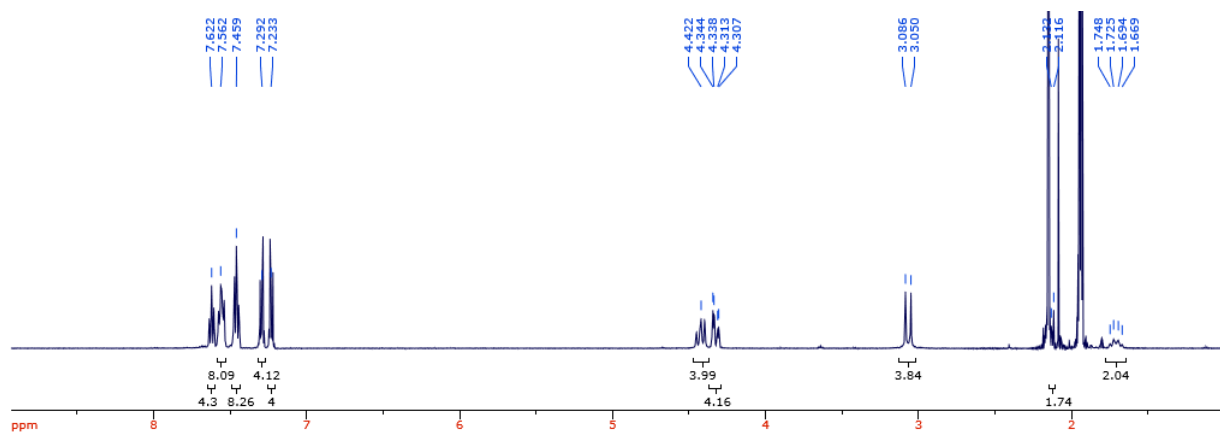


Figure 3.11: ^1H NMR (500 MHz) spectrum of **1** in CD_3CN .

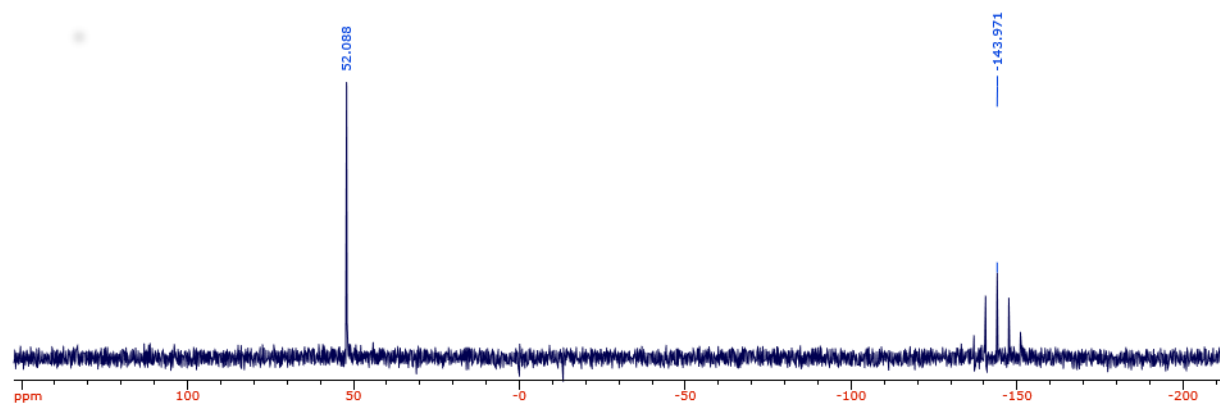


Figure 3.12: ^{31}P NMR (500 MHz) spectrum of **1** in CD_3CN .

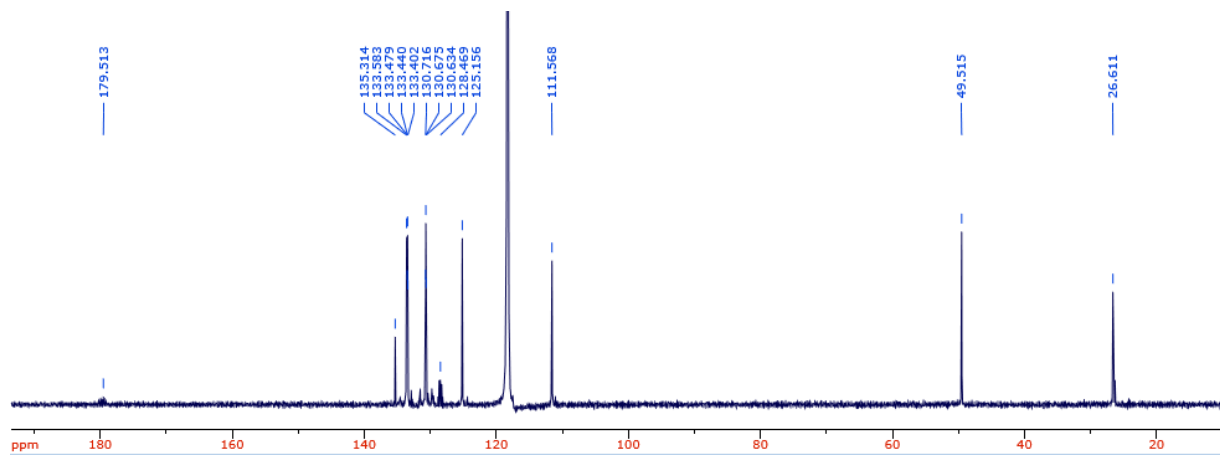


Figure 3.13: ^{13}C NMR (500 MHz) spectrum of **1** in CD_3CN .

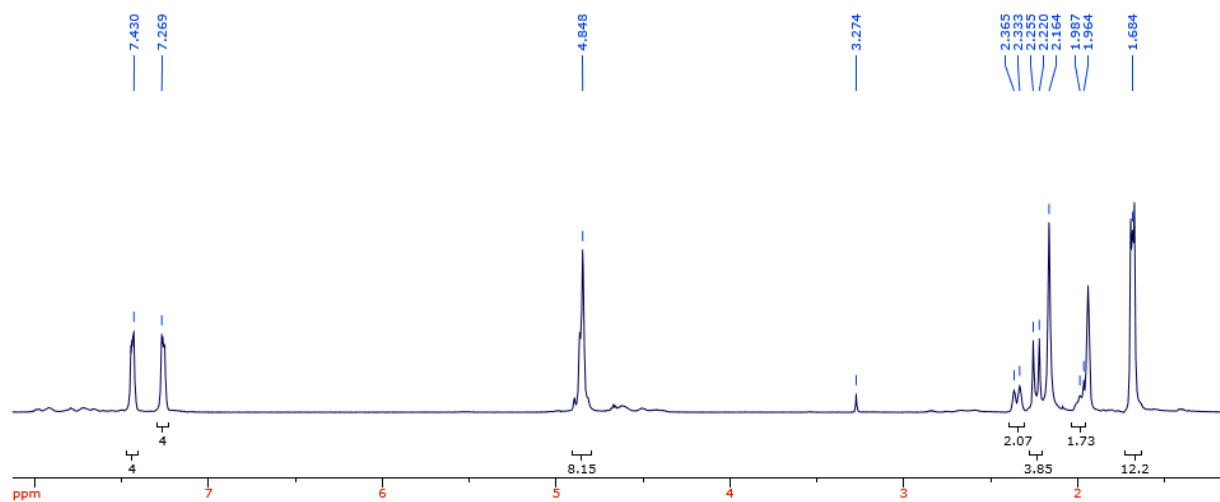


Figure 3.14: ^1H NMR (500 MHz) spectrum of **2** in CD_3CN .

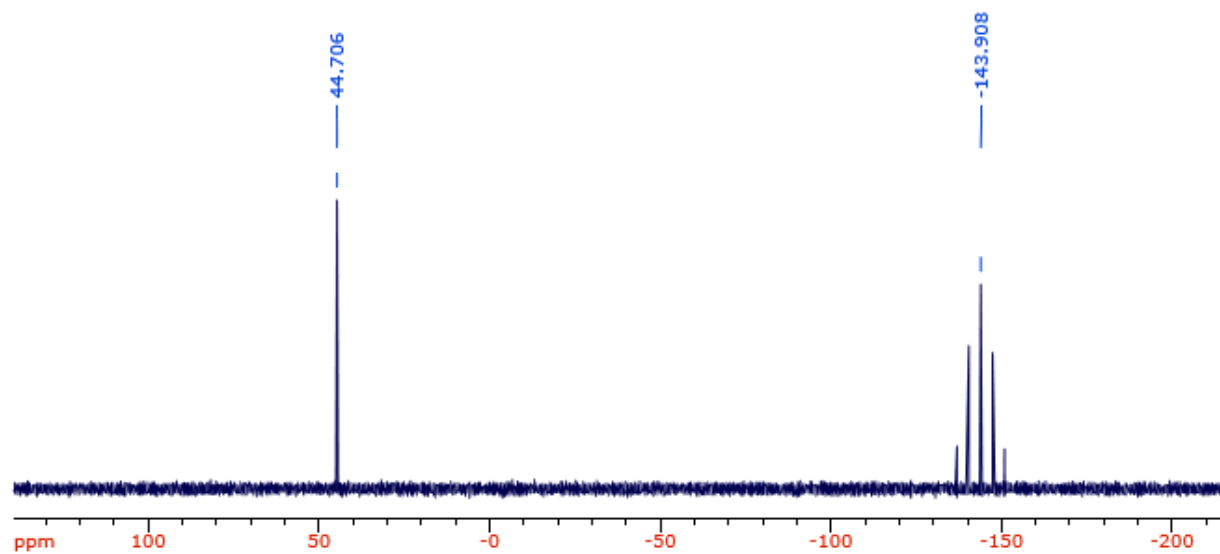


Figure 3.15: ^{31}P NMR (500 MHz) spectrum of **2** in CD_3CN .

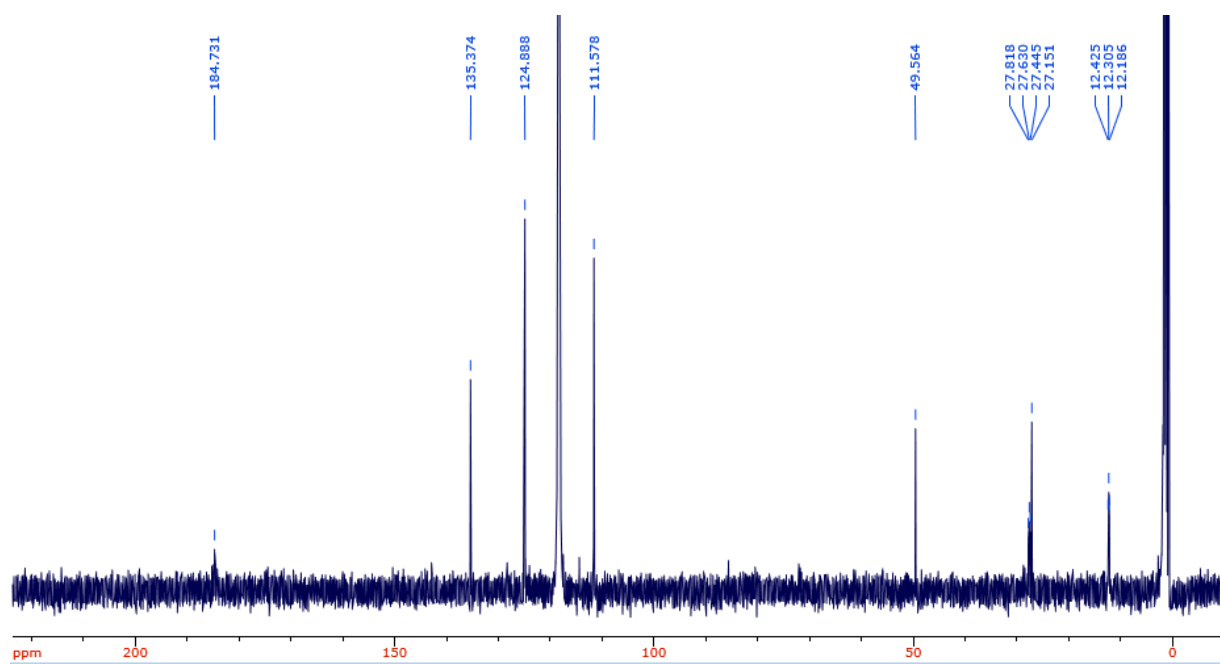


Figure 3.16: ^{13}C NMR (500 MHz) spectrum of **2** in CD_3CN .

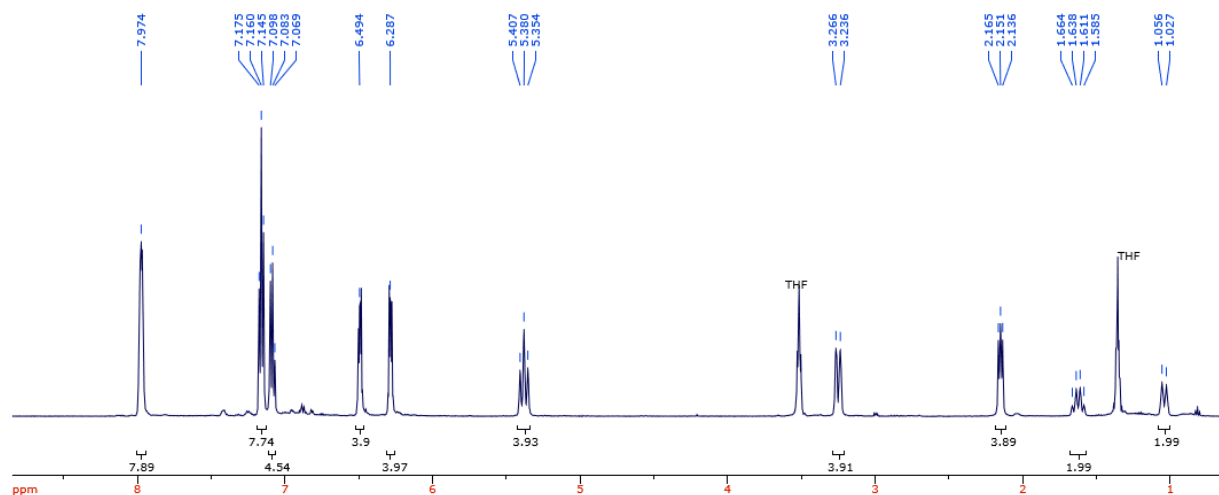


Figure 3.17: ^1H NMR (500 MHz) spectrum of **3** in C_6D_6 .

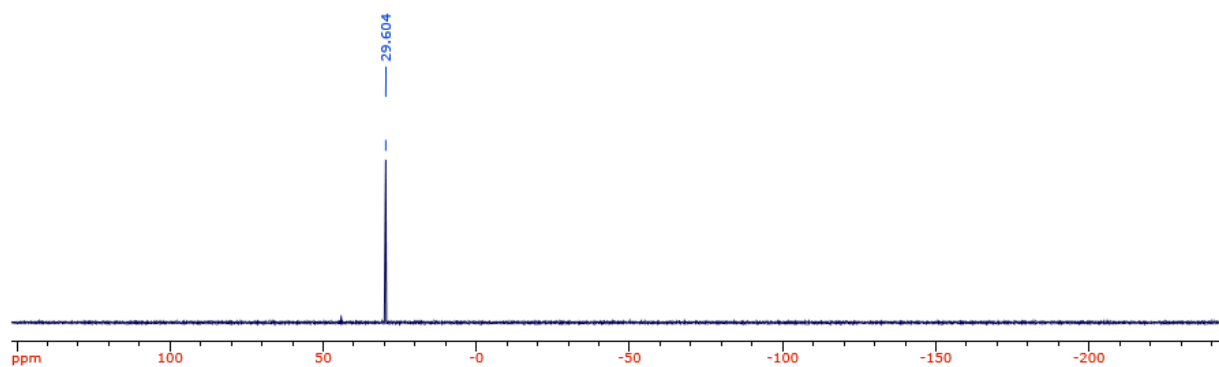


Figure 3.18: ^{31}P NMR (500 MHz) spectrum of **3** in C_6D_6 .

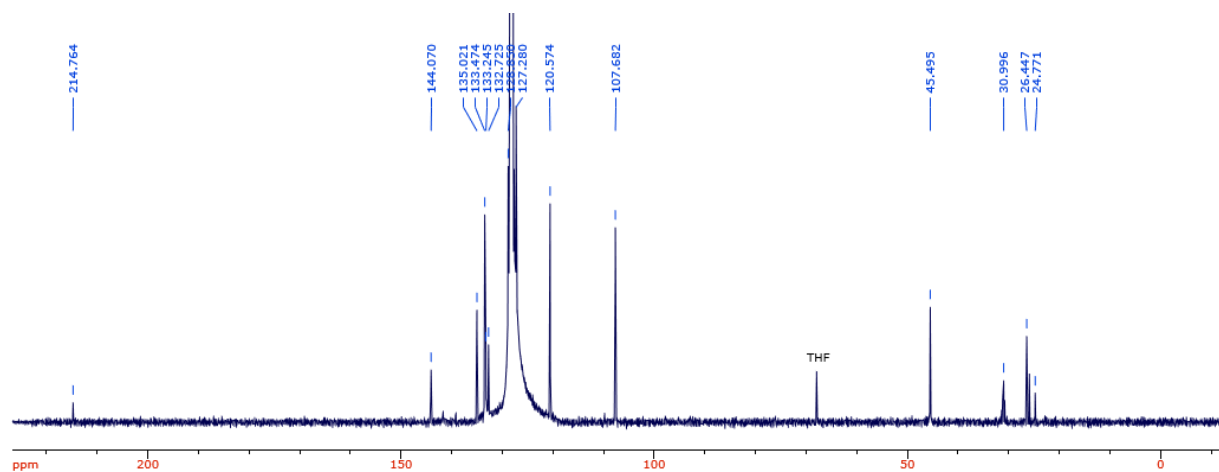


Figure 3.19: ^{13}C NMR (500 MHz) spectrum of **3** in C_6D_6 .

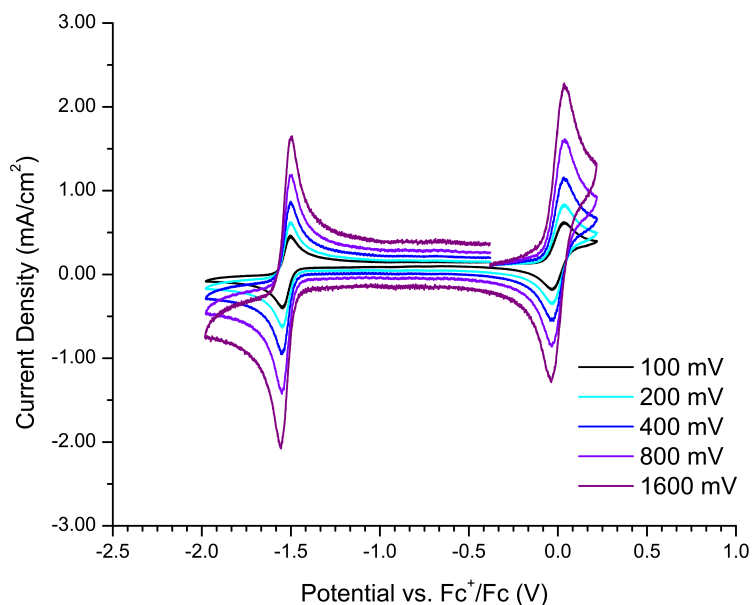


Figure 3.20: Cyclic voltammograms of **1** (1 mM) in acetonitrile. 0.1 M TBAPF₆, glassy carbon working electrode, platinum counter, Ag/AgCl reference, internal ferrocene reference.

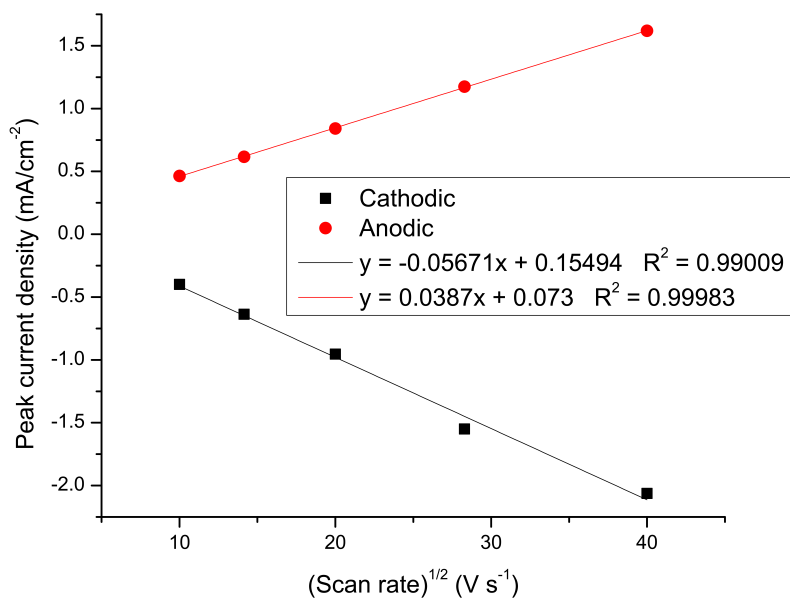


Figure 3.21: Plot of peak current vs. scan rate for **1**.

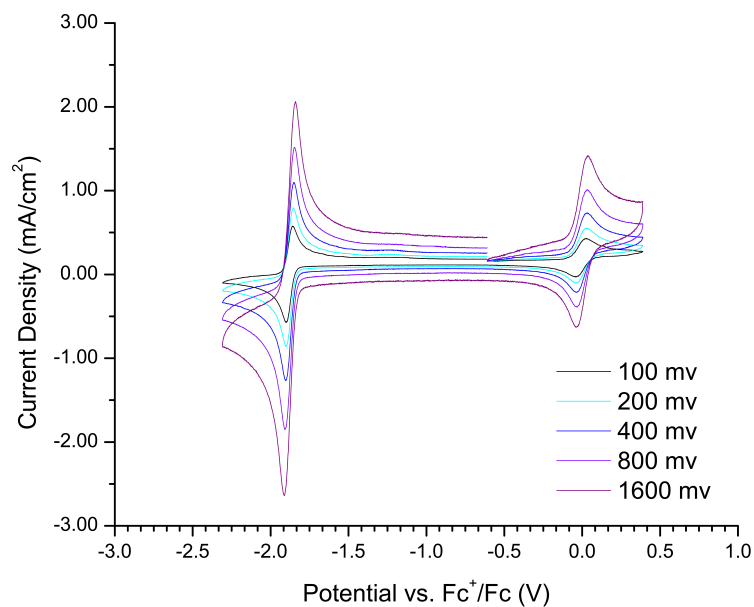


Figure 3.22: Cyclic voltammograms of **2** (1 mM) in acetonitrile. 0.1 M TBAPF₆, glassy carbon working electrode, platinum counter, Ag/AgCl reference, internal ferrocene reference.

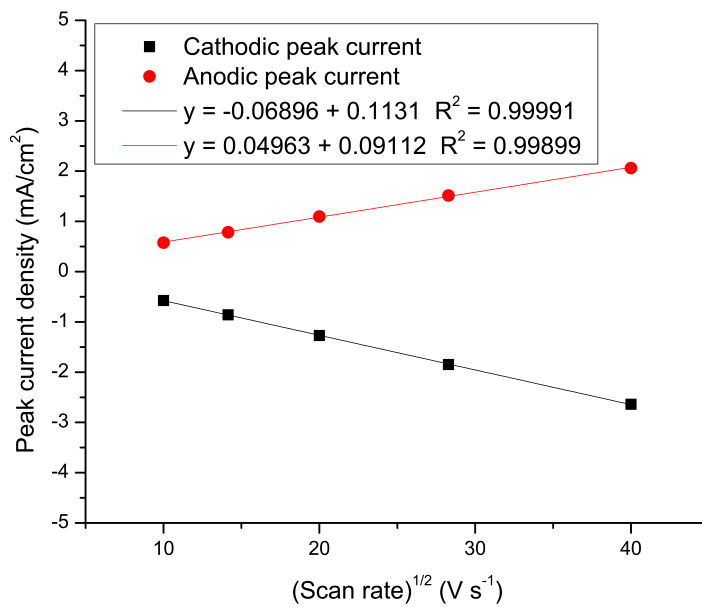


Figure 3.23: Plot of peak current vs. scan rate for **2**.

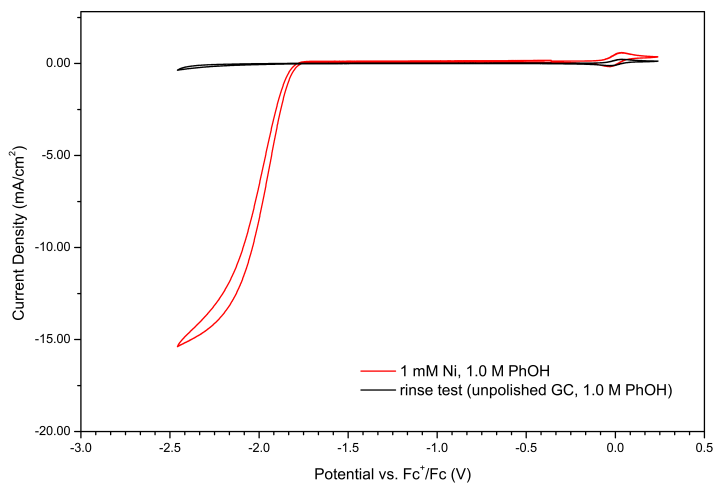


Figure 3.24: Post-catalysis electrode rinse test. Red trace: 1 mM **2**, 1.0 M phenol, 0.1 M TBAPF₆ in ACN with internal ferrocene reference. 100 mV s⁻¹ scan rate. Black trace: unpolished glassy carbon electrode post-catalysis in fresh solution with same conditions in absence of catalyst. 100 mV s⁻¹ scan rate.

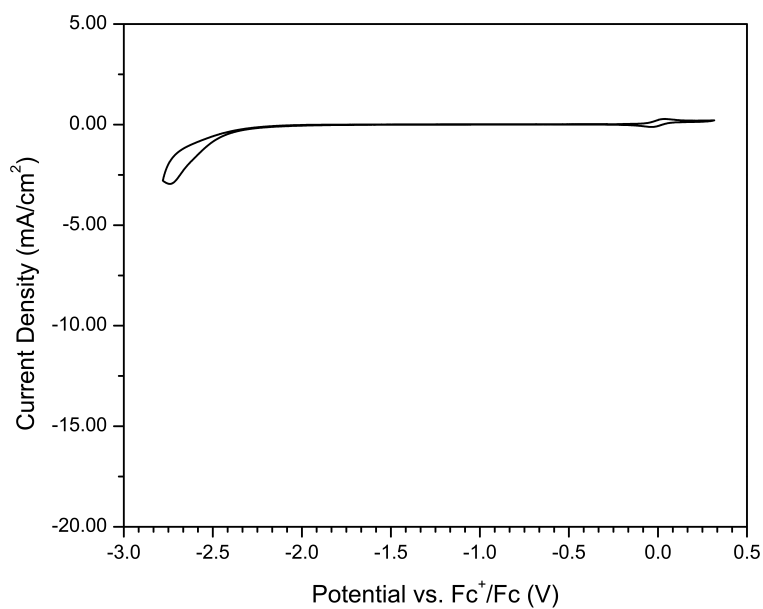


Figure 3.25: Cyclic voltammogram of phenol (3.0 M) in acetonitrile. 0.1 M TBAPF₆, glassy carbon working electrode, platinum counter, Ag/AgCl reference, internal ferrocene reference.

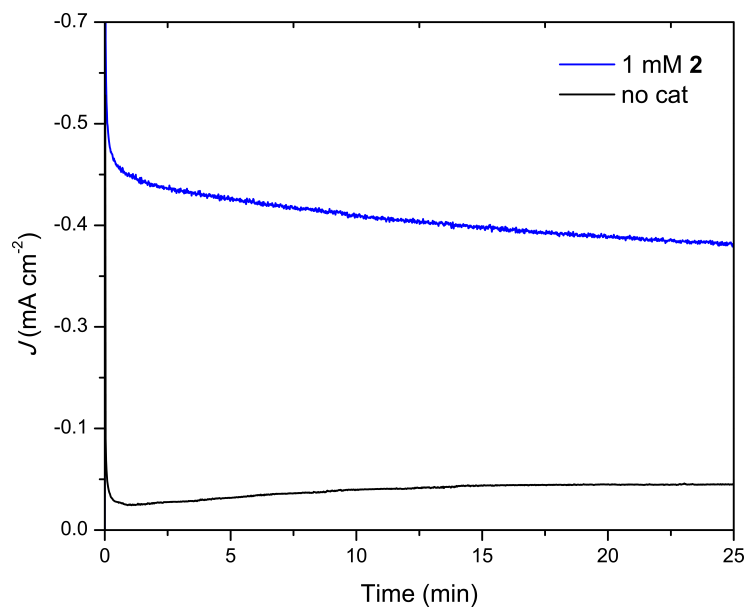


Figure 3.26: Controlled potential electrolysis at -1.9 V vs. $\text{Fc}^{+/0}$ in the presence and absence of **2**. Conditions: 0.1 M TBAPF_6 in acetonitrile with 0.2 M phenol and 1 mM Fc internal standard, glassy carbon working electrode, graphite rod counter electrode, Ag/AgNO_3 reference electrode.

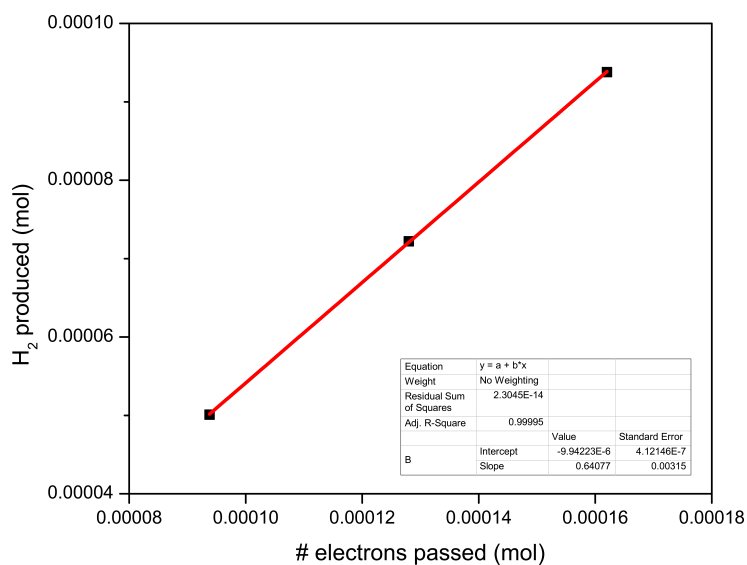


Figure 3.27: Plot of electrons passed vs H_2 produced during controlled potential electrolysis of **2** with phenol. Average Faradaic Efficiency of $112 \pm 5\%$.

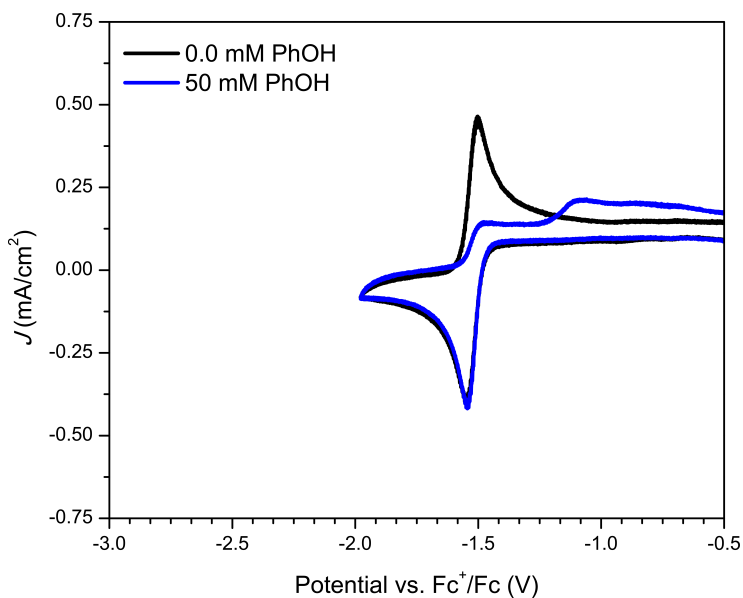


Figure 3.28: Cyclic voltammograms of **1** in presence and absence of phenol. 1 mM **1** in acetonitrile with 0.1 M TBAPF₆, glassy carbon working electrode, platinum counter, Ag/AgCl reference at 100 mV s⁻¹ scan rate.

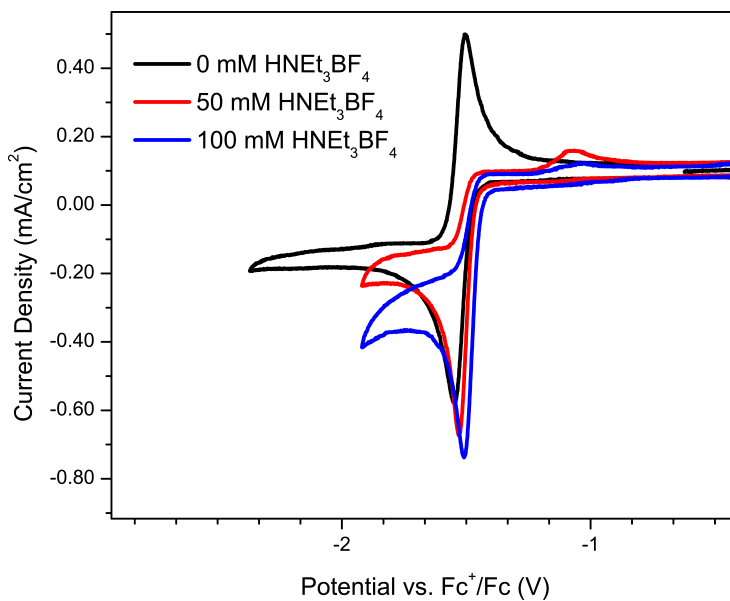


Figure 3.29: Cyclic voltammograms of **1** with varying concentrations of HNEt₃BF₄. 1 mM **1** in acetonitrile with 0.1 M TBAPF₆, glassy carbon working electrode, platinum counter, Ag/AgCl reference at 100 mV s⁻¹ scan rate.

Estimation of E_{BH}° of phenol & HNEt_3BF_4 in acetonitrile

Phenol is known to undergo significant homoconjugation in acetonitrile ($K_c = 10^{4.2}$)¹ which lowers its effective pK_a and thereby shifts the thermodynamic potential for reduction for proton reduction more positive. To more accurately estimate the thermodynamic potential for the reduction of H^+ from phenol for use in the calculation of upper benchmarks of hydricities and for determination of overpotentials, $E_{1/2(BH/BHB^-)}$ of phenol at various concentrations can be estimated according to Artero et al. by the following equation:²

$$E_{BH}^{\circ} = E_{\text{H}^+/\text{H}_2}^{\circ} - \frac{2.303RT}{F} \text{pK}_a + \epsilon_d + \frac{RT}{2F} \ln(2K_c^2 C_0 C_{\text{H}_2}^0)$$

Where,

$$E_{\text{H}^+/\text{H}_2}^{\circ} = -0.07 \text{V vs. Fc}^{+/0} \text{(ref. 2)}$$

$$R = 8.314 \text{ J mol}^{-1} \text{K}^{-1}$$

T = temperature in Kelvin

$$F = 96485.3 \text{ C mol}^{-1}$$

$$\text{pK}_a = 29.12 \text{ (phenol in acetonitrile)}^3$$

$$\epsilon_d = 40 \pm 5 \text{ mV}^2$$

K_c = homoconjugation formation constant

C_0 = concentration of acid

$$C_{\text{H}_2}^0 = 3.3 \text{ mM in acetonitrile}^4$$

Therefore, at

$$0.1 \text{ M phenol: } E_{BH}^{\circ} = -1.60 \text{ V vs Fc}^{+/0}$$

$$1.0 \text{ M phenol: } E_{BH}^{\circ} = -1.57 \text{ V vs Fc}^{+/0}$$

Using these values to estimate effective pK_a by the Nernst equation:

$$E_{BH}^{\circ} = E_{\text{H}^+/\text{H}_2}^{\circ} - \frac{2.303RT}{F} pK_a$$

Gives,

$$0.1 \text{ M phenol: } pK_a = 25.9$$

$$1.0 \text{ M phenol: } pK_a = 25.4$$

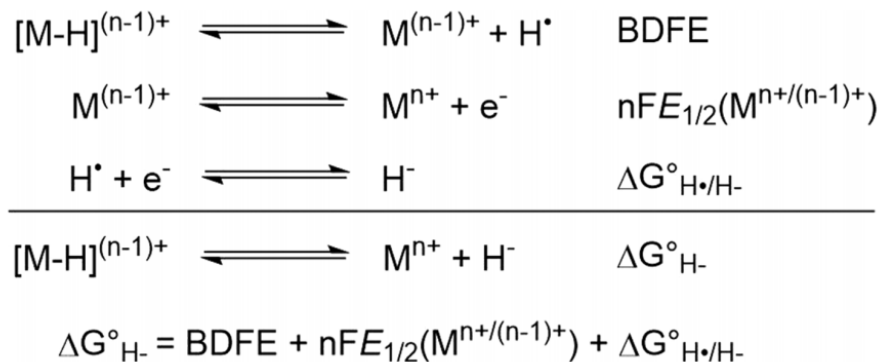
For HNEt_3BF_4 ($pK_a = 18.82$ in acetonitrile) homoconjugation is negligible and therefore:

$$E_{BH}^{\circ} = E_{\text{H}^+/\text{H}_2}^{\circ} - \frac{2.303RT}{F} pK_a$$

Gives,

$$E_{BH}^{\circ}(\text{HNEt}_3\text{BF}_4) = -1.18 \text{ V vs. Fc}^{+/0}$$

Benchmarking of hydricities



When HER is exergonic, eq. 9 becomes negative. Therefore, rearranging allows for benchmarking an upper bound for hydricity ($\Delta G^{\circ}_{H^{-}}$) given a known pK_a of added acid (BH^+), where $\Delta G^{\circ}_{H^{-}}(H_2) = 76.0 \text{ kcal mol}^{-1}$.⁵

Where HER is ergoneutral:

$$0 = \Delta G^{\circ}_{H^{-}} - \Delta G^{\circ}_{H^{-}}(H_2) + 1.364pK_a(BH)$$

Therefore, when HER is exergonic:

$$\Delta G^{\circ}_{H^{-}} < \Delta G^{\circ}_{H^{-}}(H_2) - 1.364pK_a(BH)$$

For **2** in the presence of triethylammonium tetrafluoroborate ($HNEt_3BF_4$, $pK_a = 18.82$ in acetonitrile):⁶

$$\Delta G^{\circ}_{H^{-}} < 76.0 - 1.364pK_a(18.82)$$

$$\Delta G^{\circ}_{H^{-}} < 50.3 \text{ kcal mol}^{-1}$$

For **2** in the presence of phenol, homoconjugation is significant and the estimated effective pK_a of 0.1 M phenol in acetonitrile (25.9) is used to avoid overestimation of the strength of the corresponding hydride (*vide supra*).

$$\Delta G^{\circ}_{H^{-}} < 76.0 - 1.364pK_a(25.9)$$

$$\Delta G^{\circ}_{H^{-}} < 40.7 \text{ kcal mol}^{-1}$$

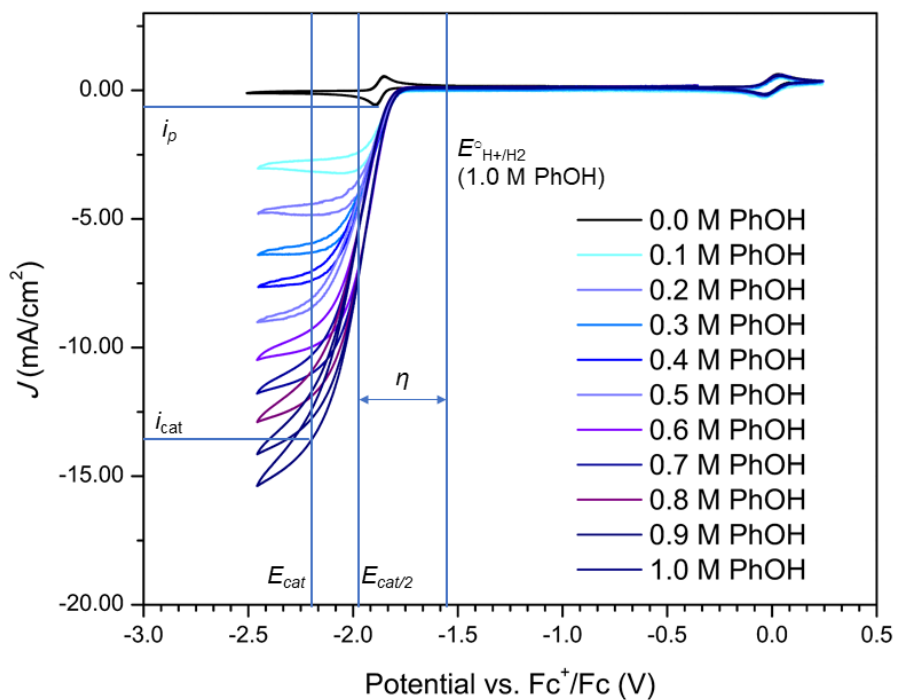


Figure 3.30: Graphical representation of i_{cat} , i_p , E_{cat} , $E_{cat/2}$, and E_{H^+/H_2}^{circ} , for rate and overpotential determination following methods by Appel and Helm.⁷

Determination of overpotential with 2 and phenol

Taking $E_{cat} = -2.22$ V vs. $Fc^{+/0}$

Gives,

$$E_{cat/2} = -1.97 \text{ V vs. } Fc^{+/0}$$

Where current = $i_{cat/2}$

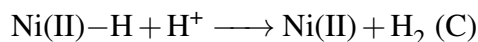
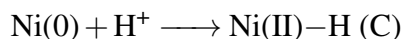
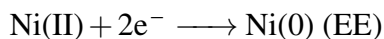
Since overpotential (η) is defined by:

$$\eta = |E_{cat/2} - E_{H^+/H_2}^{\circ} (1.0 \text{ M phenol})|$$

$$\eta = |-1.97 - (-1.57)| = 400 \text{ mV}$$

Tafel Analysis

Assuming an EECC-type mechanism for HER of the following:



We have followed Artero and Saveant's procedures for constructing Tafel plots by the following equations:⁸

$$\frac{i_{cat}}{i_p} = 4.484 \sqrt{k_1 [BH]} \sqrt{\frac{RT}{Fv n_p^3}}$$

$$k_1 = \frac{(0.223 \frac{i_{cat}}{i_p} \sqrt{(\frac{Fv n_p^3}{RT})^2})}{[BH]}$$

$$TOF_{max} = k_1 [BH]$$

$$TOF = \frac{TOF_{max}}{1 + \exp[\frac{F}{RT}(E_{\text{H}^+/\text{H}_2}^\circ - E_{cat/2})] \exp[\frac{F}{RT}\eta]}$$

Where,

$$\frac{i_{cat}}{i_p} = 25.1$$

$$\frac{F}{RT} = 38.92 \text{ V}^{-1}$$

$$v = 0.1 \text{ V}^{-1}$$

$$n_p = 2$$

$$E_{\text{H}^+/\text{H}_2}^\circ = -1.57 \text{ V vs Fc}^{+/0} \text{ (for 1.0 M phenol in acetonitrile as estimated above)}$$

$$E_{cat/2} = -1.97 \text{ V vs Fc}^{+/0}$$

Crystallographic Data

Table 3.2: Crystal data and structure refinement for Complex 1. (CCDC: 1852576)

Empirical formula	C ₄₇ H ₄₅ Cl ₃ F ₁₂ N ₄ NiP ₄
Formula weight	1182.81
Temperature/K	100.0
Crystal system	triclinic
Space group	P-1
a/Å	11.4277(4)
b/Å	13.1720(5)
c/Å	20.4025(8)
α/°	86.1230(10)
β/°	86.8440(10)
γ/°	64.9950(10)
Volume/Å ³	2775.69(18)
Z	2
ρ _{calc} /g/cm ³	1.415
μ/mm ⁻¹	3.597
F(000)	1204.0
Crystal size/mm ³	0.16 x 0.16 x 0.20
Radiation	CuKα (λ = 1.54178)
2θ range for data collection/°	4.342 to 140.14
Index ranges	-13 ≤ h ≤ 13, -16 ≤ k ≤ 16, -21 ≤ l ≤ 24
Reflections collected	51195
Independent reflections	10326 [R _{int} = 0.0415, R _{sigma} = 0.0288]
Data/restraints/parameters	10326/0/640
Goodness-of-fit on F ²	1.025
Final R indexes [I ≥ 2σ (I)]	R ₁ = 0.0467, wR ₂ = 0.1263
Final R indexes [all data]	R ₁ = 0.0484, wR ₂ = 0.1279
Largest diff. peak/hole / e Å ⁻³	1.35/-0.68

Notes on refinement. The SQUEEZE routine in PLATON was used to omit density assigned to one highly-disordered molecule of chloroform in the unit cell.

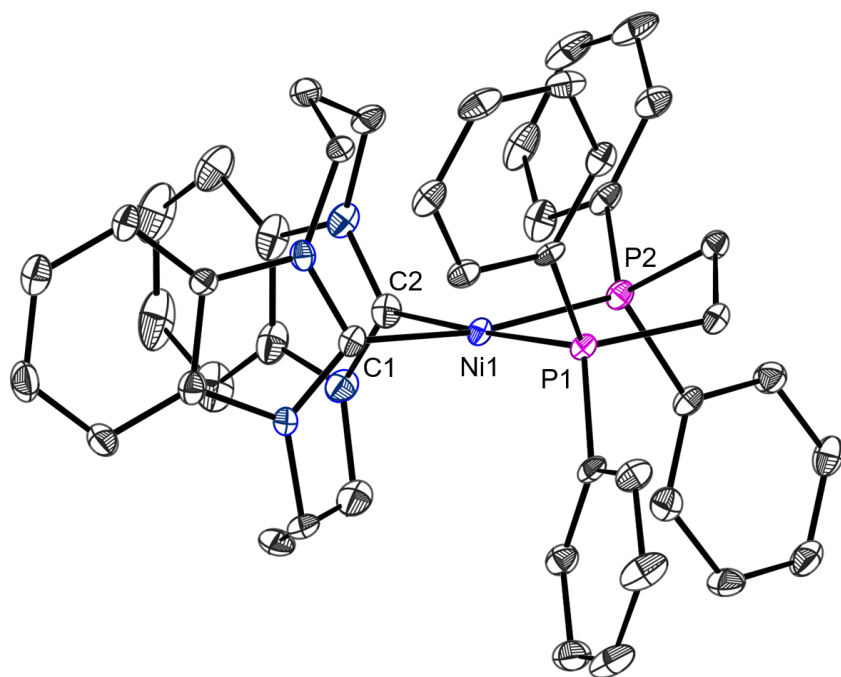


Table 3.3: Selected bond distances for complex **1**.

Atom	Atom	Length/Å
Ni1	P1	2.2196(7)
Ni1	P2	2.2063(7)
Ni1	C2	1.894(3)
Ni1	C1	1.900(2)

Table 3.4: Selected bond angles for complex **1**.

Atom	Atom	Atom	Angle/°
P2	Ni1	P1	86.85(3)
C2	Ni1	P1	175.63(8)
C2	Ni1	P2	95.40(8)
C2	Ni1	C1	79.80(10)
C1	Ni1	P1	97.42(7)
C1	Ni1	P2	170.59(8)

Table 3.5: Crystal data and structure refinement for Complex **2**. (CCDC: 1851821)

Empirical formula	$C_{28}H_{39}F_{12}N_5NiP_4$
Formula weight	856.23
Temperature/K	100.0
Crystal system	monoclinic
Space group	P21/n
a/Å	10.162(3)
b/Å	12.106(3)
c/Å	31.001(8)
$\alpha/^\circ$	90
$\beta/^\circ$	90.092(8)
$\gamma/^\circ$	90
Volume/Å ³	3813.8(17)
Z	4
$\rho_{calc}/\text{g}/\text{cm}^3$	1.491
μ/mm^{-1}	0.763
F(000)	1752.0
Crystal size/mm ³	0.4 x 0.1 x 0.1
Radiation	MoK α ($\lambda = 0.71073$)
2 Θ range for data collection/ $^\circ$	2.628 to 52.742
Index ranges	$-12 \leq h \leq 12, -15 \leq k \leq 15, -38 \leq l \leq 38$
Reflections collected	41073
Independent reflections	7792 [$R_{int} = 0.0601, R_{sigma} = 0.0482$]
Data/restraints/parameters	7792/0/457
Goodness-of-fit on F_2	1.112
Final R indexes [$I \geq 2\sigma(I)$]	$R_1 = 0.0622, wR_2 = 0.1461$
Final R indexes [all data]	$R_1 = 0.0750, wR_2 = 0.1572$
Largest diff. peak/hole / e Å ⁻³	1.24/-0.93

Notes on refinement. Twinned data refinement Scales: 0.6110(16); 0.3890(16). Twin law: [-1.0, 0.0, 0.0, 0.0, -1.0, 0.0, 0.0, 0.0, 1.0]. The SQUEEZE routine in PLATON was used to omit density assigned to one highly-disordered molecule of diethyl ether in the unit cell.

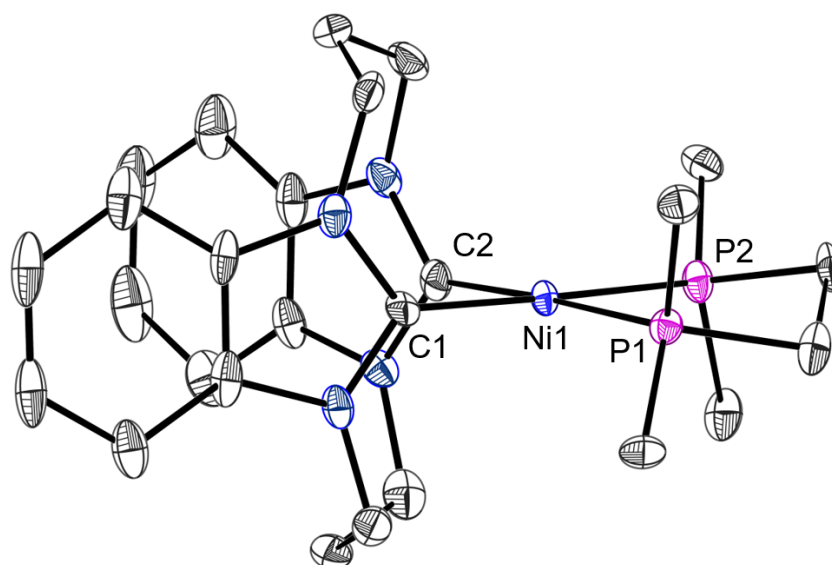


Table 3.6: Selected bond distances for complex **2**.

Atom	Atom	Length/Å
Ni1	P1	2.1859(14)
Ni1	P2	2.1710(14)
Ni1	C1	1.900(4)
Ni1	C2	1.899(5)

Table 3.7: Selected bond angles for complex **2**.

Atom	Atom	Atom	Angle/°
P2	Ni1	P1	87.93(5)
C1	Ni1	P1	96.97(13)
C1	Ni1	P2	175.07(14)
C2	Ni1	P1	177.33(18)
C2	Ni1	P2	93.50(14)
C2	Ni1	C1	81.62(19)

Table 3.8: Crystal data and structure refinement for Complex **3**. (CCDC: 1851844)

Empirical formula	C ₄₆ H ₄₄ N ₄ NiP ₂
Formula weight	773.50
Temperature/K	100.0
Crystal system	monoclinic
Space group	C2/c
a/Å	21.5537(9)
b/Å	15.6323(8)
c/Å	23.5228(11)
α/°	90
β/°	102.908(3)
γ/°	90
Volume/Å ³	7725.3(6)
Z	8
ρ _{calc} /g/cm ³	1.330
μ/mm ⁻¹	1.799
F(000)	3248.0
Crystal size/mm ³	0.4 x 0.1 x 0.1
Radiation	CuKα (λ = 1.54178)
2θ range for data collection/°	7.048 to 136.948
Index ranges	-25 ≤ h ≤ 25, -18 ≤ k ≤ 18, -28 ≤ l ≤ 28
Reflections collected	25596
Independent reflections	7038 [R _{int} = 0.1038, R _{sigma} = 0.0879]
Data/restraints/parameters	7038/0/478
Goodness-of-fit on F ₂	0.978
Final R indexes [I ≥ 2σ (I)]	R ₁ = 0.0464, wR ₂ = 0.0930
Final R indexes [all data]	R ₁ = 0.0879, wR ₂ = 0.1064
Largest diff. peak/hole / e Å ⁻³	0.48/-0.33

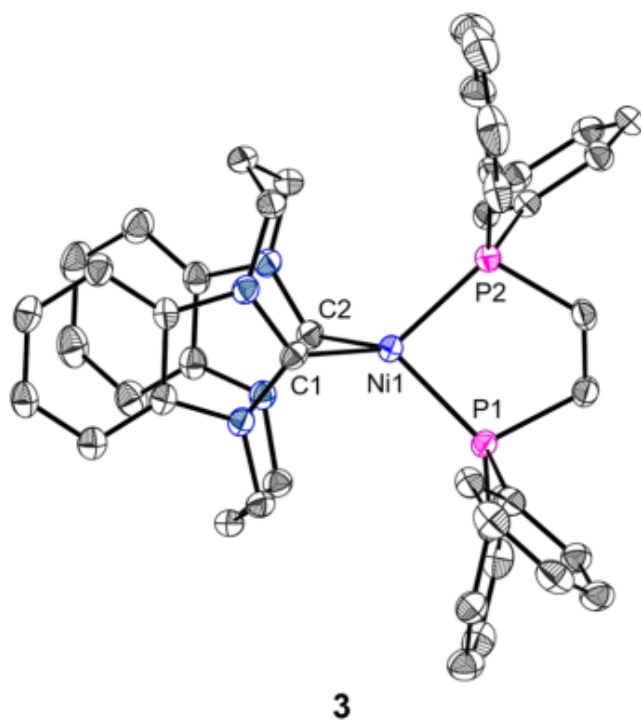


Table 3.9: Selected bond distances for complex **3**.

Atom	Atom	Length/Å
Ni1	P2	2.1643(8)
Ni1	P1	2.1642(9)
Ni1	C1	1.921(3)
Ni1	C2	1.914(3)

Table 3.10: Selected bond angles for complex **3**.

Atom	Atom	Atom	Angle/°
P1	Ni1	P2	88.42(3)
C1	Ni1	P2	125.61(9)
C1	Ni1	P1	122.93(10)
C2	Ni1	P2	118.91(9)
C2	Ni1	P1	123.78(10)
C2	Ni1	C1	81.76(12)

Appendix B References

1. McCarthy, B. D.; Martin, D. J.; Rountree, E. S.; Ullman, A. C.; Dempsey, J. L., Electrochemical Reduction of Brønsted Acids by Glassy Carbon in Acetonitrile—Implications for Electrocatalytic Hydrogen Evolution. *Inorganic Chemistry* **2014**, *53* (16), 8350-8361.
2. Fourmond, V.; Jacques, P. A.; Fontecave, M.; Artero, V., H₂ evolution and molecular electrocatalysts: determination of overpotentials and effect of homoconjugation. *Inorg Chem* **2010**, *49* (22), 10338-47.
3. Kütt, A.; Movchun, V.; Rodima, T.; Dansauer, T.; Rusanov, E. B.; Leito, I.; Kaljurand, I.; Koppel, J.; Pihl, V.; Koppel, I.; Ovsjannikov, G.; Toom, L.; Mishima, M.; Medebielle, M.; Lork, E.; Röschenthaler, G.-V.; Koppel, I. A.; Kolomeitsev, A. A., Pentakis(trifluoromethyl)phenyl, a Sterically Crowded and Electron-withdrawing Group: Synthesis and Acidity of Pentakis(trifluoromethyl)benzene, -toluene, -phenol, and -aniline. *The Journal of Organic Chemistry* **2008**, *73* (7), 2607-2620.
4. Brunner, E., Solubility of hydrogen in 10 organic solvents at 298.15, 323.15, and 373.15 K. *Journal of Chemical & Engineering Data* **1985**, *30* (3), 269-273.
5. Curtis, C. J.; Miedaner, A.; Ellis, W. W.; DuBois, D. L., Measurement of the Hydride Donor Abilities of [HM(diphosphine)₂]⁺ Complexes (M = Ni, Pt) by Heterolytic Activation of Hydrogen. *Journal of the American Chemical Society* **2002**, *124* (9), 1918-1925.
6. Kaljurand, I.; Kütt, A.; Sooväli, L.; Rodima, T.; Mäemets, V.; Leito, I.; Koppel, I. A., Extension of the Self-Consistent Spectrophotometric Basicity Scale in Acetonitrile to a Full Span of 28 pK_a Units: Unification of Different Basicity Scales. *The Journal of Organic Chemistry* **2005**, *70* (3), 1019-1028.
7. Appel, A. M.; Helm, M. L., Determining the Overpotential for a Molecular Electrocatalyst. *ACS Catalysis* **2014**, *4* (2), 630-633.
8. Artero, V.; Saveant, J. M., Toward the Rational Benchmarking of Homogeneous H₂-Evolving Catalysts. *Energy Environ Sci* **2014**, *7* (11), 3808-3814.

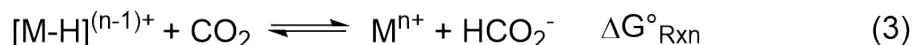
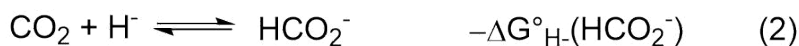
Chapter 4

Thermodynamic Targeting of Electrocatalytic CO₂ Reduction: Advantages, Limitations, and Insights for Catalyst Design

4.1 Introduction

Electrochemical reduction of CO₂ to value-added products represents an attractive approach to mitigating the adverse effects of anthropogenic emission of CO₂ while simultaneously manufacturing economically desirable products.^{1–5} The two-electron, two-proton reduction of CO₂ to carbon monoxide or formic acid, are two pathways of particular interest due to their applications in Fischer-Tropsch and formic acid fuel cells, respectively.^{4,6} Our lab and others have studied homogeneous metal hydride tuning as a means of targeting efficient catalysts for CO₂ reduction.^{7–15} Hydricity (ΔG_{H-}°), is the propensity of hydride transfer from a hydride donor and plays a key role in determining the subsequent reactivity of the metal hydride donor with a

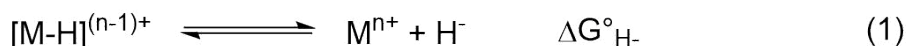
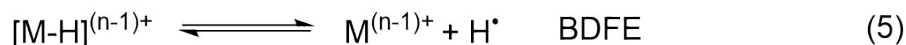
given substrate. In the case of CO₂, thermodynamically favorable hydride transfer from a metal hydride to CO₂ to produce formate requires the hydricity of the hydride donor to be stronger than formate ($\Delta G_{H^-}^\circ < 44 \text{ kcal mol}^{-1}$ in acetonitrile).¹² (Figure 4.1)



$$\Delta G_{\text{Rxn}}^\circ = \Delta G_{\text{H}^-}^\circ([\text{M-H}]^{(n-1)+}) - \Delta G_{\text{H}^-}^\circ(\text{HCO}_2^-) \quad (4)$$

Figure 4.1: Thermochemical cycle for hydride transfer to CO₂.

In an effort to tune and target hydride donors to catalyze CO₂ reduction, our lab has recently expanded on a useful scaling relationship that was initially noted by Berning et al. in 2001 between hydricity and the first reduction potential of the parent metal complex ($E_{1/2}(\text{M}^{n+}/(n-1)+)$) (Figure 4.4). This relationship is well-modeled by eq 8 (Figure 4.2),¹⁶⁻¹⁷ and not only provides a mechanism for predicting hydricity based on $E_{1/2}(\text{M}^{n+}/(n-1)+)$ but also establishes a road map for targeting highly reactive transition metal hydride species: Since hydricity is directly proportional to $E_{1/2}(\text{M}^{n+}/(n-1)+)$, more hydridic hydrides can be accessed through the consideration of ligand field effects.



$$\Delta G_{\text{H}^-}^\circ = \text{BDFE} + nFE_{1/2}(\text{M}^{n+}/(n-1)+) + \Delta G_{\text{H}^\bullet/\text{H}^-}^\circ \quad (8)$$

Figure 4.2: Hydricity in terms of BDFE and $E_{1/2}(\text{M}^{n+}/(n-1)+)$.

However, electrocatalytic CO₂ reduction can give rise to a variety of distinct mechanistic pathways, each resulting in different product selectivity, which is very clearly discussed by the Yang group in a recent perspective article.¹³ We herein describe the electrochemical reactivity of a recently-reported heteroleptic nickel complex bearing highly σ -donating N-heterocyclic carbenes (NHC's) to target reactive hydrides with CO₂. This marks an illustrative example of these divergent pathways and the challenges associated with rational design of selective CO₂ reduction electrocatalysts.

4.2 Results and Discussion

4.2.1 Overview of the System Studied

In an effort to probe and study the scaling relationship between hydricity (ΔG_{H-}°) and the first reduction potential of the parent metal complex ($E_{1/2}(M^{n+/(n-1)+})$) we began exploring several N-heterocyclic carbene nickel complexes in conjunction with eq. 8 to target first-row transition metal hydrides capable of catalyzing the reduction of CO₂ to formate.¹⁸⁻²⁻ By this relationship, the hydricity of the metal hydride complex is predicted to increase with increasing electron density at the metal center; i.e. ΔG_{H-}° becomes more negative as $E_{1/2}(M^{n+/(n-1)+})$ becomes more negative. While nickel bis-diphosphine complexes would be a convenient starting point, we opted to investigate their heteroleptic analogues that feature the bis-NHC ligand: 1,1':3,3'-bis(1,3-propanediyl)dibenzimidazolin-2,2'-diylidene, as even the most donating nickel bis-diphosphine complex $[\text{Ni}(\text{dmpe})_2]^{2+}$ (dmpe = 1,2-Bis(dimethylphosphino)ethane) does not yield hydrides of sufficient reactivity under standard conditions.^{8,21} Furthermore, the geometric constraints of the bis-NHC ligands allows synthesis of several to heteroleptic nickel diphosphine complexes where further tuning of the electron density at nickel can be attained.²⁰

Estimation of the hydricity for complex **1** was obtained through application of eq. 8 using the fixed-slope line in our scaling relationship (Figure 4.4). Cyclic voltammograms of complex

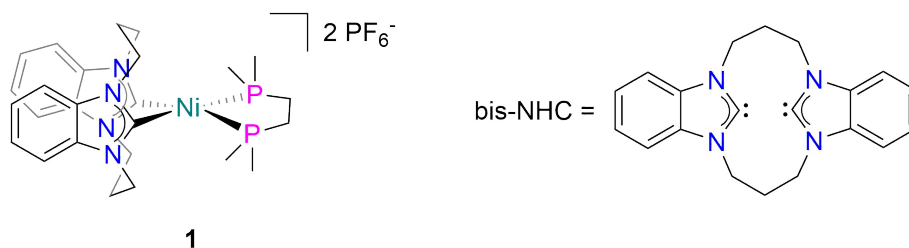


Figure 4.3: Complex **1** and bis-NHC ligand.

1 (Figure 4.5) show a reversible two electron reduction at $-1.87\text{ V vs Fc}^{+/0}$ which predicts a hydricity for the corresponding hydride to be $\sim 37.8\text{ kcal mol}^{-1}$. This is in excellent agreement with the experimentally benchmarked value which is found to be less than $40.6\text{ kcal mol}^{-1}$.²⁰ These values indicate that hydride transfer to CO_2 is thermodynamically favorable by $\sim 6\text{ kcal mol}^{-1}$ with a driving force of at least $\sim 3.4\text{ kcal mol}^{-1}$.

4.2.2 Electrocatalytic CO_2 Reduction

In the presence of phenol, **1** shows significant current enhancement at the Ni(II/0) couple which corresponds to hydrogen evolution with 100% FE (Figure 4.5b). Interestingly however, upon the introduction of a CO_2 atmosphere, a significant change in the electrocatalytic response is observed (Figure 4.5a), indicative of either an entirely different catalytic process or the emergence of a competing process. The electrocatalytic current is significantly reduced in the presence of CO_2 , exhibiting a decrease in i_{cat}/i_p from 13.8 at 0.4 M phenol under N_2 to 9.34 at 0.4 M phenol under CO_2 , where i_{cat} and i_p correspond to the plateau catalytic current and the peak current in the absence of substrate, respectively.²² This suggests that the competing process is slow with respect to the hydrogen evolution observed in the presence of phenol under an inert atmosphere or simply blocks it from proceeding.

Secondly, introduction of a CO_2 atmosphere results in a significant change in the shape of the catalytic wave, suggesting a kinetically distinct catalytic processes. In the absence of CO_2 , the catalytic wave exhibits near ideal S-shaped behavior, indicative of “pure kinetic” conditions

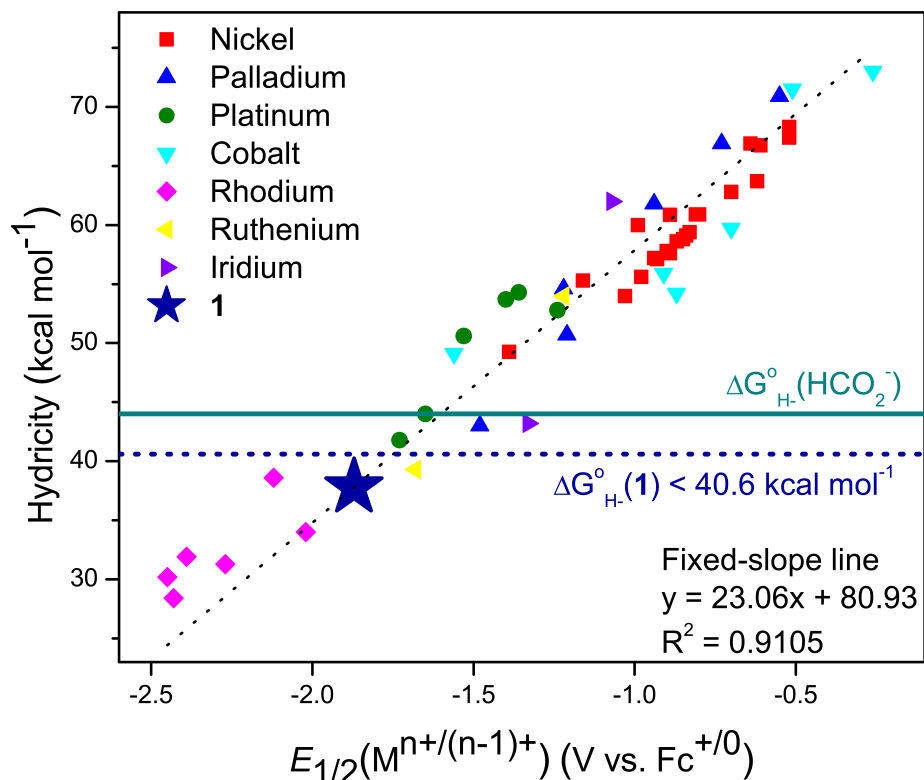


Figure 4.4: Plot of known hydricities of $d^{8/9}$ metals versus $E_{1/2}(M^{n+/(n-1)+})$ (adapted from ref. 17). The hydricity of formate (44 kcal mol^{-1}) is indicated by the cyan line. The predicted hydricity of **1** (based on the fixed-slope line) and the experimentally-determined upper bound thereof are denoted by the blue star and dashed line, respectively.

corresponding to fast catalysis unhindered by substrate consumption in the diffusion layer.²³ Conversely, a peak-shaped current response is observed under an atmosphere of CO_2 , most often indicating substrate consumption or other “side phenomena” such as substrate inhibition or catalyst deactivation.^{24–25}

While the electrocatalytic response from the CVs under a CO_2 atmosphere would initially suggest the possibility of competitive hydride transfer to CO_2 , yielding formate, CPE experiments performed under identical conditions at -1.75 V show only the production of CO and hydrogen at 25% and 55% FE respectively (Figures 4.10-11). The remaining unaccounted passed charge is most likely due to catalyst degradation under these conditions (*vide infra*).

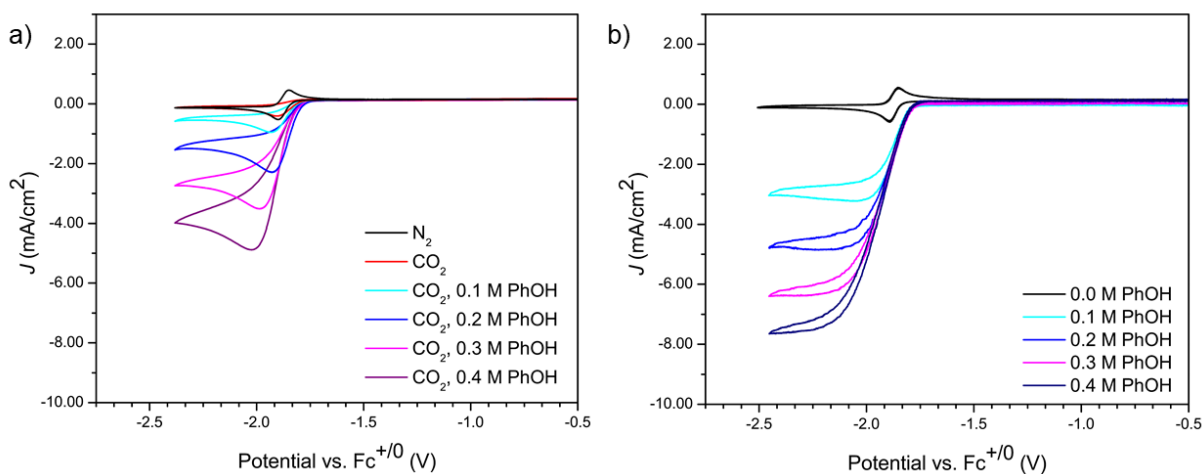


Figure 4.5: **a)** Cyclic voltammograms of **1** (1 mM) in the presence of phenol (up to 0.4 M) under an atmosphere of CO_2 . Conditions: 0.1 M Bu_4NPF_6 in acetonitrile saturated with CO_2 at 100 mV s^{-1} ; glassy carbon working electrode; platinum counter electrode; Ag/AgCl reference electrode. **b)** Cyclic voltammograms of **1** (1 mM) in the presence of phenol (up to 0.4 M) under an atmosphere of N_2 . Conditions: 0.1 M Bu_4NPF_6 in acetonitrile at 100 mV s^{-1} ; glassy carbon working electrode; platinum counter electrode; Ag/AgCl reference electrode.

In order to suppress hydrogen evolution, methanol can be utilized as the added proton source to avoid protonation of the electrochemically-generated hydride. Addition of methanol followed by introduction of a CO_2 atmosphere yields mild current enhancement at the Ni(II/0) couple in conjunction with a disappearance of the hydride oxidation feature at -1.15 V vs. $\text{Fc}^{+/0}$. (Figure 4.14) And while CPE studies under these conditions demonstrate successful suppression of hydrogen evolution ($\text{FE}_{\text{H}_2} = 4\%$), generation of methoxide by deprotonation of methanol convolutes product analysis. Though trace formate ($\text{FE} = 1\%$) and CO ($\text{FE} = 22\%$) are observed upon electrolysis work up, (Figures 4.13-15) methoxide is known to readily catalyze carbonylation of methanol to methyl formate in the presence of CO.²⁶ Therefore, due to the possibility of carbonylation activity and the degradation pathways of **1** discussed herein (*vide infra*), we refrain from assigning observed formate to be a result of hydride transfer to CO_2 .

However, the significant production of CO in the presence of phenol indicates reactivity of the Ni(0) state directly with CO_2 , which is typical of other systems such as $[\text{Ni}(\text{cyclam})]^{2+}$, which has been shown to bind CO_2 upon reduction of the nickel center followed by reductive

disproportionation to generate CO.²⁷ Indeed, cyclic voltammograms of **1** under CO₂ in the absence of a proton source result in a complete loss in reversibility of the Ni(II/0) couple with no observable increase in current. (Figure 4.6) This response is consistent with electron transfer to the catalyst followed by a chemical step (EC). In this system, the chemical step is believed to be irreversible binding of CO₂ to the electrochemically-generated, charge-neutral Ni(0) state.

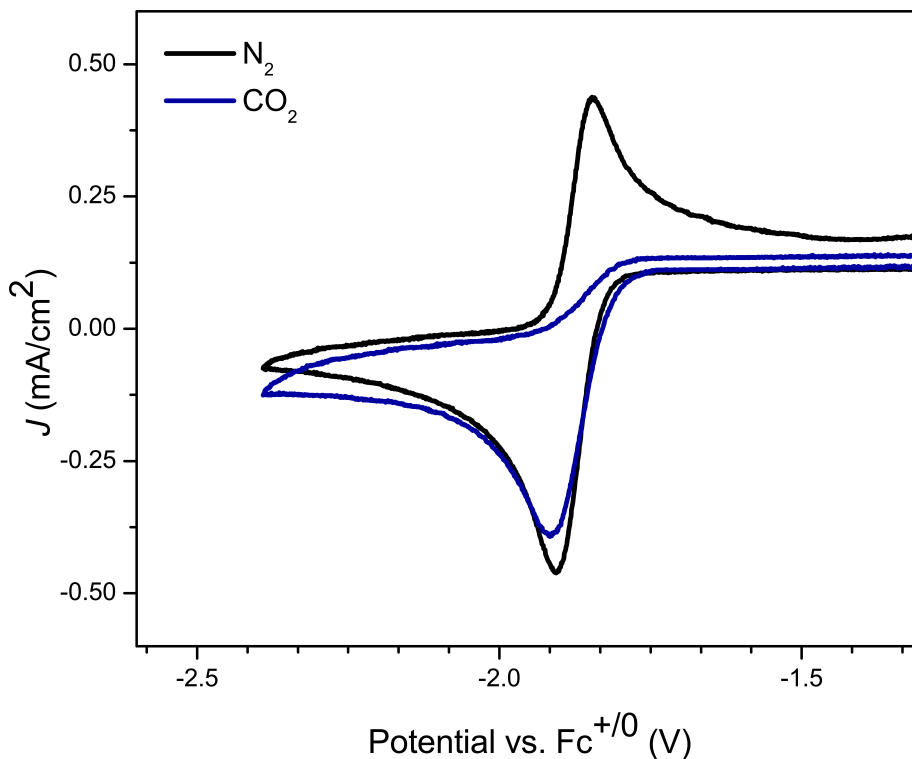


Figure 4.6: Cyclic voltammograms of **1** (1 mM) with no added proton source under nitrogen (black) and under CO₂ (blue). Conditions: 0.1 M Bu₄NPF₆ in acetonitrile at 100 mV s⁻¹; glassy carbon working electrode; platinum counter electrode; Ag/AgCl reference electrode.

4.2.3 Infrared Spectroelectrochemistry

Infrared spectroelectrochemical (IR-SEC) studies of this interaction indicate that upon reduction, **1** directly binds CO₂ to leading to the formation of a Ni(0) dicarbonyl species in both the presence and absence of an added proton source. In the absence of an added proton source, upon scanning to -1.8 V vs. a Ag pseudoreference electrode intense bands at 1951 and 1881

cm^{-1} are observed to grow in coinciding with the growth of an additional set of bands at 1686, 1648, and 1608 cm^{-1} .

We assign the bands at 1951 and 1881 cm^{-1} to the formation of a $[\text{Ni}(\text{bis-NHC})(\text{CO})_2]^0$ species, which is consistent with the A_1 and B_1 $\nu(\text{CO})$ modes in the expected C_{2v} geometry. This assignment is supported by previously reported Ni(0) dicarbonyl diphosphine complexes where the A_1 and B_1 $\nu(\text{CO})$ modes are observed in a similar vicinity.^{28–29} The bands at 1686, 1648, and 1608 cm^{-1} however, most likely correspond to formation of a bicarbonate species generated by disproportionation of the Ni(0)– CO_2 adduct resulting in bicarbonate and the nickel carbonyl species. These observations are analogous to previous studies when $[\text{Ni}(\text{cyclam})]^+$ is used as the catalyst.²⁷ Interestingly, formation of the nickel dicarbonyl species is still observed in the presence of phenol. (Figure 4.18) These findings suggest that binding of CO_2 to the Ni(0) state is a competitive pathway that persists, even in the presence of a proton source and supports the observation of significant poisoning under catalytic conditions.

When the identical experiment was performed with $^{13}\text{CO}_2$ (Figure 4.17), a redshift of 46 and 41 wavenumbers is observed for the higher and lower energy $\nu(\text{CO})$ modes, respectively. These findings are consistent with the expected isotopic shift for the generation of $[\text{Ni}(\text{bis-NHC})(^{13}\text{CO})_2]^0$. These findings are further supported by density functional theory (DFT) calculations. At the B3LYP level of theory, the DFT simulated FTIR spectrum of the $[\text{Ni}(\text{bis-NHC})(\text{CO})_2]^0$ (Figure 4.16), is in striking agreement with the experimental FTIR spectrum, with $\nu(\text{CO})$ modes at 1901 and 1838 cm^{-1} .

4.2.4 Computational Studies

Attempts to chemically isolate the doubly reduced state $\mathbf{1}^0$ and the hydride complex $\mathbf{1}^H$ were unsuccessful and we therefore employed DFT calculations to support their predicted geometries and qualitative molecular orbital structures. Calculations were carried out for complexes $\mathbf{1}$, $\mathbf{1}^0$, and $\mathbf{1}^H$ using Restricted Kohn-Sham (RKS) calculations in the ORCA software suite (version

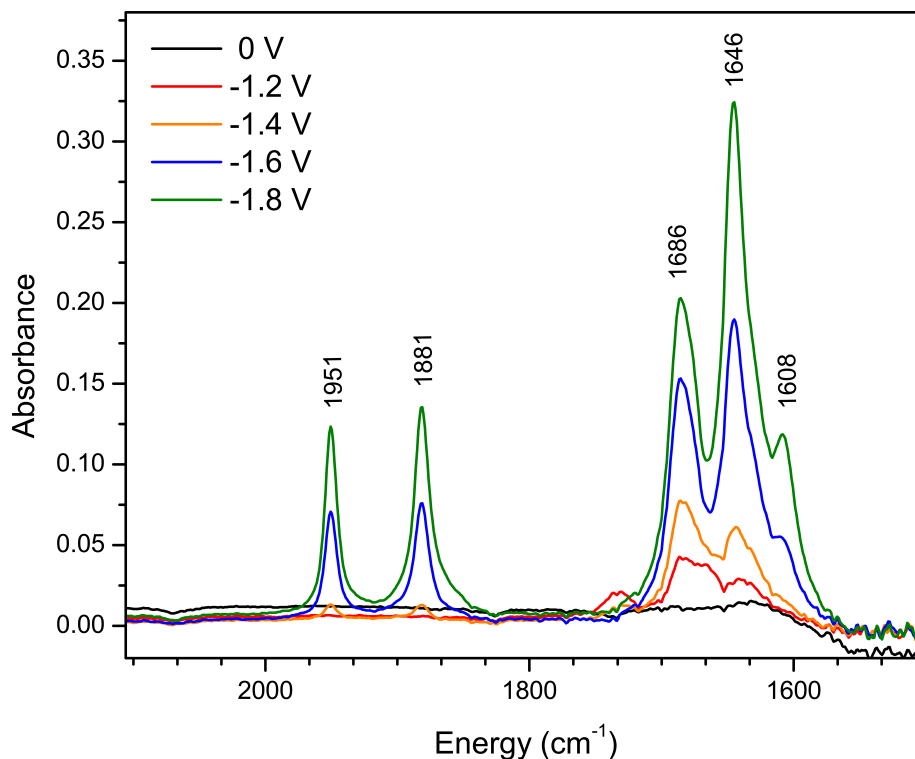


Figure 4.7: IR-SEC of **1** (3 mM) in CO₂-saturated acetonitrile in the absence of an added proton source, sweeping from 0 to -1.8 V vs. Ag pseudoreference electrode. Conditions: glassy carbon working electrode; platinum counter electrode; silver pseudoreference electrode; 0.1 M tetrabutylammonium hexafluorophosphate supporting electrolyte.

3.0.3) at the B3LYP level of theory. Further details on computational studies including input files and optimized coordinates are provided in Appendix C.

We previously reported the structural characterization of **1** and the phenyl-substituted analogues of both **1** and **1**⁰, [Ni(bis-NHC)(dppe)]²⁺ and [Ni(bis-NHC)(dppe)]⁰, respectively (dppe = 1,2-bis(diphenylphosphino)ethane).²⁰ The optimized structure of **1** shows the expected square planar geometry and is in close agreement with the solid state bond lengths (Table 4.1). The doubly reduced state, **1**⁰, is consistent with a tetrahedral Ni(0) d¹⁰ complex, which exhibits mild lengthening of 0.04 Å at the Ni-C bonds, and closely matches the crystallographic bond distances of the analogous tetrahedral [Ni(bis-NHC)(dppe)]⁰ crystal structure.

However, most notable is the optimized geometry and molecular orbital structure of **1**^H, which adopts a pseudo-trigonal bipyramidal geometry. The optimized structure provides

Table 4.1: Selected calculated and experimental bond lengths.

Bond	Complex					
	Calculated Bond Length (Å)			Crystallographic Bond Length (Å) ²⁰		
	1	1⁰	1^H	1	[Ni(bis–NHC)(dppe)] ²⁺	[Ni(bis–NHC)(dppe)] ⁰
Ni-P1	2.20	2.20	2.17	2.1859(14)	2.2196(7)	2.1642(9)
Ni-P2	2.20	2.20	2.53	2.1710(14)	2.2063(7)	2.1643(8)
Ni-C1	1.92	1.96	1.91	1.900(4)	1.894(3)	1.921(3)
Ni-C2	1.92	1.96	1.94	1.899(5)	1.900(2)	1.914(3)
Ni-H	-	-	1.49	-	-	-

direct insight into the observed instability of these species, displaying clear labilization of the phosphine ligand. The distorted 5-coordinate geometry exhibits significant lengthening of the Ni-P2 bond length from 2.20 Å in **1** and **1⁰** to 2.53 Å in the calculated **1^H** structure. Investigation of the frontier orbital structure of this species reveals that the HOMO is antibonding in nature with respect to one of the phosphorus atoms of the dmpe ligand. The interaction consists of a d_{z^2} , nickel-based orbital in combination with an out-of-phase colinear phosphine σ orbital with calculated Mulliken reduced orbital populations of 47.0% at the nickel and 20.8% at the phosphorus. We postulate that this antibonding HOMO interaction results in instability of the 5-coordinate hydride species *via* labilization of the phosphine chelate, which yields susceptibility of attack at that position, leading to dissociation of the phosphine chelate.

4.2.5 Proposed Mechanism

Given these electrocatalytic and spectroscopic studies, we propose a series of divergent mechanistic pathways depicted in Figure 4.8. All three possible pathways are initiated by the two-electron reduction of **1** to afford **1⁰**. Upon formation of **1⁰**, either direct interaction with CO₂ or protonation to form the proposed Ni(II) hydride **1^H** can occur. Protonation of **1^H** by a second equivalent of acid yields molecular hydrogen, regenerating **1**. Interestingly however, density function theory (DFT) studies indicate that **1^H** may be susceptible to phosphine labilization

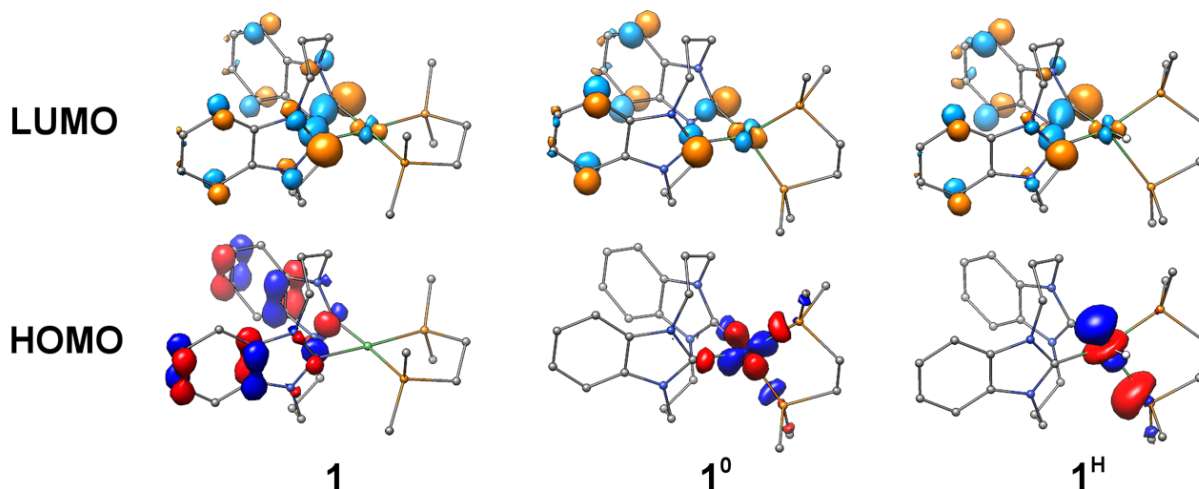


Figure 4.8: DFT-calculated HOMOs and LUMOs of complexes **1**, **1⁰**, and **1^H**. Hydrogen atoms are omitted for clarity with the exception of the hydride of **1^H**.

(*vide supra*). However, near ideal, S-shaped catalytic responses observed in cyclic voltammetry experiments of **1** in the presence of phenol and stable current densities through several catalyst turnovers for HER in previous studies suggest that hydride protonation is fast with respect to hypothesized phosphine loss.²⁰

While the hydricity of **1^H** was experimentally benchmarked to be less than 40.6 kcal mol⁻¹, which establishes hydride transfer to CO₂ to be exergonic by at least 3.4 kcal mol⁻¹, no significant formate was observed in controlled potential electrolysis experiments. Hydride transfer kinetics are generally quite slow at first row transition metals,^{30–32} and we therefore postulate that fast protonation and instability of **1^H** preclude interaction of this species with CO₂ under catalytic conditions.

However, **1⁰** readily reacts with CO₂ in both the presence and absence of an added proton source. Detection of CO as a reduction product in controlled potential electrolysis and spectroscopic observation of bicarbonate formation via IR-SEC experiments indicate a reductive

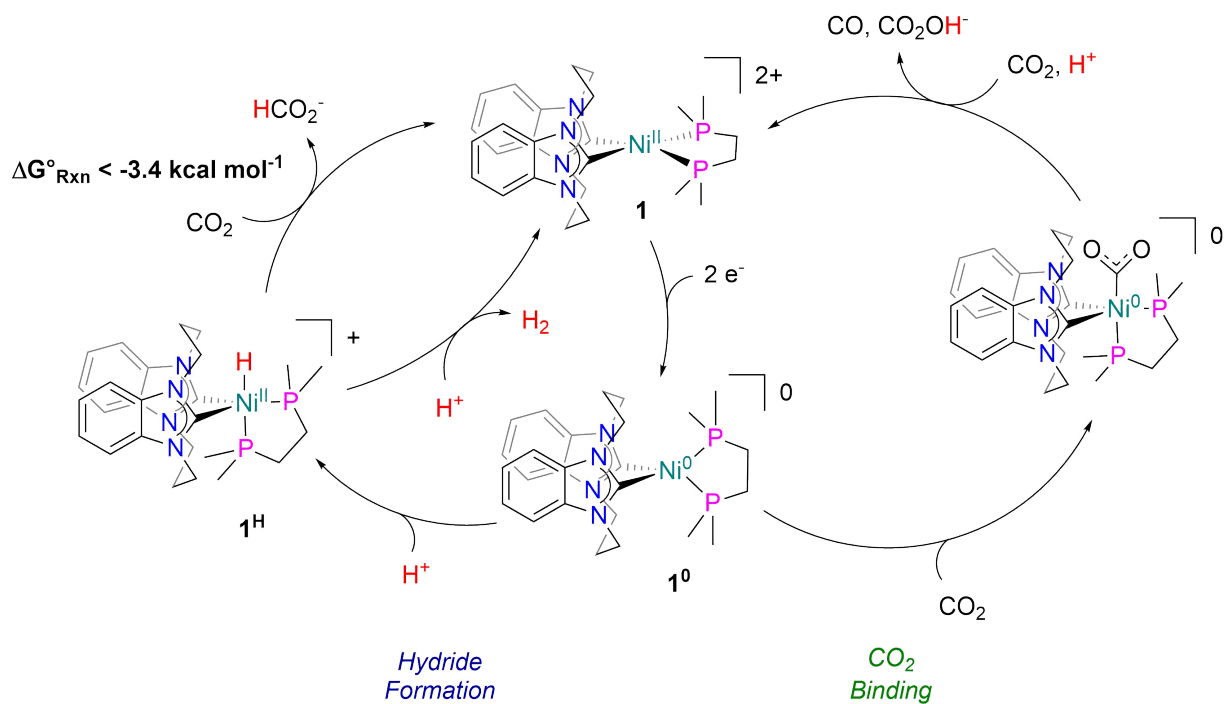


Figure 4.9: Proposed mechanistic pathways of CO₂ reduction and hydrogen evolution by **1**.

disproportionation pathway, which is well established for [Ni(cyclam)]²⁺ catalysts.²⁷ However, **1** suffers greatly from instability through this pathway as the CO-poisoned, dicarbonyl degradation product is observed by IR-SEC under an atmosphere of CO₂ at potentials negative of the Ni(II/0) couple both in the presence and absence of added acid.

4.2.6 Insights for Future Catalyst Design

Directing selective electrocatalysis requires finely balancing catalyst intermediate reactivities, which becomes particularly convoluted when multiple substrates are required. Our focus over the course of these recent studies was to target strong hydricities at nickel to select for thermodynamically favorable hydride transfer to CO₂. However, tuning pre-catalyst redox couples to such negative potentials in the pursuit of such reactive hydrides results in the generation of particularly electron-rich reduced states. In this case, the electrochemically-generated Ni(0)

state becomes extremely nucleophilic, yielding direct binding of CO₂ to undergo reduction to CO in addition to deleterious catalyst poisoning.

This underscores the give-and-take nature of scaling relationships: the highly electron-rich catalyst sites required to access reactive hydride intermediates can in turn produce divergent substrate reactivity and instability. In the case of **1**, stability issues may be remedied by the utilization of new ligand frameworks. While the bis-NHC ligand described herein successfully pushes reduction potentials at nickel to highly negative potentials, the instability of **1^H**, may be a product of the orthogonal chelation geometry of this ligand, which we have shown previously to be quite rigid and pinched in comparison to typical 5-membered chelation motifs. However, even if greater stability of the hydride is achieved, the propensity for CO₂ binding at the reduced state of the catalyst would likely persist. Therefore, kinetic tuning to favor hydride formation over direct interaction with CO₂ through the installation of proton shuttles such as the well-studied P₂N₂ ligand family may represent a fruitful approach to improving pathway selectivity.

However, a more elegant goal to develop new hydride transfer catalysts for CO₂ reduction would be to diverge from the hydricity scaling relationship altogether. Inspection of eq 8, which describes hydricity as a function of $E_{1/2}(M^{n+/(n-1)+})$, shows that ΔG_{H-}° is also dependent on the bond dissociation free energy of the metal hydride bond. This term varies relatively little across most transition metal hydride complexes, which accounts for the strong fit in this relationship. This is even more notable in the same relationship for organic hydride donors, wherein there exists less variation in BDFE, resulting in still better fit.¹⁷ Carbon-hydrogen bonds are on average ~ 20 kcal mol⁻¹ stronger than metal-hydride bonds and the linear hydricity relationship is subsequently translated vertically to hydricities that are approximately ~ 20 kcal mol⁻¹ weaker, given the same corresponding redox potential. Moving in the opposite direction by selecting for weaker hydride BDFE's in new systems while simultaneously tuning $E_{1/2}(M^{n+/(n-1)+})$ may prove to be a more desirable approach to targeting hydridic hydrides. Less electron-rich metal centers with weaker M-H bonds could produce similarly hydridic hydrides while avoiding nucleophilic intermediates

capable of direct interaction with CO₂ and providing the added benefit of less negative operating potentials.

4.3 Conclusion

Targeting catalysts for efficient and selective electrocatalytic reduction of CO₂ marks an important goal to improve fundamental mechanistic understanding of such catalytic processes. Homing in on the thermodynamic parameters governing hydride reactivity of catalyst intermediates with CO₂, we have established a route to electronically tune first-row hydrides to regimes capable of CO₂ reduction. However, we find that despite accessing unprecedented hydricities, desired reactivity is circumvented by divergent mechanistic pathways. This not only underscores both the utility and limitation of thermodynamic scaling relationships in catalyst design, but also provides insight on the manner in which future design strategies may be steered to break from such relationships.

4.4 Experimental

General Considerations

All reactions were carried out under a nitrogen atmosphere using standard Schlenk and glovebox techniques. Solvents were sparged with argon, dried on a custom dry solvent system over alumina columns, and stored over molecular sieves before use. All reagents were obtained from commercial suppliers and used without further purification unless otherwise noted. Tetrabutylammonium hexafluorophosphate (TBAPF₆, Aldrich, 98%) was twice recrystallized from methanol and dried under a vacuum at 90°C overnight before use. **1** was prepared according to a previously-reported procedure.²⁰

Instrumentation

^1H NMR spectra were recorded on a Bruker 300 MHz spectrometer. ^1H NMR chemical shifts are reported relative to TMS ($\sigma = 0$) and referenced against residual solvent proton peaks.

Electrochemical experiments were performed in 0.1 M tetra-*n*-butylammonium hexafluorophosphate solution in acetonitrile using a Gamry Reference 600 potentiostat. A single-compartment cell was used for cyclic voltammetry experiments with a glassy carbon working electrode (3 mm in diameter, Bioanalytical Systems, Inc.), Pt wire counter electrode, and Ag/AgCl pseudo-reference electrode. All potentials are referenced to the $\text{Fc}^{+/0}$ couple using ferrocene as an internal reference. Controlled potential electrolysis experiments were carried out in a custom 90 mL cell designed in our laboratory. The setup included a glassy carbon working electrode, graphite rod counter electrode separated from the solution by a porous glass frit, and Ag/AgCl pseudo-reference electrode separated from the solution by a Vycor tip. For the catalytic electrolysis studies, the cell was charged with nickel catalyst (1 mM) and phenol (0.1 M) in 0.1 M tetra-*n*-butylammonium hexafluorophosphate solution in acetonitrile. Hydrogen and CO were quantified by analyzing 1 mL aliquots of the headspace on a Hewlett-Packard 7890A Series gas chromatograph with two molsieve columns (30 m x 0.53 mm ID x 25 μm film). The partial pressure of H_2 and CO in the headspace was determined by comparison to gas standard samples.

Restricted Kohn-Sham (RKS) calculations were performed in the ORCA software suite (version 3.0.3) using the B3LYP functional with the RIJCOSX approximation. All carbon, hydrogen and nitrogen atoms were treated with Ahlrichs DEF2-SVP/J basis set while Ahlrichs DEF2-TZVP/J basis set was used for nickel and phosphorus. Dispersion corrections were applied using the Becke-Johnson damping scheme (D3BJ) and solvation was accounted for using the COSMO solvation model in acetonitrile.

Acknowledgements

Chapter 4, in full, is being prepared for submission for publication of the material entitled, Ostericher, A. L.; Porter, T. M.; Kubiak, C. P., "Thermodynamic Targeting of Electrocatalytic CO₂ Reduction: Advantages, Limitations, and Insights for Catalyst Desing." The dissertation author was the primary author of this material. This work was supported by the Joint Center for Artificial Photosynthesis, a DOE Energy Innovation Hub, supported through the Office of Science of the U.S. Department of Energy under Award No. DE-SC0004993.

4.5 References

1. Senftle, T. P.; Carter, E. A., The Holy Grail: Chemistry Enabling an Economically Viable CO₂ Capture, Utilization, and Storage Strategy. *Acc. Chem. Res.* **2017**, *50* (3), 472-475.
2. Armstrong, R. C.; Wolfram, C.; de Jong, K. P.; Gross, R.; Lewis, N. S.; Boardman, B.; Ragauskas, A. J.; Ehrhardt-Martinez, K.; Crabtree, G.; Ramana, M. V., The frontiers of energy. *Nat. Energy* **2016**, *1* (1), 15020.
3. Lewis, N. S., Research opportunities to advance solar energy utilization. *Science* **2016**, *351* (6271), aad1920.
4. Benson, E. E.; Kubiak, C. P.; Sathrum, A. J.; Smieja, J. M., Electrocatalytic and homogeneous approaches to conversion of CO₂ to liquid fuels. *Chem Soc Rev* **2009**, *38* (1), 89-99.
5. De Luna, P.; Hahn, C.; Higgins, D.; Jaffer, S. A.; Jaramillo, T. F.; Sargent, E. H., What would it take for renewably powered electrosynthesis to displace petrochemical processes? *Science* **2019**, *364* (6438), eaav3506.
6. Waldie, K. M.; Brunner, F. M.; Kubiak, C. P., Transition Metal Hydride Catalysts for Sustainable Interconversion of CO₂ and Formate: Thermodynamic and Mechanistic Considerations. *ACS Sustainable Chemistry & Engineering* **2018**.
7. Lilio, A. M.; Reineke, M. H.; Moore, C. E.; Rheingold, A. L.; Takase, M. K.; Kubiak, C. P., Incorporation of Pendant Bases into Rh(diphosphine)₂ Complexes: Synthesis, Thermodynamic Studies, And Catalytic CO₂ Hydrogenation Activity of [Rh(P₂N₂)₂]⁺ Complexes. *J. Am. Chem. Soc.* **2015**, *137* (25), 8251-60.
8. Berning, D. E.; Noll, B. C.; DuBois, D. L., Relative Hydride, Proton, and Hydrogen Atom Transfer Abilities of [HM(diphosphine)₂]PF₆ Complexes (M = Pt, Ni). *J. Am. Chem. Soc.* **1999**, *121* (49), 11432-11447.
9. Curtis, C. J.; Miedaner, A.; Raebiger, J. W.; DuBois, D. L., Periodic Trends in Metal Hydride Donor Thermodynamics: Measurement and Comparison of the Hydride Donor Abilities of the Series HM(PNP)²⁺ (M = Ni, Pd, Pt; PNP = Et₂PCH₂N(Me)CH₂PEt₂). *Organometallics* **2004**, *23* (3), 511-516.
10. Wiedner, E. S.; Chambers, M. B.; Pitman, C. L.; Bullock, R. M.; Miller, A. J.; Appel, A. M., Thermodynamic Hydricity of Transition Metal Hydrides. *Chem Rev* **2016**, *116* (15), 8655-92.
11. Galan, B. R.; Wiedner, E. S.; Helm, M. L.; Linehan, J. C.; Appel, A. M., Effects of Phosphine–Carbene Substitutions on the Electrochemical and Thermodynamic Properties of Nickel Complexes. *Organometallics* **2014**, *33* (9), 2287-2294.

12. DuBois, D. L.; Berning, D. E., Hydricity of transition-metal hydrides and its role in CO₂ reduction. *Applied Organometallic Chemistry* **2000**, *14* (12), 860-862.
13. Barlow, J. M.; Yang, J. Y., Thermodynamic Considerations for Optimizing Selective CO₂ Reduction by Molecular Catalysts. *ACS Central Science* **2019**, *5* (4), 580-588.
14. Ceballos, B. M.; Yang, J. Y., Directing the reactivity of metal hydrides for selective CO₂ reduction. *Proceedings of the National Academy of Sciences* **2018**, *115* (50), 12686-12691.
15. Tsay, C.; Livesay, B. N.; Ruelas, S.; Yang, J. Y., Solvation Effects on Transition Metal Hydricity. *J. Am. Chem. Soc.* **2015**, *137* (44), 14114-14121.
16. Berning, D. E.; Miedaner, A.; Curtis, C. J.; Noll, B. C.; Rakowski DuBois, M. C.; DuBois, D. L., Free-Energy Relationships between the Proton and Hydride Donor Abilities of [HNi(diphosphine)₂]⁺ Complexes and the Half-Wave Potentials of Their Conjugate Bases. *Organometallics* **2001**, *20* (9), 1832-1839.
17. Waldie, K. M.; Ostericher, A. L.; Reineke, M. H.; Sasayama, A. F.; Kubiak, C. P., Hydricity of Transition-Metal Hydrides: Thermodynamic Considerations for CO₂ Reduction. *ACS Catal.* **2018**, *8* (2), 1313-1324.
18. Reineke, M. H.; Sampson, M. D.; Rheingold, A. L.; Kubiak, C. P., Synthesis and Structural Studies of Nickel(0) Tetracarbene Complexes with the Introduction of a New Four-Coordinate Geometric Index, τ_8 . *Inorg. Chem.* **2015**, *54* (7), 3211-3217.
19. Reineke, M. H.; Porter, T. M.; Ostericher, A. L.; Kubiak, C. P., Synthesis and Characterization of Heteroleptic Ni(II) Bipyridine Complexes Bearing Bis(N-heterocyclic carbene) Ligands. *Organometallics* **2018**, *37* (3), 448-453.
20. Ostericher, A. L.; Waldie, K. M.; Kubiak, C. P., Utilization of Thermodynamic Scaling Relationships in Hydricity To Develop Nickel Hydrogen Evolution Reaction Electrocatalysts with Weak Acids and Low Overpotentials. *ACS Catal.* **2018**, *8* (10), 9596-9603.
21. Curtis, C. J.; Miedaner, A.; Ellis, W. W.; DuBois, D. L., Measurement of the Hydride Donor Abilities of [HM(diphosphine)₂]⁺ Complexes (M = Ni, Pt) by Heterolytic Activation of Hydrogen. *J. Am. Chem. Soc.* **2002**, *124* (9), 1918-1925.
22. Faulkner, A. J. B. a. L. R., *Electrochemical Methods*. Wiley: New York, 1980.
23. Costentin, C.; Robert, M.; Savéant, J.-M., Catalysis of the electrochemical reduction of carbon dioxide. *Chemical Society Reviews* **2013**, *42* (6), 2423-2436.
24. Costentin, C.; Drouet, S.; Robert, M.; Savéant, J.-M., Turnover Numbers, Turnover Frequencies, and Overpotential in Molecular Catalysis of Electrochemical Reactions. Cyclic

- Voltammetry and Preparative-Scale Electrolysis. *J. Am. Chem. Soc.* **2012**, *134* (27), 11235-11242.
25. Bhugun, I.; Saveant, J. M., Self-inhibition in catalytic processes: cyclic voltammetry. *J. Electroanal. Chem.* **1996**, *408* (1), 5-14.
26. Reutemann, W. a. K., H., Formic Acid. In *Ullmann's Encyclopedia of Industrial Chemistry*, 2000.
27. Froehlich, J. D.; Kubiak, C. P., The homogeneous reduction of CO(2) by [Ni(cyclam)]⁺: increased catalytic rates with the addition of a CO scavenger. *J Am Chem Soc* **2015**, *137* (10), 3565-73.
28. Chatt, J.; Hart, F. A., 276. Reactions of tertiary diphosphines with nickel and nickel carbonyl. *Journal of the Chemical Society (Resumed)* **1960**, (0), 1378-1389.
29. Flener Lovitt, C.; Frenking, G.; Girolami, G. S., Donor–Acceptor Properties of Bidentate Phosphines. DFT Study of Nickel Carbonyls and Molecular Dihydrogen Complexes. *Organometallics* **2012**, *31* (11), 4122-4132.
30. Cheng, T.-Y.; Bullock, R. M., Kinetic hydricity of transition-metal hydrides toward trityl cation. *Organometallics* **1995**, *14* (9), 4031-4033.
31. Cheng, T.-Y.; Brunshwig, B. S.; Bullock, R. M., Hydride Transfer Reactions of Transition Metal Hydrides: Kinetic Hydricity of Metal Carbonyl Hydrides. *J. Am. Chem. Soc.* **1998**, *120* (50), 13121-13137.
32. Cheng, T.-Y.; Bullock, R. M., Hydride Transfer from (η^5 -C₅Me₅)(CO)₂MH (M = Fe, Ru, Os) to Trityl Cation: Different Products from Different Metals and the Kinetics of Hydride Transfer. *Organometallics* **2002**, *21* (11), 2325-2331.

4.6 Appendix C

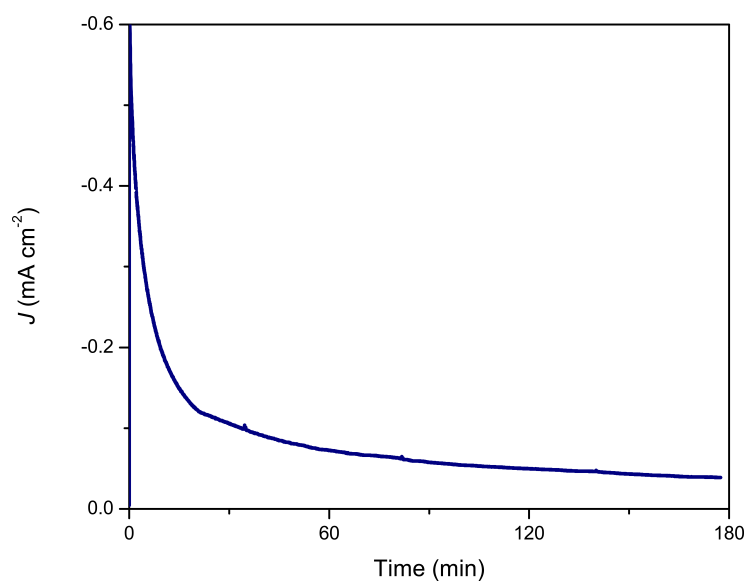


Figure 4.10: Controlled potential electrolysis at -1.75 V vs. Ag/AgCl in the presence of **1** under CO₂. Conditions: 0.1 M TBAPF₆ in acetonitrile with 0.1 M phenol, glassy carbon working electrode, graphite rod counter electrode, Ag/AgCl reference electrode.

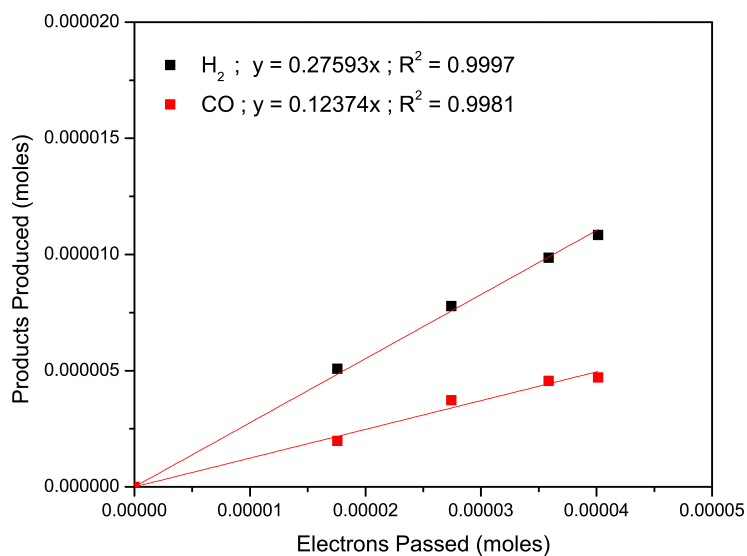


Figure 4.11: Plot of charge passed vs. gas products produced during controlled potential electrolysis shown in Figure 4.11. Slopes of 0.27593 and 0.12374 for the 2-electron products of H₂ and CO correspond to Faradaic Efficiencies of 55% and 25%, respectively.

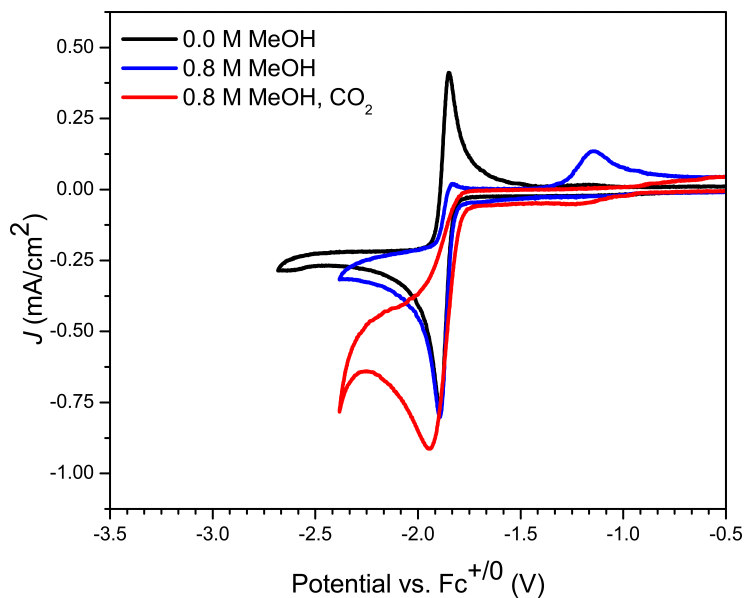


Figure 4.12: Cyclic voltammograms of **1** (1 mM) under nitrogen with no added proton source (black), with 0.8 M methanol under nitrogen (blue), and 0.8 M methanol under CO₂ (red). Conditions: 0.1 M Bu₄NPF₆ in acetonitrile at 100 mV s⁻¹; glassy carbon working electrode; platinum counter electrode; Ag/AgCl reference electrode.

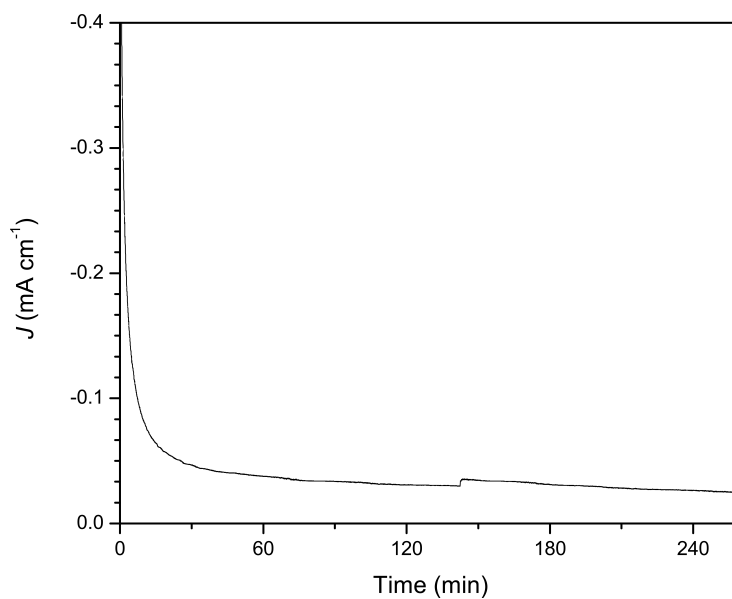


Figure 4.13: Controlled potential electrolysis at -1.75 V vs. Ag/AgCl in the presence of **1** under CO₂. Conditions: 0.1 M TBAPF₆ in acetonitrile with 0.4 M methanol, glassy carbon working electrode, graphite rod counter electrode, Ag/AgCl reference electrode.

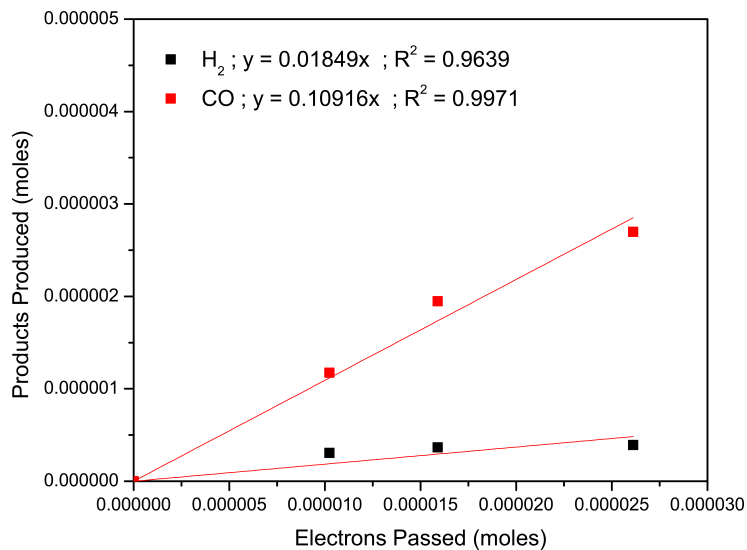


Figure 4.14: Plot of charge passed vs. gas products produced during controlled potential electrolysis shown in Figure 4.13. Slopes of 0.01849 and 0.10916 for the 2-electron products of H₂ and CO correspond to Faradaic Efficiencies of 4% and 22%, respectively.

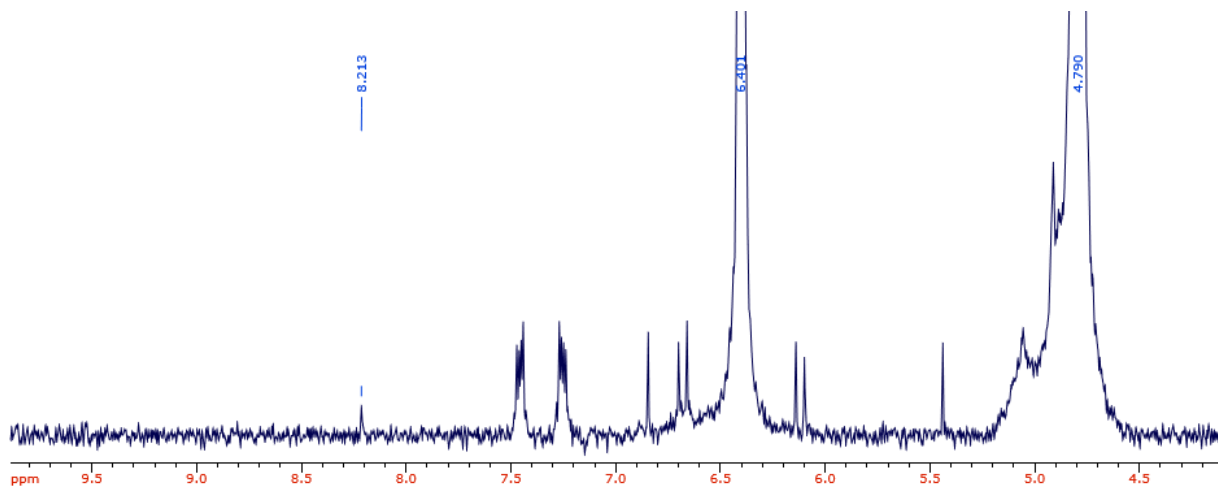


Figure 4.15: ¹H NMR of bulk work-up of CPE from Figure 4.13 in D₂O, showing formate resonance at 8.21 ppm and maleic acid internal standard at 6.40 ppm. Identical workup of control CPE under the same conditions save for the absence of 1 was void of a formate resonance.

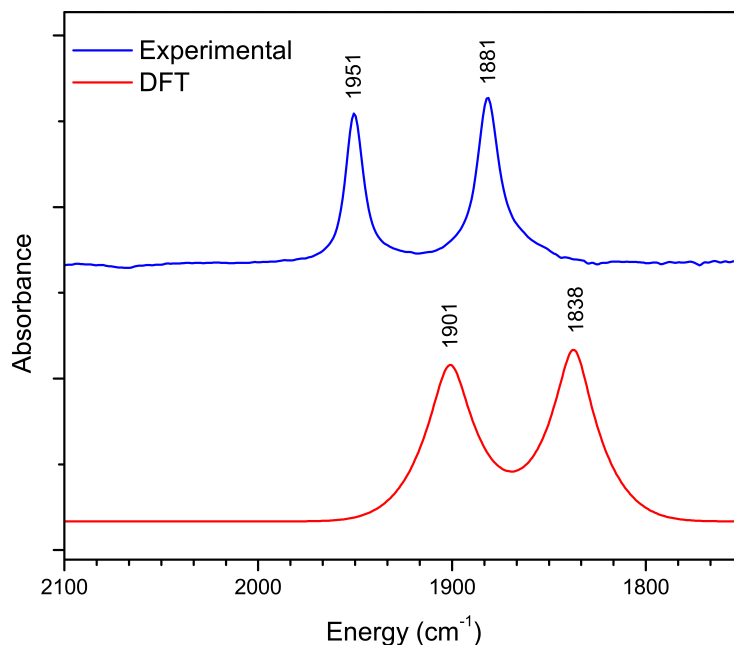


Figure 4.16: Experimental (blue) and DFT-calculated (red) FTIR spectra of the carbonyl stretches of the proposed degradation species $[\text{Ni}(\text{bis-NHC})(\text{CO})_2]^0$. For details on optimized structure used for calculations and input files, see Computational Methods section below.

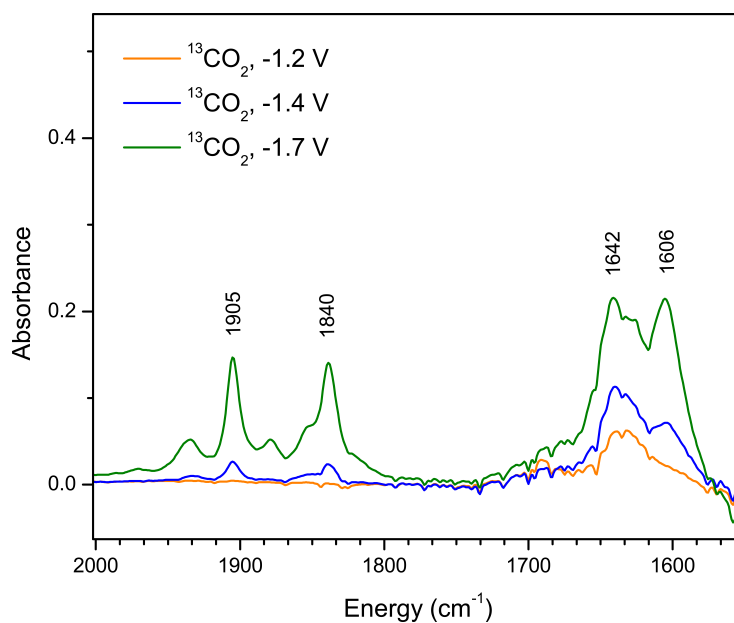


Figure 4.17: IR-SEC of **1** (3 mM) in $^{13}\text{CO}_2$ -saturated acetonitrile in the absence of an added proton source, sweeping from -1.2 to -1.7 V vs. Ag pseudoreference electrode. Conditions: glassy carbon working electrode; platinum counter electrode; silver pseudoreference electrode; 0.1 M tetrabutylammonium hexafluorophosphate supporting electrolyte.

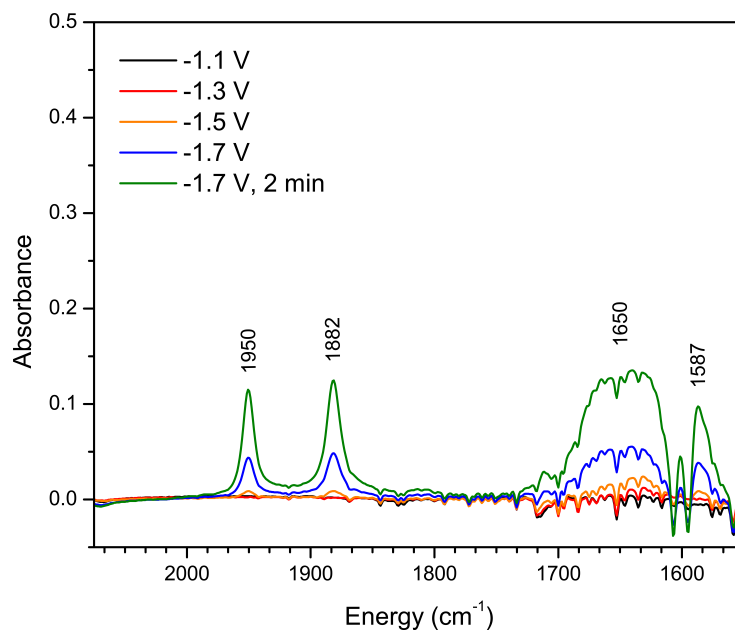


Figure 4.18: IR-SEC of **1** (3 mM) in CO₂-saturated acetonitrile in the presence of phenol (0.1 M), sweeping from -1.1 to -1.8 V vs. Ag pseudoreference electrode. Conditions: glassy carbon working electrode; platinum counter electrode; silver pseudoreference electrode; 0.1 M tetrabutylammonium hexafluorophosphate supporting electrolyte.

Computational Details

Density Functional Theory Analysis. Calculations were performed in the ORCA software suite (version 3.0.3) at the B3LYP level of theory with the RIJCOSX approximation.^{1–5} Nickel and phosphorous atoms were treated with the DEF2-TZVP basis sets while DEF2-SVP was used for all other atoms.^{6–14} Dispersion corrections were applied using the atom-pairwise dispersion correction with a Becke-Johnson damping scheme (D3BJ), while solvation was accounted for using the COSMO solvation model in acetonitrile.^{17–19} Analytical frequency calculations were performed at the same level of theory to ensure all optimized structures were minima. Molecular graphics were constructed with the UCSF Chimera package.²⁰

Representative input file:

```
%pal nprocs 8 end
! RKS B3LYP/G RIJCOSX D3BJ def2-SVP def2-SVP/J
! COSMO(Acetonitrile) SlowConv GRIDX5 FinalGrid6 VeryTightSCF opt
%basis
newgto Ni "def2-TZVP" end
newgto P "def2-TZVP" end
end
%SCF
MaxIter 2000
end
* xyz "Charge" "Multiplicity"
"XYZ Coordinates"
*
```

Table 4.2: Optimized geometry coordinates for complex **1**.

Atom	X	Y	Z
Ni	4.97707778	8.40393549	21.1819899
P	5.11146001	8.24230151	23.3727802
P	4.72682809	10.5719634	21.4589486
N	3.78649624	8.15910268	18.5226092
N	5.95504704	8.38351775	18.4328389
N	4.14397913	5.67407972	20.5751104
C	4.63057078	4.48842091	20.0169429
N	6.31233968	5.89671774	20.4782489
C	5.16668374	6.52348727	20.8400985
C	6.02914044	4.63207297	19.9533793
C	4.14734712	7.90446513	17.1960975
C	3.61431425	7.52351375	24.1029398
H	2.72826234	8.08634822	23.7782275
H	3.6819742	7.55209834	25.2005726
H	3.51503741	6.47986302	23.7744312
C	3.3983534	7.56564175	16.0674815
H	2.31475844	7.44708599	16.1086992
C	6.48668504	7.28868343	24.0619961
H	6.41748076	6.24734443	23.718364
H	6.44969969	7.31186786	25.1613009
H	7.44088408	7.7149659	23.7228788
C	5.54597852	8.0510361	17.13789
C	4.80831397	2.32078403	19.0536834

H	4.34934172	1.39931432	18.6896665
C	7.34996808	8.50959993	18.8556068
H	7.37088324	9.16867522	19.7341824
H	7.89209692	9.02521016	18.0511206
C	2.07871234	6.55147213	19.4316854
H	0.98944351	6.52469009	19.5887468
H	2.28717256	5.87913539	18.5836735
C	2.72558306	6.00522652	20.7089924
H	2.63127499	6.73386026	21.5254513
H	2.20370868	5.09293174	21.0276646
C	5.50522235	7.52565369	14.8187415
H	6.01882089	7.36604231	13.8684285
C	7.63834518	6.51290983	20.4917451
H	8.36280677	5.72837138	20.7480543
H	7.65172194	7.24641486	21.3104224
C	8.03931146	7.17910159	19.1720387
H	9.11877943	7.38577777	19.2355161
H	7.90695993	6.47334244	18.3357395
C	2.43731483	7.99417387	19.0616385
H	1.73304121	8.36993608	18.3071096
H	2.35115154	8.64933114	19.9393635
C	6.84650666	3.62392451	19.4386365
H	7.930708	3.73157962	19.3835491
C	6.2529592	7.86866043	15.9479193
H	7.33661576	7.98288811	15.8971644

C	4.88608576	8.43514064	19.2645612
C	6.24766081	11.4851131	21.0772453
H	7.0898825	11.0755512	21.6510718
H	6.12066341	12.5488967	21.3271196
H	6.46763048	11.3900238	20.0049462
C	3.41784259	11.4038758	20.5269719
H	3.60222391	11.2835	19.4500607
H	3.39904098	12.4751828	20.7760892
H	2.44452357	10.9591096	20.7762902
C	4.10525909	7.37613362	14.8776231
H	3.55959791	7.10310157	13.972294
C	5.24603449	9.93429628	24.0723948
H	4.95232777	9.93389463	25.1324475
H	6.30849537	10.22012	24.0256954
C	3.99200654	3.32920902	19.5716329
H	2.90823208	3.21281209	19.6183572
C	6.20867449	2.46560451	18.9879593
H	6.80979211	1.65356904	18.5737611
C	4.3863018	10.8840831	23.2347119
H	4.57217283	11.9401604	23.4800896
H	3.31394905	10.6914811	23.3969502

Table 4.3: Optimized geometry coordinates for complex **1⁰**.

Atom	X	Y	Z
Ni	4.95745898	8.39721725	21.251133
P	3.35589443	9.4195295	22.3559524
P	6.4370423	9.35396602	22.5742975
N	3.81529631	8.07376176	18.5118471
N	5.98164367	8.29774121	18.4468967
N	4.12389949	5.63382117	20.4840434
C	4.59999967	4.55725395	19.7466026
N	6.29039018	5.85855655	20.4217565
C	5.14306624	6.4778652	20.8979814
C	6.00290208	4.7028629	19.7062487
C	4.20788259	7.64949679	17.2483944
C	2.64352089	10.943032	21.5817948
H	3.47267785	11.5735323	21.2300682
H	2.01309619	11.5205638	22.2789535
H	2.0408304	10.6643266	20.7042942
C	3.4963338	7.16371997	16.1500455
H	2.41227816	7.04056183	16.180045
C	1.80602981	8.74161605	23.1091354
H	1.12986312	8.40013067	22.310711
H	1.27167611	9.48556923	23.7245268
H	2.06186547	7.87362511	23.7353614
C	5.61044126	7.79596599	17.2055622
C	4.77340239	2.55347811	18.4532243

H	4.3058028	1.70125558	17.9539469
C	7.3637685	8.46036932	18.8656578
H	7.3461101	9.12596889	19.7371363
H	7.9131825	8.96338317	18.0535049
C	2.04496212	6.52013142	19.3907046
H	0.95716618	6.53100862	19.5720255
H	2.20727564	5.84448837	18.5345215
C	2.71126089	5.93406184	20.6432234
H	2.63733036	6.63894836	21.4805671
H	2.19067714	5.00428517	20.9237853
C	5.62505263	6.98017712	14.9579361
H	6.16631269	6.70855479	14.0482966
C	7.62066583	6.44073198	20.4941558
H	8.33415307	5.63777711	20.7381917
H	7.60446236	7.15274281	21.3276792
C	8.07768059	7.14693562	19.2108576
H	9.14968712	7.37708208	19.3302006
H	8.00711679	6.45093749	18.3578758
C	2.45355813	7.94803911	19.0060237
H	1.77001414	8.32003178	18.2260553
H	2.37460554	8.60940197	19.8757991
C	6.80835841	3.77878306	19.0390362
H	7.89345475	3.89006437	18.9992727
C	6.33991776	7.46677633	16.0621964
H	7.4250538	7.57753829	16.0250482

C	4.89562328	8.46008291	19.2923689
C	7.12369019	8.33674461	23.9605726
H	6.28923055	7.83887704	24.4759856
H	7.69526001	8.93813197	24.6877718
H	7.77985815	7.55145589	23.5553612
C	7.96520639	10.311206	22.1524096
H	8.71266791	9.63578582	21.7082085
H	8.41545541	10.7968383	23.0343488
H	7.71381185	11.0799019	21.4059916
C	4.22912312	6.83076438	15.0016034
H	3.70244998	6.44450806	14.125523
C	4.12214383	10.173088	23.8790836
H	3.49048476	10.9821451	24.2841537
H	4.15738236	9.3712972	24.6358228
C	3.9641943	3.48269445	19.1229
H	2.87889796	3.36783234	19.1477651
C	6.16977104	2.69906227	18.4117713
H	6.77184313	1.95842167	17.8795265
C	5.53710719	10.6565968	23.5563328
H	6.09951561	10.9288072	24.4656576
H	5.49749178	11.5519894	22.9139774

Table 4.4: Optimized geometry coordinates for complex **1^H**.

Atom	X	Y	Z
Ni	4.90001326	8.20598014	21.2126126
P	3.75563287	9.94589505	21.8323588
P	6.87846636	9.37175224	22.2800915
N	3.71506885	7.96684746	18.5635187
N	5.86245689	8.27490475	18.3864369
N	4.23855841	5.47930557	20.5399182
C	4.73189685	4.34198548	19.901465
N	6.38393315	5.79224697	20.330019
C	5.23824791	6.37273927	20.7901114
C	6.11800926	4.5434154	19.765836
C	4.03199267	7.70644361	17.2303674
C	3.50031766	11.2422543	20.5718314
H	4.47667999	11.5444664	20.1684056
H	2.99000222	12.1217365	20.99252
H	2.90224429	10.8384081	19.7427302
C	3.25679534	7.31759426	16.1355594
H	2.18155162	7.15465078	16.2206666
C	2.09255327	9.72822975	22.5491183
H	1.41141194	9.29286077	21.804132
H	1.67972925	10.6921726	22.8830702
H	2.15999285	9.04001035	23.4033679
C	5.41937267	7.9071772	17.1154043
C	4.93326689	2.22657732	18.8226375

H	4.48632569	1.30592124	18.4415009
C	7.26987191	8.45492563	18.723101
H	7.30698702	9.10943269	19.5990474
H	7.74615448	8.98659069	17.8872254
C	2.09747932	6.28305182	19.5060412
H	1.01563758	6.21476469	19.7029382
H	2.29572134	5.62578018	18.6434046
C	2.81899761	5.7448225	20.7480082
H	2.74473046	6.45608157	21.5813216
H	2.34789913	4.80279953	21.0625758
C	5.31074224	7.34137955	14.8036363
H	5.79489349	7.18751554	13.8367806
C	7.6974374	6.42559457	20.3019013
H	8.44582936	5.64250115	20.4855165
H	7.73612278	7.12252118	21.1467184
C	8.02595143	7.14867417	18.9905118
H	9.09900325	7.39691168	19.0215961
H	7.8949184	6.45839743	18.1407816
C	2.38802457	7.73951073	19.126921
H	1.65250049	8.0755715	18.3826517
H	2.2897115	8.38708669	20.004093
C	6.93799761	3.59157259	19.1567627
H	8.0122463	3.74474688	19.0436462
C	6.08500417	7.73236886	15.9004107
H	7.16053397	7.88806038	15.8054187

C	4.83116737	8.30031463	19.2789475
C	7.25535459	8.54972448	23.8770674
H	6.31430393	8.29850605	24.3851509
H	7.87126972	9.18661857	24.5312474
H	7.79229035	7.60900701	23.683221
C	8.55994232	9.95894057	21.8032595
H	9.1883047	9.10372897	21.5140348
H	9.0527941	10.4914859	22.6322163
H	8.48374932	10.6367358	20.9397632
C	3.92248554	7.13664972	14.9194575
H	3.35254655	6.82722238	14.0409549
C	4.65273992	10.8267653	23.1727778
H	4.18113829	11.8051504	23.3550182
H	4.51992513	10.2203589	24.0820544
C	4.1136123	3.18036266	19.4341109
H	3.03908463	3.02047251	19.5346367
C	6.32006782	2.42873173	18.68604
H	6.92720773	1.66131867	18.2008018
C	6.13716107	10.9745301	22.8337462
H	6.70160051	11.3822925	23.6876176
H	6.2665529	11.6795472	21.9963811
H	4.58919521	7.8416483	22.6215854

Appendix C References

1. Neese, F., An improvement of the resolution of the identity approximation for the formation of the Coulomb matrix. *J. Comput. Chem.* **2003**, *24* (14), 1740–1747.
2. Kossmann, S.; Neese, F., Comparison of two efficient approximate Hartree–Fock approaches. *Chem. Phys. Lett.* **2009**, *481* (4–6), 240–243.
3. Neese, F.; Wennmohs, F.; Hansen, A.; Becker, U., Efficient, approximate and parallel Hartree–Fock and hybrid DFT calculations. A ‘chain-of-spheres’ algorithm for the Hartree–Fock exchange. *Chem. Phys.* **2009**, *356* (1–3), 98–109.
4. Izsák, R.; Neese, F., An overlap fitted chain of spheres exchange method. *J. Chem. Phys.* **2011**, *135* (14), 144105.
5. Neese, F., The ORCA program system. *Wiley Interdisciplinary Reviews: Computational Molecular Science* **2012**, *2* (1), 73–78.
6. Huzinaga, S.; Andzelm, J.; Radzio-Andzelm, E.; Sakai, Y.; Tatewaki, H.; Klobukowski, M., *Gaussian Basis Sets for Molecular Calculations*. Elsevier Science: 1983; Vol. 16, p 434.
7. Andrae, D.; Häußermann, U.; Dolg, M.; Stoll, H.; Preuß, H., Energy-adjusted ab initio pseudopotentials for the second and third row transition elements. *Theor. Chem. Acc.* **1990**, *77* (2), 123–141.
8. Schäfer, A.; Horn, H.; Ahlrichs, R., Fully optimized contracted Gaussian basis sets for atoms Li to Kr. *J. Chem. Phys.* **1992**, *97* (4), 2571–2577.
9. Schäfer, A.; Huber, C.; Ahlrichs, R., Fully optimized contracted Gaussian basis sets of triple zeta valence quality for atoms Li to Kr. *J. Chem. Phys.* **1994**, *100* (8), 5829–5835.
10. Weigend, F., Accurate Coulomb-fitting basis sets for H to Rn. *Phys. Chem. Chem. Phys.* **2006**, *8* (9), 1057–1065.
11. Pantazis, D. A.; Neese, F., All-electron scalar relativistic basis sets for the 6p elements. *Theor. Chem. Acc.* **2012**, *131* (11), 1292.
12. Pantazis, D. A.; Neese, F., All-Electron Scalar Relativistic Basis Sets for the Actinides. *J. Chem. Theory Comput.* **2011**, *7* (3), 677–684.
13. Pantazis, D. A.; Neese, F., All-Electron Scalar Relativistic Basis Sets for the Lanthanides. *J. Chem. Theory Comput.* **2009**, *5* (9), 2229–2238.

14. Pantazis, D. A.; Chen, X.-Y.; Landis, C. R.; Neese, F., All-Electron Scalar Relativistic Basis Sets for Third-Row Transition Metal Atoms. *J. Chem. Theory Comput.* **2008**, *4* (6), 908-919.
15. Sinnecker, S.; Rajendran, A.; Klamt, A.; Diedenhofen, M.; Neese, F., Calculation of Solvent Shifts on Electronic g-Tensors with the Conductor-Like Screening Model (COSMO) and Its Self-Consistent Generalization to Real Solvents (Direct COSMO-RS). *J. Phys. Chem. A* **2006**, *110* (6), 2235–2245.
16. Grimme, S.; Ehrlich, S.; Goerigk, L., Effect of the damping function in dispersion corrected density functional theory. *J. Comput. Chem.* **2011**, *32* (7), 1456–1465.
17. Grimme, S.; Antony, J.; Ehrlich, S.; Krieg, H., A consistent and accurate ab initio parametrization of density functional dispersion correction (DFT-D) for the 94 elements H-Pu. *J. Chem. Phys.* **2010**, *132* (15), 154104.
18. Pettersen, E. F.; Goddard, T. D.; Huang, C. C.; Couch, G. S.; Greenblatt, D. M.; Meng, E. C.; Ferrin, T. E., UCSF Chimera—a visualization system for exploratory research and analysis. *J. Comput. Chem.* **2004**, *25* (13), 1605–1612.